1-1-2018

MESOSCOPIC LIGHT SCATTERING APPROACH FOR STRUCTURAL DISORDER ANALYSIS OF BIOLOGICAL CELLS: APPLICATION IN CANCER DIAGNOSTICS

Huda Almabadi

MESOSCOPIC LIGHT SCATTERING APPROACH FOR STRUCTURAL DISORDER ANALYSIS OF BIOLOGICAL CELLS: APPLICATION IN CANCER DIAGNOSTICS

by

Huda Muslih Almabadi

A Dissertation

Submitted in Partial Fulfillment of the

Requirements for the Degree of

Doctor of Philosophy

Major: Biomedical Engineering

The University of Memphis

May 2018

Dedication

To my little adorable daughters: Tina, Deena, and Zain, and to my husband: Abdulemushen.

Acknowledgments

First of all, I would like to express my gratitude and sincere appreciation to my advisor, Dr. Prabhakar Pradhan, for introducing me to the Bionanophotonics area and giving me an opportunity to pursue doctoral degree with him. Without his continuous guidance and encouragement, this achievement would not have been accomplished.

Secondly, I would like to extend my sincerest gratitude to my Department Chair, Dr. Eugene Eckstein for his continuous advice and support as an advisor throughout my doctoral studies. I am grateful that he was always there whenever I wanted to discuss any academic related problem.

Sincere thanks also to Dr. Richard A. Smith, Dr. Sanjay Mishra and Dr. Omar Skalli for accepting my request to be in my dissertation committee, and providing valuable suggestions and supports despite their busy schedules.

I would like to thank the former and current lab members including Shiva Bhandari, Ethan Avery, Vibha Tripathi, and Hemendra Ghimire, for their supports and inspirations during my research. Special thanks to Dr. Peeyush Sahay for helping me in my research projects and helpful discussions throughout the projects. Special thanks also go to Dr. Aditya Ganju, Dr. Prashanth Nagesh, Dr. Murali Yallapu, and Dr. Subhash Chauhan from the Department of Pharmaceutical Sciences at UTHSC, as well as Dr. Omar Skalli (UofM), for providing samples and useful discussions. I am also thankful to Ms. Lauren Thompson from the Integrated Microscopy Center at University of Memphis for helping me in confocal imaging.

Last but far from the least, I must express my deepest gratitude to my husband and daughters, and rest of my family members for providing me continuous support and encouragements throughout the dissertation work. This accomplishment would not have been possible without them.

Abstract

Almabadi, Huda M., Ph.D. The University of Memphis. May 2018. Mesoscopic light scattering approach for structural disorder analysis of biological cells: application in cancer diagnostics. Major Professor: Prabhakar Pradhan, Ph.D.

Optical techniques are often used to study biological cells and tissues to gain valuable information about them. Recently, the mesoscopic physics based light scattering techniques have provided unprecedented insight into the physical properties of biological systems. In particular, the mesoscopic light transport and light localization approaches allow to measure and quantify nano – to micron scale structural alterations in the biological system. The applications of these techniques have been foreseen in efficient diseases diagnostics and therapeutic studies. Genesis and progression of diseases such as cancer is known to accompany with structural alterations in the building blocks of cells, such as DNA, proteins, lipids, etc. In that context, this dissertation presents a detailed study on quantification of structural changes in the cancer cells, by employing the mesoscopic physics based light transport and light localization analysis. Two different techniques, namely the partial wave spectroscopy (PWS) (light transport) and inverse participation ratio (IPR) (light localization), are implemented to image and quantify 'structural disorder' developed as a result of alteration in the cellular structure caused by cancer diseases. The PWS and IPR techniques were used to quantify structural disorder, represented as 'disorder strength', and thus differentiate normal from cancer cells in several human breast, brain and prostate cell lines. Additionally, the effect of drug resistance developed by the prostate cancer cells, on prolonged chemotherapy treatment, on the structural disorders of the cells was also analyzed. Results show that the cancer cells have higher structural disorder compared to the normal cells and that the degree of structural disorder is correlated with the aggressiveness/metastatic potential of the cancer cells. The results with drug study suggest that the cancer cells which develop resistance to the chemotherapy become more aggressive. Further,

the results of this study strongly indicate that the parameter *disorder strength* can acts as an efficient biomarker/numerical index to assess hierarchy of cancer as well as evaluate efficiency of drug treatment processes

Preface

The major part of chapter four is taken from a paper submitted to the Biophotonic (2018) journal. The major part of chapter five and six have been taken from our below publications:

Optics Express 15428, Vol. 25, No. 13, 26 Jun 2017, and
Journal of Biophotonics. https://doi.org/10.1002/jbio.201700257, Jan. 2018

Table of Contents

List of Figures

Figure **Page**

1 Introduction

Cells in the human body can be divided into two major groups: differentiated cells and undifferentiated cells. Stem cells are included in the undifferentiated group. With few exceptions, specialized cells can no longer divide to produce copies of themselves. However, stem cells can do so in a process called mitosis (cell division) to replace damaged or short-lived specialized cells. In normal cell division, stem cells undergo DNA replication. If such replication is not completed or damage occurs to the DNA, cell division is stopped, and the problems are corrected. Cancer is a disease in which stem cells lose control of the normal cell division mechanism and start dividing and growing even with DNA damage and genetic alterations.

DNA encoded genes play an important role in cancer initiation and development. Gene alteration occurs when there is a change in the DNA nucleotide sequence (i.e., genetic mutation). The accumulation of multiple mutations eventually leads to uncontrolled cell growth (cancer). Genetic alterations affect two groups of genes associated with cancer: proto-oncogenes (oncogenes) and tumor suppressor genes. Normally, proto-oncogenes produce proteins that enhance cell division and suppress cell death, while tumor suppresser genes produce proteins inhibit cell division and growth to prevent tumor formation. An example of an aberrant tumor suppressor gene occurs in Li-Fraumeni syndrome, which involves the p53 protein. In a normal cell cycle, p53 activates the transcription of the p21 protein. Later, the protein stops the cell cycle from moving into the G1 phase, where the duplication of DNA occurs. If there is damage present in the DNA, the block allows the cell to repair the DNA before replication. If the error cannot be repaired, p53 triggers the cell programmed death. Mutations of these two gene groups lead to the two genes losing their normal functions and ability to control cell division and cell death.

The genetic mutations in these two groups of genes can be of two types: germline mutation (inherited cancer) and somatic mutation (non-inherited cancer). A germline mutation occurs in a germline cell (egg or sperm) and thus will be incorporated into the DNA of every cell of an offspring. Somatic mutations can happen in any type of cell in the body except the reproductive cells; thus, somatic mutation is not passed onto offspring. Cancer caused by somatic mutations accounts for 90-95% of all cancer types.

The first step in tumor growth is hyperplasia, the increase cells numbers resulting from losing control of growth (Fig.1.1). In hyperplasia, cells appear normal microscopically (or, cytologically). The second stage is dysplasia, in which cells continue to grow in an uncontrolled manner and appear abnormal under a microscope. Hyperplasia and dysplasia may or may not develop into form cancer. If the cell growth remains localized at the primary location, it is called benign and non-invasive. On the other hand, if the tumor cells spread away from the primary tumor location, they are called malignant, which is the most severe type of tumor.

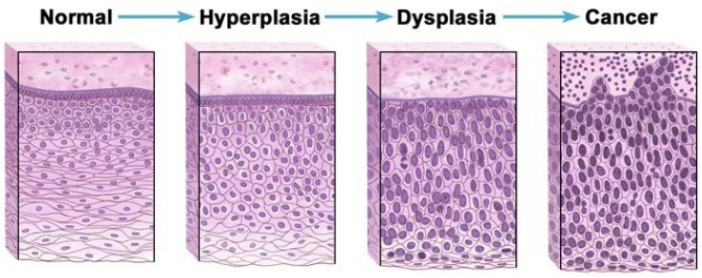

Figure 1.1: The histological changes occur in the epithelium cells with the development of cancer. (Taken from https://www.cancer.gov/publications/dictionaries/cancer-terms/def/dysplasia Accessed: 4/5/2018)

Tumors can arise from any specialized cells in the body. For example, tumors initiating from the epithelial tissues are called carcinomas. Carcinomas are the most common type of

tumors, responsible for around 80% of human cancer. One type of carcinoma is adenocarcinoma, which is formed from epithelial cells that contain specialized cells (secretory cells) that secrete a substance to the tissues they line. Some of the tumors that start in the breast, prostate, and colon are adenocarcinomas. Another example is sarcoma, which represents tumors that occur in soft, connective, and supportive tissues, such as tumors that start in muscles, blood vessels, bones, and fat. Osteosarcoma and liposarcoma are two types of sarcoma that begin in bones and fat, respectively.

1.1 Clinical Cancer Diagnostics Techniques

Cancer is a global problem and the number of cancer patients increases every year. Therefore, cancer patients have put tremendous pressure on the healthcare systems in terms of cost and time. Cancer screening and diagnosis can save lives; therefore, there are routine screenings for different types of cancer. We will discuss some specific cancer cases that are addressed in this thesis. For example, if a patient shows symptoms of prostate, or brain, or breast cancer, a general test is ordered. Based on the results of the test, if a patient's initial screening is positive, the doctor will advise a more detailed examination through some or all of the following tests, depending on tumor location: a histopathology test, a prostate-specific antigen (PSA) blood test, and imaging tests. Improved diagnostic methods hold promise for enabling and care for more patients.

1.1.1 Histopathology

Histopathology is the examination for signs of a disease in a tissue by using a microscope. In a common procedure in which a stained sections of tissues (biopsies) are examined under a microscope by an experienced pathologist for evidence of cancer cells. This procedure is considered as the "gold standard" in cancer diagnosis.[1] After the targeted tissues are removed

from the body, preparation of the histopathological slide involves five steps: fixation, processing, embedding, sectioning, and staining. Fixation preserves the biological sample structurally and chemically in as natural state as possible and prevents cell/tissue autolysis. A chemical substance is needed to stabilize the cell content of proteins and nucleic acids by making them insoluble. Processing removes water from the sample (dehydration) and replaces the water with material that can be solidified, allowing a sufficiently thin section to be cut. The embedding of a biological sample involves placing it in molds with liquid embedding material that later hardens. Sectioning cuts thin biological tissue sections from the hardened block of the biological sample. A steel knife mounted in a microtome may be used to cut sections for light microscopy studies. The typical thickness of a thin tissue section for a light microscopy studies is 5 μm. Finally, staining is an important step in histopathology because it increases the contrast of the sample under microscopy light and hence the clarity of the examined sections. Another advantage of staining is that it allows one to selectively visualize different cellular components of a tissue. Hematoxylin-Eosin (H&E) staining has a long history in medical diagnosis. Eosin stains connective tissue and cytoplasm pink or red, while Hematoxylin stains cell nuclei blue or violet.

1.1.2 Prostate-Specific Antigen (PSA) Blood Test

The PSA is a protein produced by normal and cancer cells in the prostate gland. The PSA test measures the amount of PSA in nano-grams per milliliter (ng/ml) in a blood sample withdrawn from the patient's arm veins. The cut-off level (normal) for PSA in blood is 4 ng/ml, and at higher values prostate cancer is suspected. A PSA level of more than 10 ng/ml increases the chance of prostate tumor to over 50%. However, a PSA level below 4 ng/ml does not reduce the chance of prostate cancer. Different factors affect the PSA and can lead to decreases or increases in the PSA level in the blood, such as advanced age, prostatitis (increase PSA), aspirin, and

obesity (decrease PSA). The sensitivity of the PSA test is 21% for detecting any prostate cancer and 51% for detecting high grade prostate cancer, and it has a specificity of 91%.[2] Moreover, this test has a very low ability to discriminate prostatic hyperplasia.[3]

1.1.3 Imaging Tests

An imaging test captures an image of the tissues inside the human body by using different types of energy, such as x-rays and magnetic fields. Imaging tests can be helpful in cancer diagnosis as they allow the doctor to examine a mass for cancer. Imaging tests, however, are only part of the cancer diagnosis process in addition to lab tests because they carry certain limitations, as tumors must be large enough to show up on an imaging test. Different types of imaging tests include computer tomography (CT) scan, magnetic resonance imaging (MRI) scan, mammography, and ultrasound. Table 1 compares features of conventional imaging techniques for cancer diagnosis.

Conventional clinical techniques have limitations, and none are without drawbacks. Some are extremely expensive or invasive, while others are prone to technical problems. Therefore, there is a continuing demand for an alternative that is inexpensive, safe, and fast as well as optical methods and techniques that overcome limitations in the clinical diagnostic techniques.

1.2 Potential of Optical Techniques in Diagnostic Applications

1.2.1 Conventional Optical Methods: Scattering Techniques

Light scattering by optically heterogeneous media is a fundamental form of light-matter interaction. Biological cells and tissues are heterogeneous optical media, and light scattering is the most dominant form of light-tissue/cell interaction in comparison with absorption, which is very low in the optical regime of electromagnetic radiation. Light scattering techniques based on the optical properties analysis of the biological system have a significant impact on the characterization of biological and biomedical sciences. In cell biology, light scattering

phenomena are utilized as a tool to investigate the structure of cell organelles. The structural changes of organelles, such as nuclei and lysosomes, have been monitored using optical scattering methods and linked to cellular functions, such as apoptosis, metabolism activity, and differentiation.[4,5]

Table 1.1. Imaging Techniques

Clinical Imaging System	**Applications**	**Limitations**
Mammography	• Breast	• Radiation exposure • False-positive results (young women)
MRI Scan	• Liver • Heart • Breast • Brain • Cartilage • Ligaments	• Tissue calcifications not visible • Safety issues (metallic implants)
Positron Emission Tomography (PET)	• Breast • Brain • Whole body	• Radioactive substance decays quickly (short life time) • Expense • Regulatory
CT Scan	• Angiography • Lungs • Head and Abdomen • Brain	• Radiation • Requires IV contrast media
Ultrasound	• Muscles • Joints • Abdomen	Limited access (e.g., lungs, brain, bone)

Applications such as bacteria identification and macromolecule size characterization have been studied using light scattering techniques.[6,7] The field of biomedical optics shows an increase in the variety of optical scattering diagnostic techniques applied for detecting disease

and abnormalities, which have been developed to study the relationship between optical scattering and the physical properties of tissues. In diagnostic optical methods, when a light beam is incident on a scattering source, light is scattered by different tissue structures, such as cells, membranes, and proteins, in all directions as light interacts with the sample. Depending on the nature of the study, measurements, such as magnitude/phase of the scattered light, intensity as a function of wavelength, and intensity as a function of angle of scattering, are conducted in the near or far fields from the scattering center. Since the amount of scattered light depends on the refractive index, orientation, and size of the scattering objects, information such as extinction coefficients, anisotropic coefficient, refractive index, and size of the scattering elements are often calculated through such measurements.[8,9]

1.2.1.1 Spectroscopic Techniques

Optical scattering techniques vary widely depending on the investigated parameter and the physical information intended to be extracted from a sample. Spectroscopy, an example of an emerging optical scattering technology, is defined as the measurement of a scattering quantity as a function of wavelength, frequency, or energy in a defined band width. Spectroscopic techniques are a rapidly growing area of research because they provide spectral dependent information about the biochemical and biophysical (structural) compositions of the sample depending on spectroscopy type.

Different types of spectroscopic methods are based on the type of samples and light interactions involved in the measurement process. For example, in Raman spectroscopy, biochemical information can be obtained by measuring the intensity of light as a function in the frequency shift. [10] In addition, elastic light scattering spectroscopy in the visible range measures the intensity of light as a function of wavelength or frequency to determine the structural

characteristics of samples. Elastic light scattering in tissues/cells occurs when the light is redirected (by the cellular and subcellular components, such as nuclei and mitochondria) without change in the wavelength of the reflected light. Cellular and subcellular scattering elements (scatterers) have physical characteristics, such as size, concentration, and density. Any change in these characteristics is an indication of change in the scattering properties of the sample. In most disease cases, the structural properties of a cell/tissue changes at all types of length scales: ranging from μm to cm in tissue and nm to μm in cells. For example, in most cells, enlargement of nuclei is an indication of tissue transition from normal to dysplastic growth. Such changes in biological cells/tissues leads to a change in the characteristics of the scattering spectrum, which in turn can be utilized for diagnosis purposes in different biomedical applications to discriminate cellular/tissue abnormality in disease conditions.[11]

1.2.1.2 Confocal Laser Scanning Microscopy

In addition to elastic scattering spectroscopy techniques, confocal laser scanning microscopy (CLSM) is another modality of optical scattering applied for biomedical purposes. Confocal scanning microscopy is an improved version of fluorescence microscopy introduced to overcome the size- resolution and contrast limitations of fluorescence microscopy. In fluorescence microscopy, a light source illuminates the entire sample and a detector captures all sample fluorescence, including the unfocused light. In contrast, confocal microscopy blocks the out-of-focus light with a point illumination technique and a pinhole in front of the detector to reject the out-of-focus light. This configuration allows only the light emitted from the florescent emitters near the focal plane to reach the detector and hence improves image quality and resolution. Moreover, it offers a depth selectivity that allows optical sections of the samples without physical contact with the sample. These two features and, more recently, molecular labeling

make confocal microscopy a powerful tool in biomedical sciences to study living or fixed cells and tissues.

1.3 Existing Literature

In biomedical applications, especially for diagnostic applications, there is an increasing interest in investigating the optical properties of cells and tissues using optical technologies. This interest stems from the many advantages of optical techniques, such as no tissue excision needed and fast, inexpensive, real-time diagnosis. More importantly, optical techniques such as fluorescence and light-scattering techniques can be used to diagnose and monitor their progress and treatment. The techniques identify and characterize pathological changes at the cellular and subcellular scales by providing structural and biochemical information. With the development of new optical methods and techniques, the optical parameter refractive index has gained attention within the disease diagnosis and biomedical optics research community. The effective and average refractive index of a single cell has been studied extensively to give detailed information of cell pathology.

Choi et al.[12] used optical coherence microscopy to characterize cancerous and healthy cells by measuring the distribution of the optical parameter refractive index of a single cell. Cancer cells showed a higher average refractive index than healthy cells. *In vivo*, Backman et al.[13] used the light scattering spectroscopy of four organs with three different types of epithelium: stratified squamous epithelia of the oral cavity, transitional epithelia of the urinary bladder, and columnar epithelia of the colon and Barrett's esophagus, to measure the thickness and refractive index of the epithelial cells. The extracted information was used to diagnose dysplasia and carcinoma cases based on quantitative measurement of nuclear size, which revealed that nuclei from both the epithelium cells tissues displaying dysplasia and the

carcinoma had greater percentages of enlargement. In addition, the normal and abnormal refractive index were compared to find a correlation with a disease, such as cancer.

Wang et al.[14] used quantitative phase microscopy to measure the average refractive index of breast biopsy specimens. Three groups of cells were studied: normal, histologically normal, and malignant cells. The results showed an increase in the measured refractive index of the malignant and histologically normal cells compared to the normal cells, with malignant cells having the highest refractive index. Different clinical studies have shown that at metastatic stages of some cancer types, such as breast and prostate cancer, tumor cells circulated in the blood stream. Tumor cell mass density (refractive index) has been determined in ovarian cancer patients and compared to the white blood cell mass density in detecting the circulating ovarian cancer cells. [15] The results were used to provide a new detection system for ovarian cancer using mass density quantification through the refractive index measurement. In Wang et al., [16] the refractive index distribution of histopathology slides of prostate tumors was measured using a spatial light interference microscopy (SLIM). The phase shift images were compared using H&E stained histopathology slides (where normal and malignant areas were marked). The resulting measures on SLIM images showed strong correlations with the normal and cancerous areas indicated on the prostate slides.

Moreover, various experimental studies using optical coherence tomography (OCT) have measured the refractive index *in vitro* and *in vivo*. These measurements highlighted the importance of the refractive index for monitoring physiological changes in living tissues. For example, Zhernovaya et al. [17] measured the refractive index of glucose-hemoglobin solutions at different glucose concentrations to evaluate the glycated hemoglobin amount in the plasma of

blood. Meng et al.[18] reported a study on the refractive index of human teeth and anticipated the potential of the method to predict the changes caused by dental decay.

1.4 Limitations of Conventional Optical Techniques

The analysis of light propagation through biological media has drawn significant attention because of potentially important applications it can offer in disease diagnostics. The main purpose of such techniques is to analyze the intracellular architectural alteration developed inside the cells and tissues with the progress of the disease, such as cancer. Light transport analysis includes the study of light-matter interaction and specifying the optical properties of the medium, such as absorption coefficients, scattering, anisotropic factor, and refractive index. Being able to accurately extract the optical properties of a biological medium is the key to diagnostic and therapeutic applications of light. One of the motivations of diagnosis of biological samples based on optical measurement is to reduce or eliminate the need for the normal biopsy and replace it with optical biopsies. The term optical biopsy refers to the use of light scattering properties to make an instant diagnosis without the need for tissue removal if it is accessible for light experiments.[19] The technology associated with fiber optics and micro-sized optical components can be applied after sound measurement processes are shown using larger, standard optical components such as those used in this work.

Light is a highly sensitive probe suitable for investigating the physical and geometric details of biological systems, as organelle sizes are the same scale as the probing light wavelength in visible range. Optical methods are among the most powerful non- or minimally invasive tools to determine morphological structural changes of a biological system. For a biological sample in the visible optical window (400-700nm), light scattering is more dominant than absorption.[20] Hence, most optical methods rely on a light scattering approach to determine

the structural characteristics of cells and tissues.[21] Biological samples, including tissues and cells, have a mass density distribution that varies during physiological changes at the cellular and subcellular levels during the progression of diseases. Such structural changes occur with the progress of carcinogenesis due to the alteration of the building blocks of cells, such as DNA, proteins, and lipids. These alterations bring changes in mass density within the cell. It has been shown that the local refractive index in a biological system is directly proportional to the local mass density in the medium.[22] Therefore, any change in the spatial mass density distribution inside biological media also results in a change in their refractive index distribution. Thus, because a change in the refractive index can be sensed using light as a probe, the refractive index is a widely used physical parameter to characterize diseases such as cancer with optical methods.[16]

A change in the spatial variation of the refractive index of biological media introduces a change in the distribution and amount of scattered light. However, light scattering by complex heterogeneous media, such as biological cells or tissues, is not well understood. There is no well-defined analytical framework to perform such studies. In optics, Maxwell's equations and transport theory are fundamental physical theories used to describe the light scattering problem in biological systems. Unfortunately, exact analytical solutions for Maxwell's equations are not available for complex structures. Additionally, performing approximate numerical calculations is highly tedious and not clearly applicable. Instead, several simplified approximations are used to analyze light scattering from biological media; of these, Rayleigh theory (for particle size $<< \lambda$) analysis and Mie scattering (for particle size $>> \lambda$) analysis are the most common.[23–25]

Although these approximations provide a reasonable estimation of several optical parameters of the samples, such as refractive index, sample size, and extinction coefficient, one

of the main limitations of such techniques is that they measure the changes in average (bulk) properties of the refractive index of the samples.[26] To illustrate this, let us consider that the refractive index inside a biological sample, at any point (r), is expressed as $n(r) = n_0 + dn(r)$, where the n_0 and $dn(r)$ represent the average (bulk) and fluctuation part of the refractive index, respectively. The conventional optical and analysis techniques, such as phase contrast microscopy (PCM), OCT, and Mie scattering, analyze the bulk ($<n(r)>=n_0$) part of the refractive index. This is because these optical techniques are insensitive to the refractive index fluctuation.

However, it has been now realized that the quantification of refractive index fluctuation (standard deviation) as opposed to the bulk refractive is highly useful, especially when the changes inside the system are not large enough to be detected by the abovementioned conventional techniques. For example, in early carcinogenesis, structural changes were found to occur at the nanoscale due to the intracellular structural alteration in cells at the nanoscale.

In this regard, to study the fluctuating part of the mass density or refractive index in a cell, mesoscopic-physics-based studies were made of light wave propagation and light localization properties in spatially random media recently developed into the biological system.[14,15] The advantage of the mesoscopic approach is that it allows the calculation of the properties of the fluctuation (dn) part of the refractive index in the sample more accurately/efficiently. The term *random media* refers to media with refractive index $n(r) = n_0 + dn(r)$ varying in space, with the variation being random (represented by dn(r) part); hence, such a system is called a random or disordered system. Moreover, a medium can be described as weakly or strongly disordered, depending on the value of the refractive index fluctuation compared to its mean background index. In optical scattering experiments dealing with a biological sample, the medium is considered weakly disordered since its refractive index

fluctuation is much smaller (dn~.01) than the average refractive index background value (n_0~1.38), that is $dn(x)/n_0 << 1$.

The next section introduces two techniques explored in this thesis to move closer to implementing optical biopsy in cancer diagnostic applications. The techniques were based on mesoscopic physics analysis approaches of a weakly disordered system.

1.5 New Optical Techniques

Two optical scattering techniques were recently introduced that take advantage of mesoscopic physics analysis, namely partial wave spectroscopy (PWS), based on spectroscopic microscopy techniques, and the inverse participation ratio (IPR) technique, based on confocal imaging. These techniques apply for the first-time concepts of condensed matter physics concepts to understand structural properties of biological systems ranging from nano- to submicron-scales. In both techniques, the degree of structural disorder (randomness) of the biological systems are analyzed, and the measurement are expressed in terms of a parameter called the degree of structural disorder strength , or disorder strengths (L_{sd}), which quantify the spatial fluctuations of the refractive index of the biological samples.

1.5.1 Partial Wave Microscopy Spectroscopy (PWS)

PWS is a technique recently introduced to study the intracellular structural changes in disease processes, such as cancer. The PWS system is a backscattering technique in which the spectral imaging of the biological cells is produced by combining spectroscopy and microscopy. This type of analysis is based on mesoscopic light transport theory in a quasi-1D disordered system. The quasi-1D transport theory assumes that when a light wave is incident on dielectric media such as a biological system at a normal incident angle, the 180^0 backscattered light is most sensitive to refractive index fluctuations inside the sample along the direction of the incident

wave.[26,27] This fundamental light-matter interaction is exploited to determine the average refractive index (averaged along the depth or light path of the sample in 1D) at different spatial positions (in the sample plane perpendicular to the light path) of the sample; the fluctuation of the quantify the refractive index is also quantified along the light-incident direction.

Therefore, in PWS analysis, the sample in the image plan is virtually divided into several parallel 1D channels, with each channel represented by a pixel size. In addition, the backscattering spectrum of each channel (pixel) is collected. The advantage of the spectral image analysis of the backscattering intensity lies in identifying the spectroscopic signatures associated with intracellular changes, since it reflects the refractive index fluctuation along each channel. The technique evaluates properties of cell nano-architecture by measuring structural disorder strength at many pixels. The spectral reflection coefficients and its correlation function in wave length/wave vector are needed to calculate L_{sd}.

1.5.2 The Inverse Participation Ratio (IPR) Technique

In biological media, disorder represented by the refractive index fluctuation (*dn*) is the main cause of wave scattering and eventually halts light transport. The cessation of light transport is attributed to the localization of waves. The localization effect has been studied extensively in condensed matter physics.[28,29] Light localization can be defined as phenomena that arise due to the interference between waves after multiple instances of scattering by the disorders in the system.

Recently, the idea of light localization was introduced to the biological studies through the IPR technique. This technique was introduced to study and quantify the structural disorder properties of cancer cells using TEM images.[30,31] Accurate structural characterization of a biological system requires correct information about the spatial mass density variations.

However, a biological system by nature is heterogeneous, which makes characterization of the system a difficult task. The spatial heterogeneity of the biological system has led to the use of different correlation functions and multiple parameters to describe the mass density inside the biological systems. In the pragmatic side, there is a significant interest in minimizing the complicity of cell characterization and so, an introduction of a single parameter that might provide appropriate descriptions of cell/tissue structure and structural changes. The IPR technique satisfies the criteria of characterizing the cell architecture in a single parameter (the IPR). This project further developed the IPR technique by introducing confocal microscopy imaging. An analysis of light scattering was performed in a lattice constructed from confocal imaging of cells to study the properties of light localization in biological cells.

The IPR technique explores the linear relation between intensities of the confocal fluorescence microscopy images and the biological mass densities (ρ). As a first step, a refractive index matrix is constructed from a confocal micrograph. This is followed by statistical analysis of the optical eigenfunctions of the refractive index matrix using in a closed boundary condition, which leads to the calculation of average IPR (<IPR>) value of the eigenfunctions.The parameter of <IPR> is a measures of the strength of light localization in the observed biological system, which in turn is a measure of the degree of effective structural disorder in that system.

1.6 Objectives

It is now recognized that structural characterization of a biological cell particularly sensitive determination of subtle alterations of internal structural properties is of primary importance for many biomedical applications, especially for cancer diagnosis and screening. Many cancers are curable if diagnosed and treated at an early stage. Therefore, detecting early cancer by characterization of cells is a topic of immense research interest. As the size of cell features varies

from a fraction of a micron to a few microns, visible light (wavelength λ varies from .4μ to .7μ) is a potential probe for the characterization of these biological cells when its scattering properties are characterized. Furthermore, recent studies have shown that the internal disorder properties of a cell change with the progress of carcinogenesis in the cell. Therefore, characterization of the disorder properties of cancerous cells was the focus of this dissertation. The specific aims of this research were as follows:

1. To develop a new version of PWS system and study the structural disorder at the nanoscale of three different standard human cancer cell line models (breast, brain, and prostate) by taking advantage of PWS reflection intensity spectra and analyzing them using mesoscopic-physics-based formalism.
2. To study the chemotherapy efficiency in prostate cancer treatment using the PWS technique via nanoscale structural disorder analysis of non-drug-resistance cancer and drug-resistant prostate cancer cells.
3. To study the same cancer cell line models' structural disorder, as described in 2, at the submicron scale via the IPR technique using confocal microscopy imaging.

1.7 Overview of the Dissertation

The remainder of this dissertation is organized as follows. **Chapter 2** describes the PWS system, including a detailed description of the experimental set up, system calibration, and error analysis. **Chapter 3** is a report of studies of the structural disorder of the breast and brain cell lines using the PWS technique. In it, the disorder strength of the disorder strength is quantified for each cell line, and compared to corresponding normal cells. **Chapter 4** examines the chemo-resistance of prostate cancer cell lines to understand the architectural changes associated with the drug-resistant cells using optical disorder analysis. We compare the nanoscale structural alterations of

chemotherapy drug-resistant cancer cells and with the structural disorder of the drug-sensitive cancer cells.

Chapter 5 presents a novel technique, the IPR, to study the light localization properties of a biological sample based on confocal imaging, which is used to quantify the effective structural disorder at the submicron level. The chapter presents confocal working principles and the theoretical description of the IPR technique followed by the analysis method employed to calculate the effective structural disorder of a biological cell and then calculation of average IPR, <IPR>, by ensemble averaging. **Chapter 6** evaluates the performance of the IPR techniques to study the structural disorder in the breast, brain, and prostate cell lines. **Chapter 7** provides a summary of the results from work presented in this dissertation and suggests ideas for further development and future research.

2 Partial Wave Spectroscopy (PWS): Nano Structural Disorder Measurement System

2.1 Introduction

Optical spectroscopy and microscopy have greatly advanced our knowledge of biological systems. A combination of both the techniques in one modality provides advantages of both the techniques by allowing simultaneous microscopic view and spectral analysis of regions of the sample. Ideally, multi-modal imaging approaches are needed to examine and address nano-meso-microscopic substrates with different contrasts using the same optical platform. In a combined optical spectroscopy and microscopy technique, i.e., hyperspectral imaging, the spatially-resolved spectral response of a system (images at different wavelengths or full spectral in each pixel comprising a hyperspectral image) is captured; the resulting spatio-spectrally-resolved microscopic image cubes (Fig.2.1) contain a wealth of physical and chemical information about the system of interest.

Traditionally, frequency/energy/wavelength tuning is achieved either by recording a collection of point spectra at different spatial positions in 2 or 3D, or using conventional imaging detectors, whereby stacks of images are recorded at single wavelengths at a time. Both approaches are restrictively tedious and time consuming. In this context, recent developments in computer controlled liquid crystal tunable filters (LCTF) for wavelength tuning has dramatically advanced the field of hyperspectral imaging. Presently, the whole sample under illumination can be imaged in one shot for each wavelength using LCTF. This development has accelerated this field in recent years, whereby novel experiments and applications of hyperspectral imaging are sought-after and are regularly reported as well. One such application is using hyperspectral imaging to determine the refractive index (RI) and refractive index fluctuations in dielectric media. For example, PWS

technique combining hyperspectral imaging with mesoscopic physics to analyze RI and RI fluctuations in biological cells.

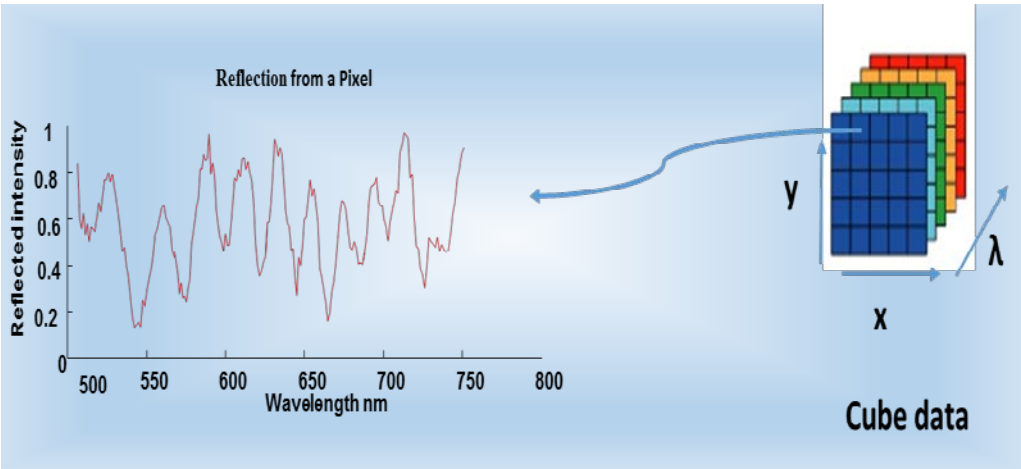

Figure 2.1: Schematic of hyperspectral-imaging. Plot of the backscattered intensity as function of the wavelength of light.

2.2 Mesoscopic Physics Approach and Biological System

The mesoscopic theory of light suggests that when a light wave is incident onto a dielectric media at a normal incidence angle, the 180^0 backscattered light is most sensitive to RI fluctuations inside the sample along the direction of the incident wave. [32, 33] This fundamental light-matter interaction can be exploited to determine the average RI (averaged along the depth or height of the sample in 1D) at different spatial positions (in the image plane) of the sample as well as to quantify the RI fluctuation along the light-incidence direction. While theoretically there is no limit to the detection of RI fluctuations, experimental studies of PWS technique have shown nano-scale levels of accuracy (~20 nm) in determining changes in RI fluctuations in standard dielectric media.[33] It should be noted that the naturally occurring dielectric media such as biological systems typically fall in mesoscopic length scale regime (few hundred nano meters to few microns); thus, the techniques of mesoscopic physics are readily applicable to such systems. However, now, very few

laboratories have used the meso-scale index measurements for quantification of fluctuations in biological cells. The opportunity for us was to focus on cancer as a particularly appropriate diagnostic area and possibly as an area of analysis of therapeutic effects. Thus, one of our major interests is to extend this analysis, to broader set of target systems such as brain and breast cells and chemotherapy resistance cells in the following chapters.

2.3 Description of the Partial Wave Spectroscopy (PWS)

2.3.1 Instrumentation

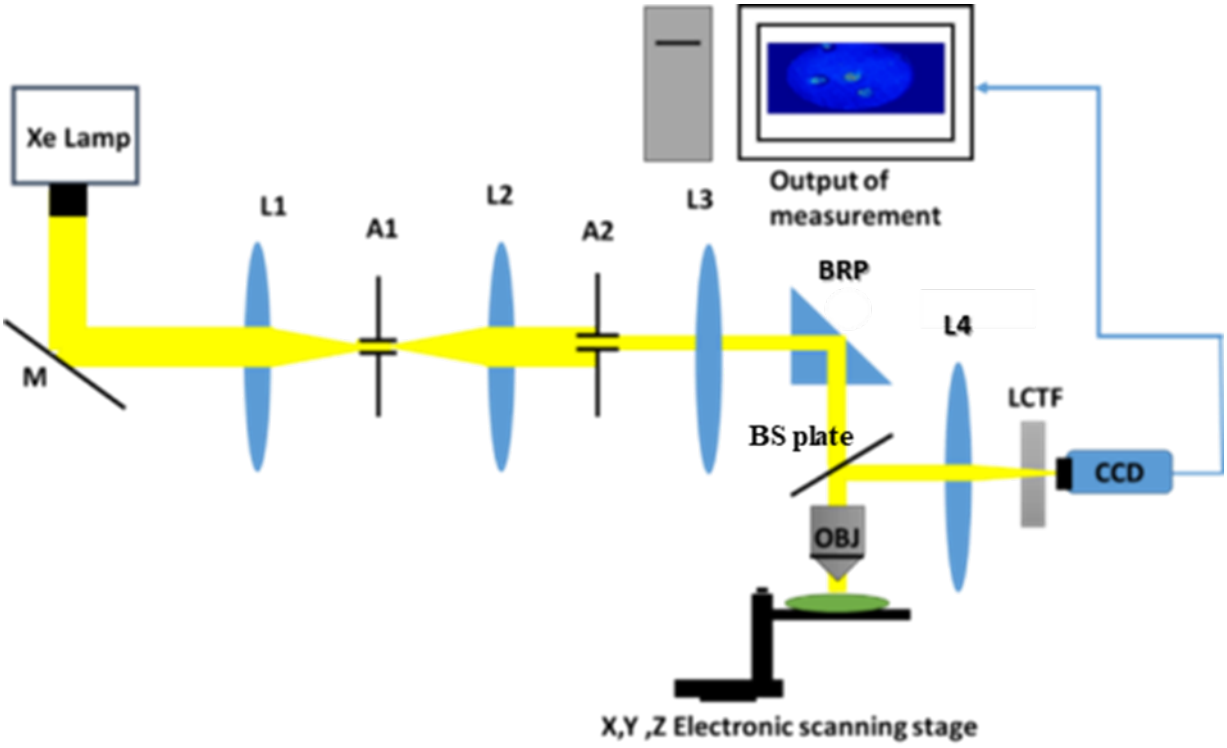

Figure 2.2: Schematic of the Partial Wave Microscopy Spectroscopy (PWS) System (PWS). M: Mirror; L: lens; A: Aperture; BRP: Right Angel Prism; BS Plate: Beam splitter plate; OBJ: Objective Lens; LCTF: Liquid Crystal Tunable Filter; CCD: Detector CCD Camera.

This section discusses about the spectroscopy system for performing the partial wave acquisition.The spectroscopy system is an optical measurement system that allows the partial

spectral collections of the backscattered signal $I(x,y;\lambda)$ and then imaging of the disorder strength at a particularspatial point (x,y) using reflection wavelength (λ) spectra. The division of the back reflection intensity into many parallel quasi-one-dimensionalreflectionspectra, hence the name Partial Wave Spectroscopy (PWS). PWS consists of a set of optical components that is connected and combined to make up the PWS system. The schematic of the PWS instrument developed by us at the BioNanoPhotonics Lab at UofM is shown in Fig.2.2. A broadband of white light from a Xenon arc lamp is used to illuminate the sample through Kohler illumination. First, the light is directed through a mirror to pass through a set of 4-f relay system lenses and apertures in order to collimate the light efficiently. Then the light is directed by a right-angle prism (BRP) to let it pass through an objective (in NA=0.65) and focused on the sample which is held on electronic motorized stage.The backscattered light was passed through the same objective lens and projected with a 40X magnification onto the slit of a liquid crystal tunable filter (LCTF), where the signal is filtered according to its wavelength components for spectral collection. The spectral resolution of the LCTF is 1nm and the spectral range is approximately the visible range (450-700nm). The LCTF is coupled with a CCD camera detector, therefore, the filtered signal is acquired by the CCD camera. The combined LCTF-CCD camera system allows to capture the backscattered image of the sample at different wavelengths (λ), over the full visible range. Each image collection point is represented by a 2D matrix with (x,y) as the spatial position of each pixel of the matrix (dx×dy). Eventually, we acquire a datacube $I(x,y;\lambda)$ for the three variables (x,y,λ). In the further processing of the data, the backscattered spectrum fluctuation $R(x,y\ \lambda)$ is extracted by filtering out the noise in $I(x,y;\lambda)$ signal.

Hence for each pixel on the captured image, we can calculate disorder strength (L_{sd}) of a biologcal sample, using the intensity captured for each pixel, which is theoretically defined as [3]

$$L_{sd} =< dn >^2 \times L_C \quad \textbf{(1)}$$

Where σ^2 is the variance of the refractive index fluctuations inside the 1D depth of the sample at the spatial position corresponding to the pixel point in the image, and L_C is the spatial correlation length of refractive index fluctuation along that depth. Therefore, the disorder strength value, L_{sd}, at any point in the sample, provides a measure of the refractive index fluctaution along the depth of the sample at the point, both in terms of its fluctuation strength and correlation length. Theoretically, the L_{sd} values can be determined if the two physical quantities, i.e., σ^2 and L_c, are known. However, in actual in practice these individual values are not known; in their stead the PWS measurement allows the calculation of the L_{sd} values for many pixel points using the spatio-spectral detail acquired from the backscattered imaging data, $I(x,y\,\lambda)$, and assume there is sufficient redundancy in the observations that estimated individual values could be separated.

2.3.2 Optical Components of PWS System

The following table is a list of all the optical components that were used to build the experimental set up of the Partial Wave Microscopy Spectroscopy System. The components specification and manufacturer are indicated in Table 2.1.

2.4 Measurement System Analysis

In brief, the experimental set up was calibrated with a standard specimen with known backscattered signal. Also, the system sources of noise were indicated as either background or due to the detector noise and lessening of the noise was achieved by performing the experiment in a dark room to avoid random stray light from reaching the detector sensors.

Table 2.1: List of the optical components of Partial Wave Micrscopy Spectrscopy(PWS) System

Optical Components	**Spesfications**	**manufacturer**
Xenon Lamp	White light	Newport Corp, CA, USA
Mirror (M)	Broadband dielectric round mirror Diameter, 50 mm, Reflectance, R >99%	Thor labs, NJ, USA
Lens (L1,L2,L3,L4)	Lens shape, convex lens focal length, 50 mm λ range, 350-700 nm Diameter, 25.4 mm	Thor labs, NJ, USA
Apartures (A1,A2)	Minimum Aperture, 1.5 mm Maximum Aperture,25 mm	Newport Corp, CA, USA
Right angle prism(BRP)	Size, 25.4 mm Used as a 90° reflector λ range, 430-700 nm	Newport, CA, USA
Beam splitter(BS) plate	Reflected: Transmitted, 50:50 Dimentions, 25×36 mm	Thor labs, NJ, USA
Objective (OBJ)	0.65 Numerical aperture 40x Magnification	Newport CA, USA
Electronic scanning stage	Resolutions, 100 nm in vertical direction (z-axis) and 40 nm in x-y plane	Zaber Technology Inc. Canada
Liquid crystal tunable filter (LCTF)	Visible range, 400-700 nm	Varispec, PerkinElmer Inc. MA, USA
CCD camera detector	Resolution, 1392 × 1040 Pixel size, 6.45µm × 6.45µm	$CoolSNAP_{HQ}^2$, Photometrics, AZ, USA

Moreover, the thermally generated noise was reduced by cooling system in the CCD camera detector that used in the experiments. Along with the experimental data acquisition, additional images were captured by the camera after the light let to passes through a glass slide

has no sample to collect the backscattered signal from the glass substrate only. The intensity reading of the sample-free slide is considered as background noise and thus it is subtracted from each pixel intensity of the actual sample reading through the data analysis process.

The purpose of each experimental measurement is to find the best estimate for the true (unknown) value of a physical quantity being measured. The measured quantity is not exact, but varies due to the presence of errors in measurement processes. Therefore, the best estimate value is not enough when we want to state the true value of the measured quantity, but an estimate of the errors present with that best estimated measured value is also necessary to predict the accuracy of measurements. In this regards, uncertainty in measurement analyses (or error analysis) is a process in which estimation and quantification of the errors that are a part of the measured values can be calculated and separated. Errors in the measured value classified as mainly of two types; 1) Systematic errors and 2) Random errors.[34]

2.4.1 Systematic Errors

Systematic errors are errors that shift the measured value from the (unknown true) value by certain amount and it always shift the data value in the same direction, either above or below the true value. Since systematic errors do not change with repeating the experiment, the statistical analysis of the measured data cannot be used to evaluate systematic errors. However, systematic errors can be reduced and corrected by a calibration process and performing experiments on known samples; they cannot be eliminated. Systematic errors are hard to be detected, but knowing the limitations of the measurement system can help to locate some of the elements that might contribute to a systematic error in the readings/measurements.

2.4.2 Random Errors

Random errors are errors that cause the scattering of the measured quantity to be lower or higher than the true value every time the measurement conducted. Any unpredictable changes in the measurement system and the environmental conditions have a high chance to introduce random errors to the measured quantity. Statistical analysis of the measured data is the best path to be followed to evaluate and minimize random errors in the measurement. The mean of a large number of readings N gives the best estimate of the quantity under the measurement (unknown true value). The standard deviation (SD) of the same set of readings tells about the spread of the measured values aside from the mean and how close the data points to the mean value and it is given by the by the square root of the sum of the squared of the differences from the mean. The accuracy of the best estimate can be described by calculating the standard error of the mean.

$$\text{Standard error} = {}^{\text{SD}}/_{\sqrt{\text{N}}} \qquad \textbf{(2)}$$

2.5 Extracting of Backrefleaction Signal *R(x,y,λ)* of Known Sample

In order to extract a reliable signal from PWS measurement system, it should be calibrated first using a known/reference sample. Calibration helps to predict/minimize the errors introduced during the measurement, including both systematic and random errors, as well as errors that arise due to the limitations of the components that make up the measurement system. We expect that back-reflection signal measured by the PWS contains both systematic (bias) and random errors (noise) that introduce deviations of the pixel intensity values in our image. Sources of noise in our system arises due to detector, microscopic optical components (lens surface, dust, and uneven illumination) and ambient noise. Detector noise such as shot noise and dark current

(thermal noise) are main contributions to CCD noise. We followed different techniques to minimize the overall CCD noise. For example, to lower the dark current signal, the CCD detectors were cooled, and the experiment was performed in a dark room to reduce the random photons from reaching the detector, hence reducing the noise contributed by the detectors to the overall image.

The schematic of the PWS instrument as shown in Fig.2.3 highlights places of error elements where the major errors were expected to present, and the following sections explain how we corrected for them.

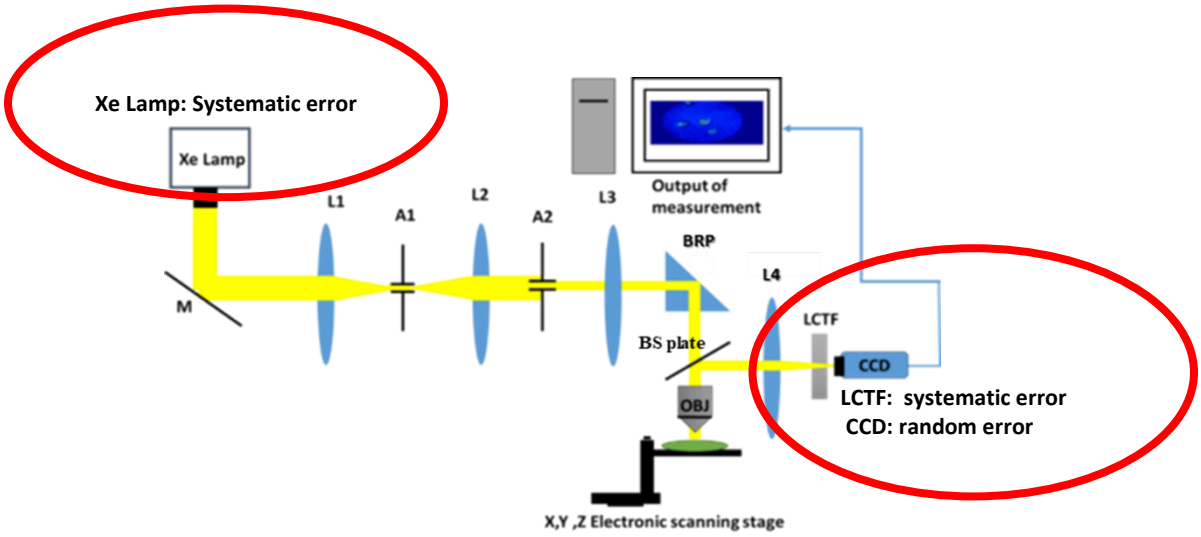

Figure 2.3: Elements of errors on the PWS system. Expected systematic errors in the lamps and LCTF and random errors represented by the CCD camera.

2.5.1 Butterworth Filter and Removal of the High Frequency Signal

2.5.1.1 Random Error in the Backscatter Intensity $I(x,y;\lambda)$

Here we perform calibration and error estimation of PWS system using known size of polystyrene beads. Beads have known radius and refractive index; therefore, back reflection spectra are well known. In Fig.2.4a the raw signal acquired from PWS of single pixel on the

image (center of a single polystyrene bead) is plotted as a function of the wavelength of light. By examining the signal, we see that there is very low frequency signal (or low oscillation), combined with a high frequency signal that appears imposed in top of it. Since the beads have no disorder (no fluctuation in the refractive index), the pattern of reflection excepted to be oscillatory, in particular along the diameter of the bead, therefore, the noise (high frequency signal) was clear in the signal. The high frequency signal we expected to have different unknown and known factors such as shot noise, and dark noise from the CCD camera.

In order for us to correct the present high frequency noise, we applied a 3rd order low pass Butterworth filter with cut off frequency of 0.5 Fig.2.4b). The data from spectral range of (520-640nm) only used due to the poor signal in the below or above this range.

2.5.1.2 Polynomial Fitting and the Correction of Systematic Errors in $R(x,y,\lambda)$ Signal

Spectral emission from the Xe lamp is non-uniform emission where light with higher wavelength has more emission (higher amplitude) from the lamp compared to light with lower wavelength. [35] Moreover, the LCTF has higher transmission for higher wavelength compared to lower wavelengths.[36] The LCTF transmission signal gave raise to systematic errors that shift the recorded backscattered signal from the expected pattern (sinusoidal). If we plot the reflected signal that collected at the CCD camera verses the wavelength of light, we can see that the plot has an oscillatory and increasing in amplitude as a function of the wavelength, where the signal should be oscillatory only in pattern and constant amplitude if plotted as a function of the wavelength oflight. Figure 2.4a shows the backscattered signal of a 6-micron polystyrene microsphere imaged at different wavelengths. We corrected the systematic variation in the signal due to the lamp spectrum and the LCTF by subtracting a third order polynomial from the

backscattered intensity *I(x, y λ).* The corrected signal after removing the high frequency signal and the systematic errors introduced by the lamp and the LCTF is shown in Fig 2.4b).

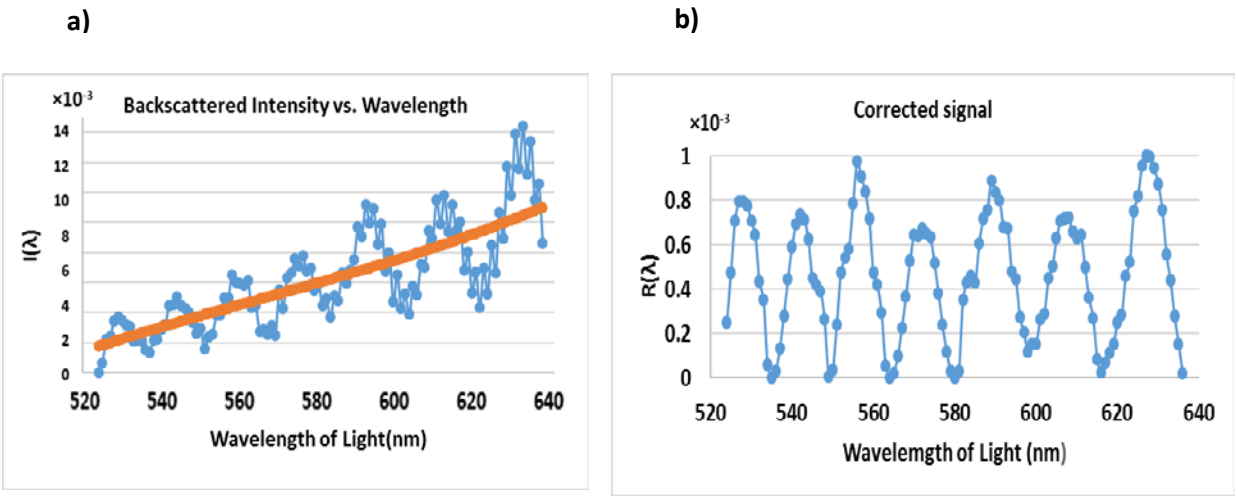

Figure 2.4: **a)** The backscattered signal of a 6-µm polystyrene bead from the PWS system. **b)** The corrected signal after: (1) subtracting the polynomial and (2) applying the Butterworth filter.

2.6 Calibration of the PWS System

To ensure the accuracy and reliability of the PWS instrument, we compared the experimentally measured backscattered signal by the PWS system and the theoretically calculated backscattered signal by a single polystyrene bead with diameter of 6 µm, at the tip of the bead. The backscattered signal from the tip (center) of a bead can act as an approximate thin film (slab model) of thickness of its diameter (*d*). For a thin film of known thickness (*d*), the reflected intensity can be expressed by the following exact equation.[37]

$$R = \frac{(m^2-1)^2 \sin(2mx)^2}{(m^2-1)^2 \sin(2mx)^2 + 4m^2} \quad \textbf{(3)}$$

Where m is the refractive index of the material relative to the air, and x is the size parameter ($x=k*d/2= (2\pi/\lambda)*d/2$)

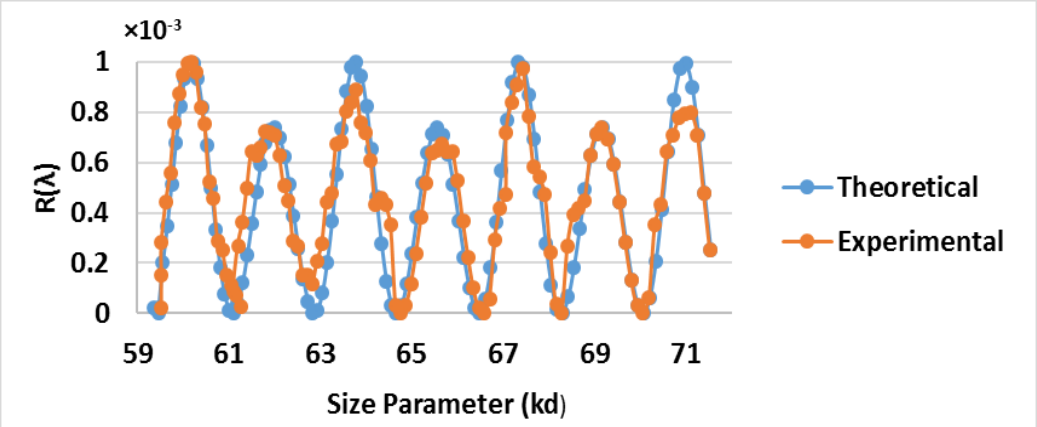

Figure 2.5: The PWS backscattered signal of a 6μm polystyrene bead in agreement with the theoretically calculated backscattered signal of a thin film back reflection signal of the same thickness d=6μm. This result confirmed that the PWS system is well calibrated.

Figure 2.5 shows the backscattered reflection intensity spectrum signal from a slab model calculated using MATLAB with incorporation of the geometry of the 6μm bead and the backscattered signal spectrum from the center of the polystyrene bead with diameter of 6μm calculated experimentally. The theoretically calculated and experimentally measured reflection data are plotted as function of the size parameter. The spectrum measured by the PWS system shows overlapping periodic pattern as predicted by the theory. As shown in Figure 2.5, there is a good agreement between the PWS measured signal and the theory single, the PWS were able to predict the periodic natural of the signal which provides an experimental proof that PWS is well calibrated.

2.7 Zero Error of PWS and Adjustment.

In order to examine the zero error of the PWS system we have conducted a measurement on three types of polystyrene beads with size 3, 6, and 10 µm. We smeared aqueous suspension of polystyrene microspheres of each size on a glass slide as separately puddles and after few minutes of evaporation at the room temperature, the samples were ready for imaging. We collected the spectrum for each bead size separately, and after image processing we calculated the disorder strength L_{sd} using the extracted *R (x, y, λ)* where

$$L_{sd} = constant * < R > \quad \textbf{(4)}$$

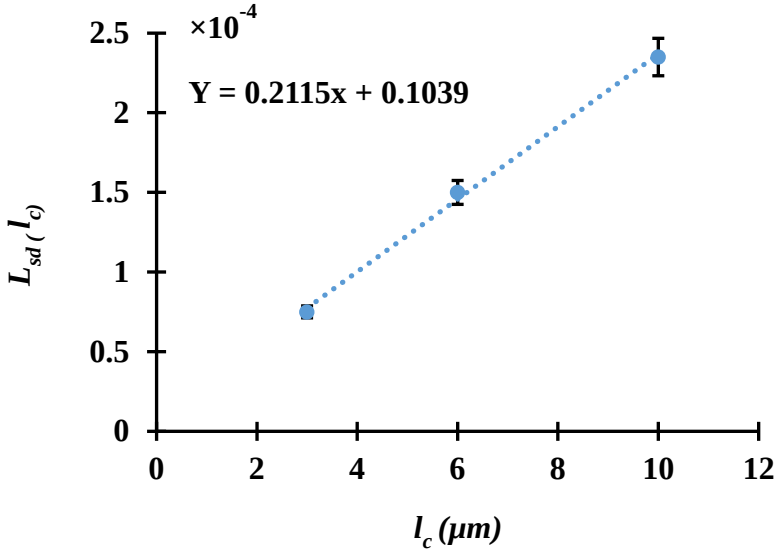

Figure 2.6: Zero error of PWS system calculated from the slope of the experimental calculation of the disorder strength for three beads with different sizes.

Where <R> is the rms average of the *R(x, y, λ)* over the visible range of the spectrum (520 -640) nm is acquired. The information about the refractive index embedded in the spectrum of the backscattered signal. We considered here the size of the beads as approximately the correlation length l_c value. From the calibration graph fitted into the Figure 2.6 plotted between $l_c$and the

data points of the disorder strength $L_{sd}(l_c)$) in Fig.2.6, we estimate the zero shift of the PWS system of ~0.1039 μm of the input range of 3-10 μm.

In Fig.2.7, we removed the zero shift, and plot the theory on the x-axis and the experimental disorder strength L_{sd} on the y-axis for comparison. We noticed that now both of the experimental and the theory is pass through zero.

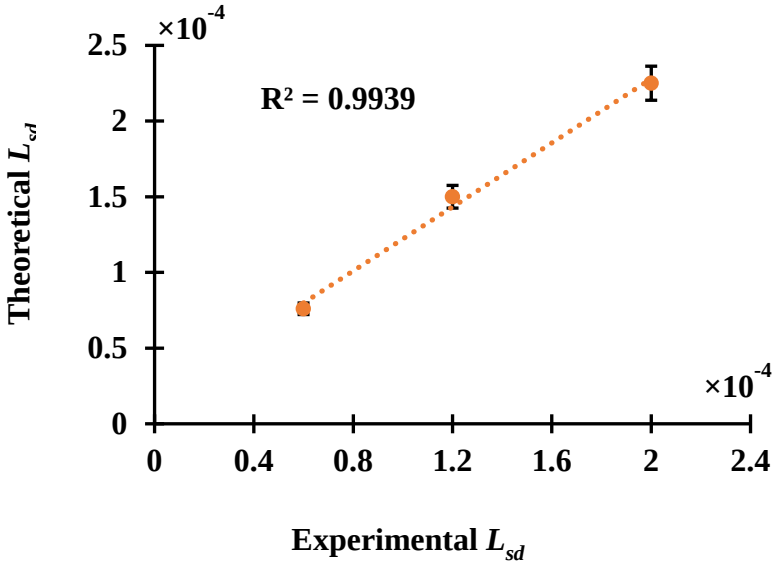

Figure 2.7: Adjustment of the zero error by comparing the experimental and theory calculation of the disorder strength L_{sd} for three beads with different sizes

2.8 Signal to Noise Ratio Estimation of the PWS System:

When an image of a microscopy system is used for quantification analysis rather than the only visualization, the signal to noise (S/N) ratio is an important parameter that judges the image quality. Signal to noise ratio (S/N) provides a qualitative description to the level with which an object on an image is distinguishable from the background noise associated with the image. In statistical term, signal to noise ratio can be used to determine the confidence interval to which a meaningful signal can be distinguished from the noise of the background. Since the signal to

noise ratio is calculated by the dividing the signal of an object on the image by the standard deviation of the background noise, it is possible to calculate the confidence interval to which image clarity is determined. Moreover, a parameter called relative error (the fraction of the signal is being noise) can be quantified by taking the inverse of the signal to noise ratio.

The signal to noise ratio of the PWS system is calculated in five steps.[38] First, the flat field corrected image is obtained using the following formula, Corrected image = M [(R-D) / (F-D)]Where, M is the mean pixel values of the raw image, R is the raw data of an object on the image, D is the data of dark frame image acquired by closing the shutter of the CCD camera, F is (flat field frame) the data of the background without the object image (see Fig.2.8).

Next, a rectangular area (100X100 Pixels) is determined on the corrected image that covered an object (object+background) and the mean of the pixel values in that chosen area is calculated and multiplied by the gain of the CCD camera (1 e^-/ADU) to convert the pixels value to electrons. Then, an area that covers the same size of the rectangle around the background of the image without including the object is selected and the mean and the stander deviation of that area are acquired and multiplied both by the gain of the CCD.

Later, the mean of the background is subtracted from the mean of the object to acquire the signal (S). In addition, the signal (S) was divided by the standard deviation of the background to obtain the S/N ratio =19.4516~ 20. By taking the inverse of S/N ratio, we obtain a 0.05 relative error which gives noise's fraction of the determined signal. Moreover, 10% fluctuation in the signal can be detected at confident interval 95 %(two SD). The images in Fig. 2.8 as shown above of a 3-μm polystyrene microspheres where: (a) represents the raw data before the image processing, (b) the background taken without sample on the glass slide, and (c)

is the corrected image. It can be seen that background contain many defects and irregularities in the intensity, which is taken, care of in the corrected image.

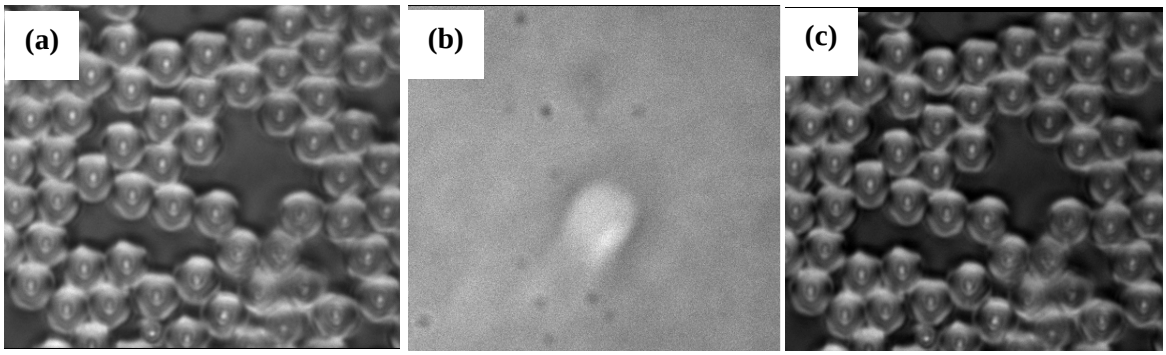

Figure 2.8: Shows **(a)** Raw frame (raw data image (background + object)) **(b)** Flat field frame (background) (**c)** Corrected image

2.9 Calculation of Disorder Strength of Biological Samples Using PWS

From a glass slide of a biological cell under the study, we pick 15-30 single cells. We acquired the spectral images for each cell separately. For each cell, we have the spectral information for each pixel in the image. We apply the data processing procedure that we mentioned in the above section to extract $R(x, y, \lambda)$ for each pixel in the image and to calculate its correlation function . Moreover, we calculate the rms average of $R(\lambda)$ for each pixel, as well. We calculate the L_{sd} for each pixel using the Eq. (4). Finally, we take the average L_{sd} for the cell. We repeat the same steps for 15 -30 cells and we get different values of L_{sd}. We averaged all the L_{sd}values for all the cells and that was our best estimate value. We estimated the error in the calculated L_{sd} by taking the standard error.

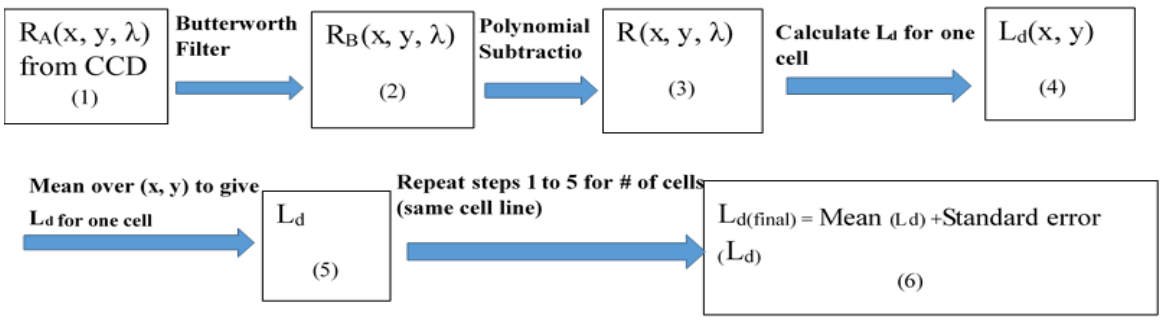

Figure 2.9: Schematic flowchart of the signal processing and error estimation in PWS system for biological samples.

2.10 Conclusions

This chapter describes methods and steps that followed to calibrate and correct the experimental data acquired using the PWS system for any expected errors in such a way as to use the system accurately for studying the different biological samples. Following the detailed steps described in the above sections, 2.4-2.7, to eliminate noise and correct for the LCTF and lamp response in our actual cell data. Moreover, following the above steps provides an improvement in the quality of the measured /recorded signal, the corrected signal, with appropriate error estimations.

We have also obtained a signal to noise ratio of PWS of 20, which is considered as a measure of image quality. To better control the noise in the image and improve the quality of the image we suggest a better light source with more uniform spectral emission in such a way that we do not need such a long exposure time to collect the images at the short-wavelength where the emission of the lamp is low. In addition, we have showed the zero error of PWS by fitting a calibration curve between the measured L_d and the input l_C to find and fix a zero shift of + 0.103. Moreover, we adjust for the zero shift by subtracting the zero error from the data points. We plotted the experimental disorder strength after subtracting the zero-shift vs theoretically calculated disorder strength and we found that the two measurements (theory and experiment) pass through the zero.

3 Partial Wave Spectroscopy (PWS) Studies of Human Breast and Brain Normal and Cancer Cell Lines

3.1 Introduction

Cancer disease is now considered as a global health concern due to the worldwide high morbidity and mortality rate. According to the 2018 United States cancer statistics, there are 1,735,350 new cancer cases and 609,640 deaths related case.[39] Breast and brain cancers are common in patients with 30% and 3% of the new cases being breast and brain cancer respectively.[39] A working hypothesis that is shared by governmental funding agencies, oncologists, and patients is that effective management of cancer patients through an effective and efficient disease diagnosis and treatment should lead to reduced cancer patients and increased the survival rate.

Tissue biopsy (histological assessment) is the current gold standard for clinical cancer diagnosis and grading including brain and breast cancers.[40,41] In a histological analysis, a micropathologist visually examines a thin section of tissue under a microscopy for any irregularities in cells' shapes and distributions.[42] Such histological studies are extensively used to determine if the tissues are normal or cancerous and the malignancy potential for almost all types of cancer cases. However, there exist inevitable disadvantages of histological assessment due to severe clinical complications resulting from sampling (biopsy repetition) and cells and tissues structural heterogeneity that can be missed using tissue biopsies. The procedures also take time and expense and need to be examined by an expert pathologist. Therefore, there is a need for better alternative clinical diagnostics techniques that are fast, sensitive and inexpensive and that helps to overcome the disadvantages of the standard biological biopsies. In particular, the use of

the so-called “optical biopsies”, i.e., use of light as diagnostic tool and as means to monitor treatment response monitoring, would allow a sensitive, rapid and economical intervention in cancer diagnosis and treatment management.

Optical biopsies represented by optical technology hold a great promise in many diagnostics applications in biomedical optics field because light is sensitive to the refractive index of the biological structures. A biological cell is made up of a heterogeneous media with spatial variation in the refractive index (RI) due to the presence of the different internal structures such as DNA wrapped on histones, proteins, and lipids. The cellular refractive index is a key parameter that researchers studied extensively to learn about the biophysical features of the cell because it can be correlated to the optical properties, such as scattering and absorption, of the biological cells. Moreover, earlier the researchers measured the refractive index of different cells and tissues, and later the refractive index of abnormal and normal cells was compared to search for a correlation with progression of diseases such as cancer.[43, 44] Different structural abnormalities associated with cancer cells are employed to study cancer, such as irregular shape (heterogeneity) and uneven chromatin textures. These cellular abnormalities of cancer cells can be considered as changes in the biophysical characteristics, such as mass density (or refractive index), etc., of the biological cancer cells and tissues.

Selected optical scattering techniques, such as quantitative phase microscopy and Mie scattering analysis, were used to probe these structural changes based on the measurement of changes in these biophysical characteristics. Despite the highly advanced level of these optical techniques, the study of the intracellular refractive index fluctuations remains a limitation. In optics, two of the commonly used light scattering based techniques are Rayleigh scattering and Mie scattering. While the Rayleigh scattering (for particle size $<< \lambda$, the incident wavelength)

and Mie scattering (for particle size >> λ) provides a reasonable estimation of the bulk refractive index(RI) of the sample, however, they fail to accurately analyze RI fluctuations within a cell. In many situations in cancer progression where early structural changes occur, the quantification of RI fluctuations becomes more informative than the bulk RI which shows noticeable changes while keeping bulk RI unchanged.

In the context of refractive index fluctuation quantification, a mesoscopic physics-based approach plays a vital role in quantifying such fluctuations in the refractive index. [33,45] Therefore, partial wave microscopy spectroscopy (PWS) was introduced recently to study the refractive index fluctuation of a single biological cell. PWS allows a spectroscopic analysis of the backscattered light by a biological cell based on the quasi-1D mesoscopic light transport theory. The technique divides the back reflection from the sample (in the images plans) into different 1D channels where each channel is represented by a pixel. In this study, we explore the ability of the PWS to isolate 1D backscattering photons spectra that are sensitive to sub-diffraction length scales of refractive index fluctuations and use that information to evaluate the cellular and subcellular structural alterations of the brain and breast normal and cancer cell lines. We acquired the bright field image spectra of the human breast and brain cells line models, and subsequently we used the spectral data to measure and quantify, and then compare the disorder strength, which is a statistical parameter of the refractive index of fluctuations of a single cells, both of the cancer cells and the control (normal) cells.

3.2 Theory

3.2.1 Structural Change Analysis (Mesoscopic Approach)

The backscattered spectral imaging data can map spatial optical density variation in the cell sample by mapping the respective spatial refractive index fluctuation inside the cells of the

sample. Light, backscattered from a sample may be used to extract spatial RI profiles of a sample. It should be noted that measuring and quantifying very weak nanoscale optical spatial refractive index fluctuations that are embedded within a background of higher refractive index poses significant scientific challenges, both from the perspective of fundamental light scattering and transport theory and in the design of high-performance optical instrumentation. For example, in biological cells, the mean background spatial refractive index is large (n~1.38), whereas its fluctuation (dn~0.02) is much weaker, that is dn/n <<1. [28,46] However, by using spectroscopic microscopy based on the principles of mesoscopic physics one can extract such information with high accuracy.[47]

To understand the mechanism of this approach, consider a light wave *E(k)* with wave number *k* incident onto a dielectric medium at a normal angle of incidence, as shown in Fig.3. 1.

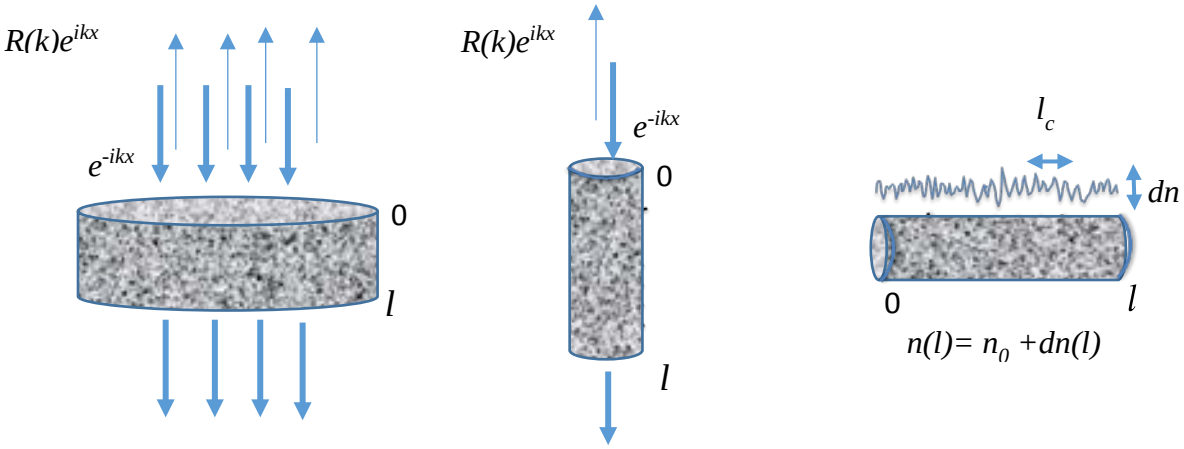

Figure. 3.1: Schematic of 1D backscattered reflection from a dielectric media

Consider the RI of the sample along the direction of light propagation (*x* represents depth along the incidence direction) is given by $n(x) = n_0 + dn(x)$; where n_0 is the average RI along the 1D

channel and *dn(x)* is the RI fluctuation along same 1D channel. Scattering theory suggests that the back-scattered intensity, *R(k)*, (where $k=2\pi/\lambda$) will depend on the nature of *dn(x)*. For a system with constant RI background, i.e. *dn (x) = 0*, the backscattered intensity is given by,

$$R = \frac{(m^2-1)^2 \sin(2mx)^2}{(m^2-1)^2 \sin(2mx)^2 + 4m^2} \quad \textbf{(1)}$$

In which *n* and *L* are the RI and the thickness of the sample, respectively. A typical plot of reflected intensity, *R (k)*, ($k=2\pi/\lambda$), as a function of wavelength λ is shown in Fig 3.2 (a).

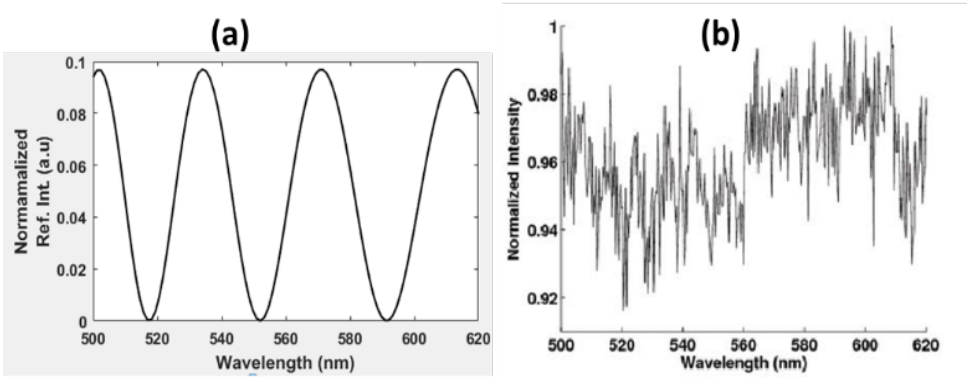

Figure 3.2: Reflected intensity vs wavelength for the cases: (a) *dn(x) =0*; (b) *dn(x) ≠ 0* (Figure taken from Ref 48)

The period of the *R(k)* oscillation, a function of *f(n,k, L)*which appears in the argument of the *sin* term in Eq.1, can be used to measure the average RI or thickness of the sample. However, in general, biological systems do not have uniform RI, i.e., *dn (x) ≠ 0*. In this case, Eq. 1 is not applicable in this form. The effect of RI fluctuation modifies the *R (k)* pattern. Figure 3.2(b) shows a typical plot of reflected intensity as function of wavelength for the case *dn (x) ≠ 0* [Taken from Ref 48]. Although the oscillatory nature of *R (k)* gets significantly modified, the

periodicity imparted by the average RI (i.e., average background) of the sample to the *R (k)* values can still be extracted through a Fourier analysis of *R (k).*

3.2.2 Mesoscopic Physics Approach for Refractive Index Fluctuation Mapping in Biological System

As discussed earlier, the mesoscopic physics-based analysis which is widely applicable to systems of mesoscopic length (~ μm), provides an excellent way of extracting information from the fluctuations inside the systems. In context to biological media, which is considered as weakly disordered heterogeneous dielectric/refractive index media, with average RI, $<n> = n_{cell} = n_0 = 1.38$ and strength of RI fluctuation $dn \sim 0.02$, therefore, a mesoscopic approach can be readily applicable. Technically, through correlation analysis of RI fluctuations, the strength of RI fluctuations is quantified in terms of a parameter called 'disorder strength', L_{sd}, which is defined as $L_d = <dn^2>l_c$, where dn and l_c represents RI fluctuations and its spatial correlation length of the system, respectively. Thus, the parameter L_{sd} provides a measure of degree refractive index fluctuation or the 'degree of disorder' inside the system. The calculation of L_{sd} utilizes the fact that the 1D backscattered intensity (at each spatial point forming the 2D image plane of the sample) from a dielectric medium can be modeled as [32]

$$< R > \cong \frac{1}{2}\left[e^{\frac{4k^2 L_{sd} L}{n_0^2}} - 1 \right] \quad \textbf{(2)}$$

Where <*R*> represents an *rms* average of the backscattered intensity *R(k)*, n_0 is the average refractive index of the medium, *L* is the depth of the sample along the direction of the light propagation, $k (=2\pi/\lambda)$ is often taken at the center of the wavelength band, and L_{sd} is defined

above. For a weakly disordered dielectric media/optical system like biological cells, $kl_c << 1$. In such case,

$$\langle R \rangle \cong \frac{2k^2 L_{sd} L}{n_0^2} \tag{3}$$

Thus, by measuring the *rms* average of the reflected intensity *R(k)*, one can quantify refractive index fluctuation and measure the degree of disorder inside the system in terms of L_{sd} values.

3.2.3 The Autocorrelation Function of the Reflection Coefficient

The autocorrelation function allows the calculation of the disorder strength for the the elimination of the sample length. The autocorrelation function of the reflection coefficient is given by equation, 4, where A is a constant

$$\ln\big(C(\Delta K)\big) = (\Delta K)^2 AL \tag{4}$$

3.2.4 Structural Disorder Strength

Finally, the structural disorder strength is the main parameter that we are investigating in the present study. Therefore, using Eqs. (3), and (4), we can write.

$$L_{sd} = \frac{n_0^2}{2k^2} \frac{(\Delta k)^2}{-\ln(C(\Delta k))} \langle R \rangle \tag{5}$$

Experimentally, the structural disorder is calculated from the reflection coefficient and the autocorrelation function of the reflection coefficient, where L_{sd} can be calculated using Eq.5.

3.3 Material and Method

3.3.1 Samples Preparation

3.3.1.1 Breast Normal and Cancer Cells

Breast cell lines included MCF10 (normal) and MCF-7 (adenocarcinoma) were obtained from the American Type Culture Collection (ATTC). Cells were re-suspended and maintained in 2 mL Dulbecco's Modified Eagle Medium (DMEM) (Gibco) supplemented with 10% Fetal Bovine Serum (FBS), and 200µM GlutaMAX™. Then, cells were dispensed onto glass slides in a sterile 10 cm petri dish. The dishes with slides were then placed in a 37°C incubator overnight in order to allow for cell growth and adhesion to slide. After 24 hours, 10 mL of medium was added to the petri dish and swirled gently. The medium was changed every 2-3 days while the cultures were maintained in a 5% CO2 incubator at 37ºC.The third day after adding 10mL medium, slides were removed from the petri dishes and placed in a Coplin jar to be rinsed/washed in PBS at 37ºC. Slides were then placed in another Coplin jar containing 20 % formaldehyde (Tousimis) for one hour at 37ºC to ensure adequate fixation of these cells. Next, slides were washed in PBS for 5 minutes.

3.3.1.2 Brain Normal and Cancer Cells

The brain cell lines include three types: normal astrocyte (Lonza Group Ltd, Basel, Switzerland), progenitor astrocyte (Applied Biological Material, Richmond, Canada), and U-78 astrocytoma (ATCC, Rockville, MD, USA). The brain cells were cultured using the same procedure as the breast cells lines.

3.3.2 PWS Experiments and Data Acquisitions

The partial wave microscopic spectroscopy instrument is described in detail in chapter 2. In brief, PWS combines microscopy and spectroscopy of the elastically backscattered light. The individual cell slide is mounted on the motorized stage and illuminated with collimated white light from a Xe-source; the backscattered light then filtered using the liquid crystal tunable filter to sample its wavelength components with a resolution of 1nm. Then, the CCD camera records the backscattered spectra between 450-700 nm for each pixel of the image. In conventional microscopy, an image is formed by integrating the intensity over the spectrum of the white light. However, PWS measure the fluctuations in the backscattering spectra in discrete ranges of the spectrum. The spectral fluctuations were then analyzed by means of the 1D mesoscopic light transport theory to calculate the statistical structural parameter the degree of disorder or disorder strength for each pixel for a 2D image. Therefore, a PWS image represents a distribution of the disorder strength $L_{sd}(x, y)$ for exposure of a specific cell category (e.g. breast or brain) to the incident light. Using the distribution, we calculate the mean and the standard deviation of the disorder strength of the individual cell over many pixel (x and y) locations. We repeat the experiment three times, and the total cells used in each set of observation is around 15 to 30 cell of a particular cell line in each category. Finally, we calculate and plot the mean and standard deviation of the disorder strength L_{sd}.

3.3.3 Statistical Analysis

All statistical analyses were performed using MATLAB and Microsoft Excel. We compared the mean intracellular disorder strength and the standard deviation of the intracellular disorder strength between different groups of cell lines using the Student's *t*-test with two-tailed distribution. The means (± standard error) over a range of different L_{sd} values across different

number of cells were determined. A two-sided *t*-test with p-values less than 0.05 was considered statistically significant.

3.4 Results and Discussion

A total of five different cell lines were investigated in this study for human breast (2 types) and brain (3 types) cell lines. We studied the commercially available normal and cancerous human astrocytic cell lines. In particular: normal astrocyte, astrocyte progenitor cells, and the U87 astrocytoma cells samples were studied. We also studied breast cancer normal and cell lines: MCF-10A (control) and MCF-7(cancer). The cells grown on glass slides and were fixed with 20% formaldehyde as described earlier. PWS imaging of these cells was performed with the PWS system at a pixel resolution of 1392 × 1040. The PWS microscopy imaging was performed to obtain $R(x,y;\lambda)$ data cube and the data were analyzed to quantify the degree of structural disorder L_{sd} in a single cell using the methodology described in Section 2, as well as the results were evaluated statistically.

The degrees of structural disorder $L_{sd}(x,y)$ was calculated for every single pixel in the image plane to get a distribution for a single cell. Then the values of $L_{sd}(x,y)$ were averaged for each single cell, and the ensemble averaged over 15 - 30 cells from every category were analyzed and the experiment was repeated three times. Figure 3.3 compares the bright field images and of (A) a normal astrocyte, an astrocyte progenitor, and a U87 astrocytoma cells, and (B) MCF-10A and MCF-7cells. The colored bar indicates the mean disorder strength L_{sd} values. As can be seen, $L_{sd}(x,y)$ images (PWS images) constructed by plotting the L_{sd} values for all the pixels (x,y) on the images.

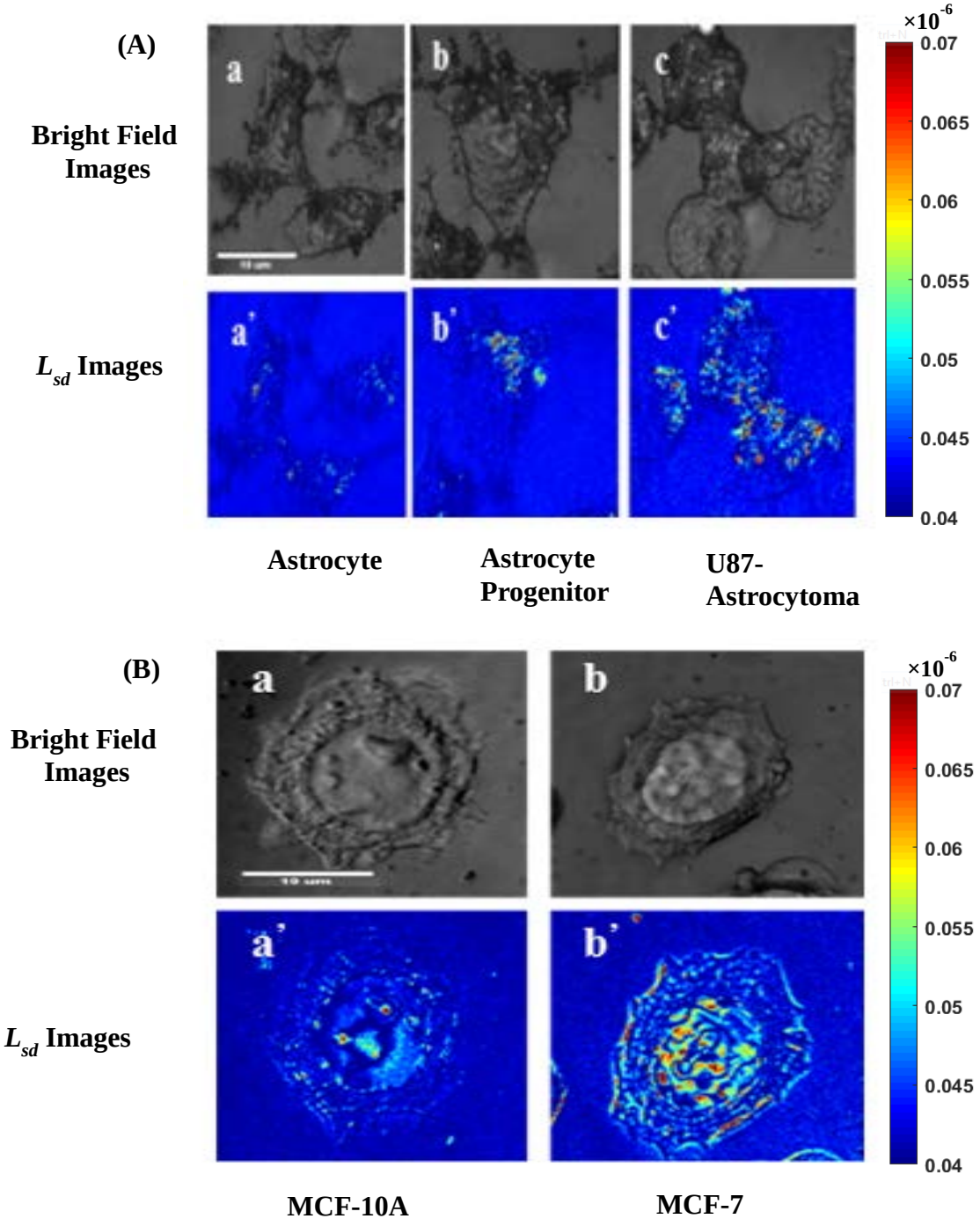

Figure 3.3: A (a), (b), and (c): Representative of the bright field images of a normal astrocyte, an astrocyte progenitor, and a U87 astrocytoma cells, respectively. (a'), (b') and (c'): Their corresponding $L_d(x, y)$ images. Similarly in B, (a), (b): Representative Bright field images of a MCF-10A and MCF-7, a normal and cancerous human breast cells, respectively. (a') and (b'): Their corresponding $L_{sd}(x, y)$ images. The scale bar in the PWS image corresponds to 10 μm.

The red colored areas in the PWS images indicate regions with higher disorder strength, that is, higher structural disorder or more spatial fluctuations in the refractive index. Clearly, there is no difference between the cancer and normal cells in the bright field images in each of the two groups that is for: (A) brain cancer and (B) breast cancer.

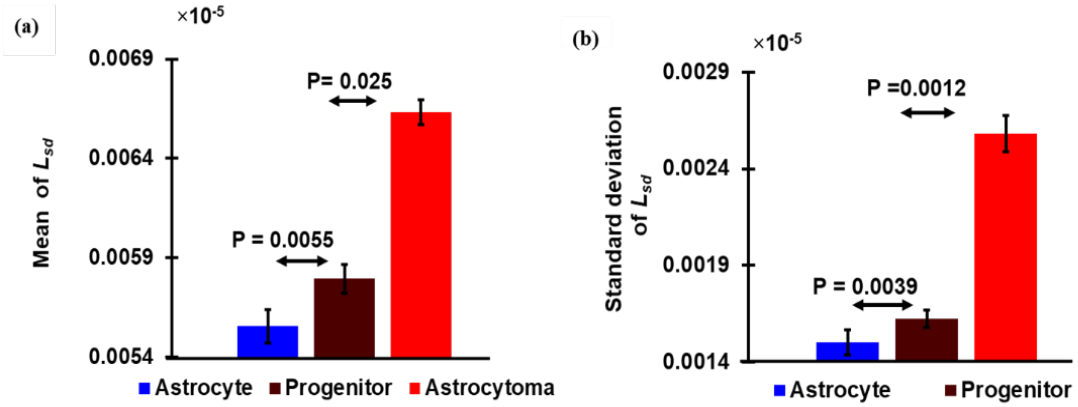

Figure 3.4: The values of the average and standard deviation from the brain cell lines. The average disorder strength is significantly elevated for cells from astrocytoma compared to astrocyte cells (P-value <0.05). Similarly, standard deviation of the disorder strength is significantly elevated in the astrocytoma cells compared to the astrocyte cells with the average and stander deviation disorder strength of the progenitor astrocyte cells falls between the astrocyte and the astrocytoma cells.

However, there is significant difference in each group of the cells between cancer and normal cells in the PWS images, for each cancer types. Hence, based on the L_{sd} distribution of each cell type, the cell with cancer can be distinguished from each other. In the (A) brain cancer cell lines cases the astrocytoma cells have the greatest disorder strength while normal astrocyte cells have the least and progenitor has the disorder strength in between. In the case of (B) breast cancer cell lines, MCF-7(cancer) has the higher disorder strength compared to the MCF-10A (normal/control).

The bar graph in figure 3.4a shows disorder strengths comparison for all the astrocytic cell lines. The average L_{sd} values for all the three types of cell line, namely the astrocyte, progenitor astrocyte, and astrocytoma cell line, were measured to be [0.0055, 0.0057and, 0.0066] $\times 10^{-5}$, respectively. Additionally, the spread of the L_{sd} values (Fig.3.4b) in each cell type, measured in terms of the standard deviation of the measurement, was noted to be [0.00150, 0.00162 and,0.00258] $\times 10^{-5}$ for the astrocyte, progenitor astrocyte, and astrocytoma cell line, respectively. These results show that the disorder strength of the metastatic brain cancer cell line is higher compared to the normal brain astrocyte cells.

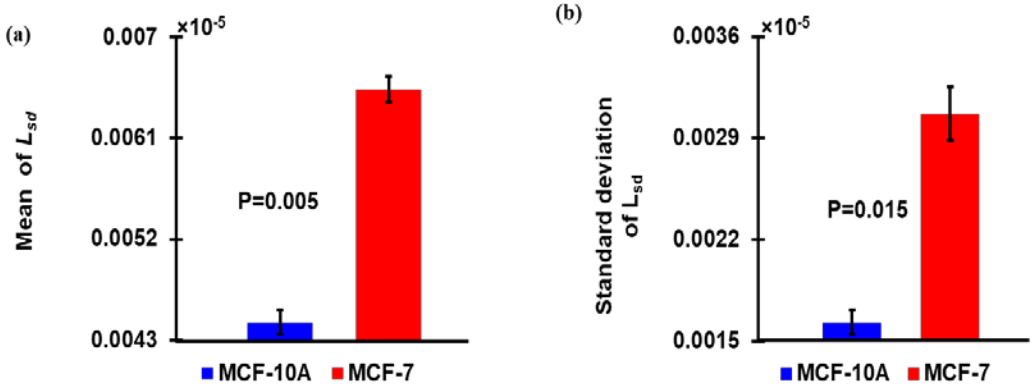

Figure 3.5: The values of the average and standard deviation from the breast cell lines**.** The average disorder strength is significantly elevated in MCF-7 cells compared to MCF-10A cells (P-value <0.05). Similarly, standard deviation of the disorder strength is significantly elevated in the MCF-7 cells compared to the MCF-10A cells (P-value <0.05).

The bar graphs in Figure 3.5 represents a comparison of (a) the average L_{sd} and (b) the standard deviation of L_{sd} values between the normal MCF-10A and the cancerous MCF-7 cell line. The average L_{sd} values for MCF-10A and MCF-7 cell lines were measured to be [0.00445, 0.00665] $\times 10^{-5}$, respectively. Additionally, the spread of the L_{sd} values in the two types of cells, measured in terms of the standard deviation of the measurement, was noted to be [0.00163,0.00307] $\times 10^{-5}$ for the for MCF-10A and MCF-7 cell line, respectively. The p-value

obtained from the student's *t*-test (sample size > 15) was less than 0.05 for all pairs demonstrating that the structural disorder is significantly higher in cancerous cells compared to that of the normal cells.

3.5 Conclusion

The development of cancer through genetic and epigenetic (non-genetic) alterations leads ultimately to the cellular and subcellular structural changes. Recently, the analysis of the structural disorder properties showed great importance in many biomedical applications; in particular, investigation of the physical properties of the samples such as mass density variations, or refractive index variations reveal a great potential in cancer diagnosis and screening. In this work, we applied the recently introduced partial wave spectroscopy (PWS) with a nanoscale sensitivity of the total structural/or mass density changes in cells to differentially identify the intracellular structural changes of breast and brain human cancer cell lines by characterizing the disorder strengths of cells internal structures. Results in terms of disorder strength demonstrate that the increase in aggressiveness or tumorigenicity levels inside the different brain and breast cancer cells are highly correlated. Where cancer cells in both the breast and brain cell lines turned out to have more structural disorder strength compared with the normal cells.

4 Optical Study of Chemotherapy Efficiency in Cancer Treatment via Intracellular Structural Disorder Analysis Using Partial Wave Spectroscopy

The major part of this chapter taken from a paper submitted to the Biophotonic (2018) journal.

With the progress of cancer, macromolecules, such as DNA, RNA, or lipids, inside cells undergo spatial structural rearrangements and alterations. Mesoscopic light transport based optical partial wave spectroscopy (PWS) was recently introduced to quantify changes in the nanoscale structural disorder in biological cells. This measurement is performed using a parameter introduced earlier 'disorder strength' (L_{sd}) which represents the degree of nanoscale structural disorder inside the cells. It was shown that cancerous cells have higher disorder strength than normal cells. In this work, we studied the effect of chemotherapy drugs on different prostate cancer cells taken from cell lines, by their spatial structural disorder analyses. For this, we first used the PWS to analyze the hierarchy of different types of prostate cancer cells from cell lines, namely C4-2, DU-145, and PC3, by quantifying their average disorder strengths. Results showed that L_{sd} values increased by the increasing aggressiveness/tumorigenicity levels of these cells. Using the L_{sd} parameter, we then analyzed the chemo-resistance properties of these prostate cancer cells from the same cell lines to docetaxel drug as compared to their chemo-sensitivity of other cells. Results showed that chemo-resistant cancer cells had increased L_{sd} values, i.e., higher disorder strength, relative to chemo-sensitive cancer cells, for each cell lines. Thus, use of the L_{sd} metric can be an effective and potential biomarker in determining the efficacy of particular chemotherapy.

4.1 Introduction

4.1.1 Role of Nanoscale Mass Density Fluctuations in Cancer Detection

It is well known that the progress of cancer is associated with cellular morphological changes [27,31] As mentioned in chapter 3, the biophotonics technique partial wave spectroscopic (PWS) microscopy was introduced to quantify the nanoscale structural disorder in weakly disordered optical systems such as biological cells. In this work, first, we used PWS technique to analyze structural disorder properties of three prostate cancer cells, namely C4-2, DU-145 and PC-3, and the effect of the treatment of chemotherapy drug, docetaxel, to these cancer cells.

Partial Wave Spectroscopy analysis is based on statistical quantification of backscattered light intensities and their spectral correlation decay length owing to the nanoscale refractive index fluctuations within biological samples. In the PWS technique, a thin sample is virtually divided into several parallel scattering subsamples such that the bulk backscattering problem is approximated as a quasi-one-dimensional (1D) scattering problem. The reflection in each 1D channel, i.e., subsample, provides two parameters: root mean square (RMS) and the correlation of the reflection spectra. From these two quantities, the effective structural disorder, or the "disorder strength $L_{sd,}$" inside the biological cell is characterized. The parameter L_{sd} is defined as, $L_{sd} = <dn^2> \times l_c$, where dn is the local rms fluctuating part of the refractive index in the 1D channel, arising from the mass density fluctuations in that channel, and l_c is its spatial correlation decay length. Consequently, L_{sd} represents a measure of refractive index fluctuation, and hence mass density fluctuation, in the sample, both in terms of magnitude and correlation length. This study used disorder strength, $L_{sd\ ,}$ as the primary metric to determine the efficacy of docetaxel, most commonly used chemotherapeutic drug, to see its effect on different types of prostate cancer cells. In particular, we demonstrated that the intracellular structural properties of drug-

resistant *vs*. drug-sensitive cells show different L_{sd} values, strongly suggesting that the sensitivity or resistance of cancer cells to a given drug can be evaluated by quantifying the disorder strength parameter L_{sd}. As such, the parameter L_{sd} acts as a potential biomarker of drug efficacy, as will be shown in our results. Briefly, drug-resistant cancer cells have higher disorder strengths, compared to that of normal (control) cancer cells, suggesting higher aggressiveness of the drug resistant cancer cells. For that, we first show, by analyzing three different prostate cancer cells (C4-2, DU-145, and PC-3), that higher aggressiveness/tumorigenicity levels of cancer cells result in higher disorder strengths in those cells, which is consistent with earlier reported results with other cancer cases.[49–51] Subsequently, the drug treatment studies of these cells were performed. These results indicate that drug-sensitive and drug-resistant cancer cells display quantifiable differences in their intracellular structural disorder. These nanoscale alterations are, in turn, related to nanoscale mass-density fluctuations inside the cells. Therefore, the degree of disorder strength, L_{sd}, can be considered as a potential biomarker, whose values can be used to assign relative efficacy to a given chemotherapy drug treatment, i.e., a marker that can differentiate between drug-resistance and drug-sensitive of cancer cells. This will be demonstrated in the following sections.

4.1.2 Prostate Cancer and Effect of Chemotherapy Drug

Prostate cancer is most commonly diagnosed in men and often metastasizes at later stages. An alarming total of 164,690 new cases are estimated in the United States in 2017, including 19% of them are prostate cancer.[52] Prostate cancer is prominent in older men, with 60% of men over the age of 65 are diagnosed with this.[53] In addition, prostate cancer is the 2nd leading cause of cancer caused deaths in American men, behind only to the lung cancer.[52] Therefore, effective detection and treatment of prostate cancer are important, especially for senior men. Chemotherapy is used

to treat advanced prostate cancer cases. However, chemotherapy is often ineffective because cells of an individual patient's tumors develop chemo-resistance.[54–56] Thus, it is important to know the efficacy of a particular chemotherapeutic drug in order to assess its potential resistance or, conversely, its potential sensitivity.

4.2 Prostate Cancer Treatment and Role of Chemotherapy

Prostate cancer treatment typically involves radiation, surgery, and then chemotherapy.[57] These treatments are performed in an order that matches the stage and size of the malignant tumor. Usually, chemotherapy is administered after surgery that removed the tumor from the prostate. This therapy is expected to kill the metastasized cancer cells around the prostate gland, as well as surrounding tissue. Resistance to chemotherapy is one of the main causes of treatment failure in all types of cancer treatment, including that of prostate cancer. Development of drug resistance by cancer cells is a serious problem since it ends the remission stage and leads to disease relapse. Clinically, the chemotherapy drug docetaxel (Taxotere®) is frequently used to treat the advanced stages (metastasis) of prostate cancer. However, resistance to this drug is a major clinical problem.[58] Docetaxel resistance is correlated with treatment time and drug dosage.[59] Researchers are studying drug resistance with the aim of understanding the physiological effect of other chemotherapeutic drugs that can bypass resistance and restore near-normal growth and division processes for cells that remain after chemotherapy.[60–62] In different chemo-resistance studies, the aggressiveness and invasion of resistant cancer cells have been observed.[63,64] In addition, it has been reported that docetaxel resistance in cancer cells is highly associated with genetic alterations.[65] These genetic mutations lead to the rearrangement and alteration of the most basic building blocks of cells, such as DNA, RNA and lipids, in turn producing intracellular structural changes in the treated cancer cells.[65] In this work, the effect of this drug on intracellular structural

changes were measured and quantified using the parameter disorder strength, L_{sd} ($=<dn^2>\times lc$), as defined earlier. The resulting value was compared to corresponding values for nondrug-treated, i.e., the drug sensitive cancer cells. The results support the hypothesis that prostate cancer cells that acquire chemo-resistance to docetaxel, ultimately showing no response toward further treatment with this drug, and become more aggressive. Consequently, we have demonstrated that L_{sd} can potentially be an efficient metric (/biomarker) that can characterize drug-sensitive *vs*. drug-resistant cancer cells using PWS technique.

4.3 Method

4.3.1 Cell Culture and Development of Docetaxel Chemo-Resistant Prostate Cancer Cells of the Following Cell Lines: C4-2 (PSMA+), DU145 (PSMA−) and PC-3 (PSMA−)

Prostate cancer cell lines [C4-2 (PSMA+), DU-145 (PSMA−) and PC-3 (PSMA−)] were developed in cell culture facilities at the University of Tennessee Health Science Center (UTHSC) and cultured in RPMI-1640 medium containing 10% (v/v) fetal bovine serum (FBS), 2 mM L-glutamine (Invitrogen, Carlsbad, CA), and 1% (w/v) penicillin–streptomycin (Gibco, Thermo Fisher Scientific, Grand Island, NY) at 37 °C in a humidified 5% CO2–95% air atmosphere (Thermo Fisher Scientific, Waltham, USA). Prostate cancer-resistant lines were generated by initial treatments with docetaxel (MP Biomedicals, Santa Ana, CA) at 1 nM (from 5 μM stock) in 75 cm^2 flasks for 24-48 hours. After treatment, the surviving cells were re-seeded into new flasks and allowed to recover for 1-2 days. Cells were maintained at 1 nM up to 4 treatment cycles (4 TC). Gradually, the concentration of docetaxel was increased to 2.5 nM (6 TC). The 5 and 10 nM of docetaxel was then continued to 8 and 12 TC, respectively. Then all cells underwent 12 TC and 15 TC with docetaxel 15 and 20 nM, respectively. Finally, at 30 nM docetaxel, we performed 25 TC to ensure the acquisition of chemo-resistance in all C4-2, D-145, and PC-3 cells. Following

each treatment, cells were allowed to fully recover before assessing their resistance to docetaxel and performing any experimental work. In total, the cells were treated for eight months. Since the passage number of the drug-treated cells increased over time, a subset of prostate cancer cells was aged alongside these cells as an appropriate control to ensure that the effects seen resulted from resistance and not the aging effect of the cultured prostate cancer cells.

4.3.2 Cell Imaging and Analysis

Frozen cell batches with similar passages were thawed and used for all experiments. For image analysis studies, we seeded 2.5×10^4 cells in each well of 4-chambered slides (Sarstedt. Inc, Newton, NC) and allowed them to grow. After reaching 70-80% of confluence, cells were fixed using 4% paraformaldehyde for 20 min.[66,67] After incubation, cells were washed with PBS, followed by PWS imaging and analysis.

4.3.3 Structural Disorder from the Backscattering Intensity

The CCD camera detects and stores the backscattered image of the biological cell taken at different wavelengths (λ) in the visible range, 450nm -700nm. Eventually, a cubic data matrix of backscattered intensity $I(x,y;\lambda)$, where (x,y) represents the spatial position on the sample, are acquired by the PWS system. For further data processing, we extract the backscattered spectral fluctuation $R(x,y;\lambda)$ as described elsewhere in chapter 3. Subsequently, the disorder strength L_{sd} is derived from two quantities: the average *rms* of the reflection intensity $\langle R \rangle_{rms}$ and spectral correlation decay of the reflection intensity $C(\Delta k)$, as follows (as described in Chapter-4)

$$L_{sd} = \frac{n_0^2}{2k^2} \frac{(\Delta k)^2}{-\ln(C(\Delta k))} \langle R \rangle \quad \textbf{(1)}$$

Where $C(\Delta k)$ is the autocorrelation function of $R(x,y,k)$ at a particular position (x,y) and averaged over many ensembles. The average value of L_{sd} (averaged over ensemble) is calculated for each pixel point (x,y). As pointed out earlier, the L_{sd} value measured at any spatial point (x,y) represents a measure of refractive index fluctuation at that point along the depth of the sample ($L_{sd} = \langle dn^2 \rangle \times l_c$), averaged over depth direction.

4.4 Results and Discussion

The disorder strength measurement was first performed on the three prostate cancer cell lines, namely C4-2, D-145, and PC-3, for which the hierarchy of tumorigenicity (aggressiveness or metastatic potential) have been well characterized.[68–70] The measurements were conducted on ~20 cells randomly selected from each cell type in one set of measurement (~60 cells in 3 sets). The results are shown in Fig. 4.1.

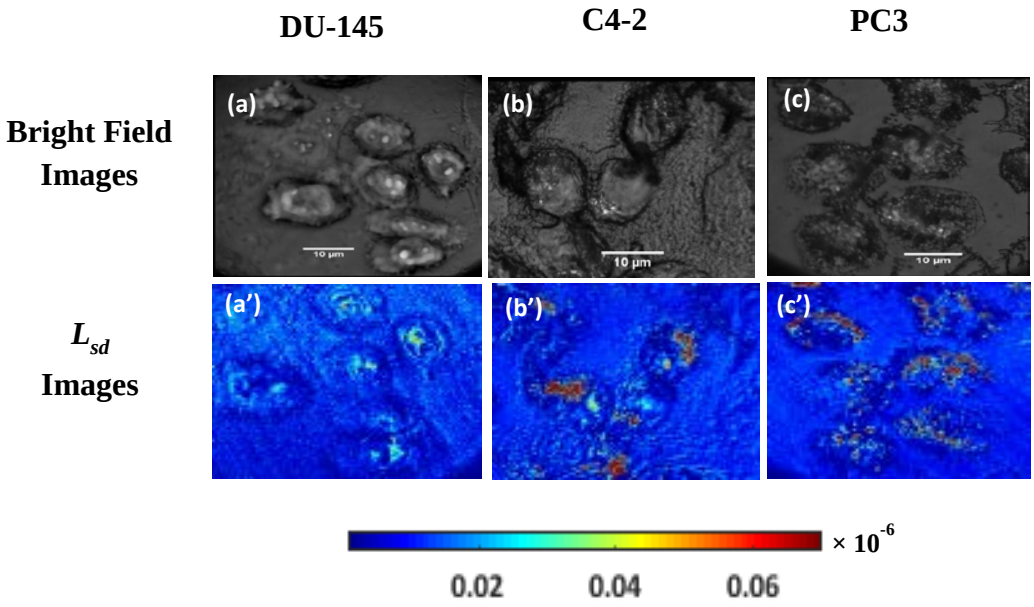

Figure 4.1: Representative bright-field images (a,b,c) and corresponding 2D L_{sd} maps (a',b',c') (PWS images) for the three prostate cell lines, DU145, C4-2, and PC3,1,2,3, respectively.

In Fig. 4.1: (a)-(c), three representatives one micrograph of bright-field images of each cell lines, namely DU-145, C4-2, and, PC-3 are presented, and their corresponding PWS L_{sd} images are shown in Fig. 4(a'), (b'), (c'), respectively. The L_{sd} map shows the distribution of L_{sd} values in the cells. In L_{sd} color map, the disorder strength increases from blue color to red. As pointed out earlier, a higher L_{sd} value at any pixel point (x,y) in the L_{sd} image indicates higher degree of structural disorder along the depth of the cell at that particular spatial point. It can be seen in the Figs.4.1 (a'), (b') and (c') that the L_{sd} distributions for the three cell lines are distinctly different. Subsequently, therefore, we calculated the average disorder strength, i.e., mean L_{sd} value, of each cell lines by taking the ensemble average of L_{sd} values of all the cells in three different sets (n ~ 60).

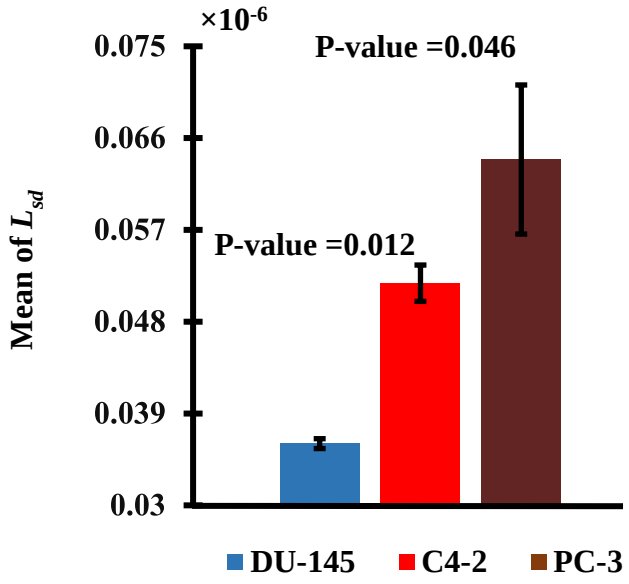

Figure 4.2: Bar plots of mean intracellular disorder strength L_{sd} calculated for three types of human prostate cancer cells (DU-145, C4-2, PC-3). L_{sd} results show that the average L_{sd} value correlates with the tumorigenicity level of the cell.

The results are shown in Fig. 4.2. The bar graph in Fig.4.2 shows a comparison of the mean L_{sd} values of the DU-145, C4-2 and PC-3 cell lines. As it is clear from the Fig. 4.2, the disorder strengths in these cell lines are in the order of DU-145 < C4-2 < PC-3, which is in accordance with their metastatic potential level (aggressiveness/tumorigenicity) as well [68,69]. Consequently, the present result suggests that the L_{sd} value (i.e., the disorder strength) is directly correlated with the aggressiveness level of the cell lines.

In the next step of this study, we examined the changes in the intracellular disorder strength that may have been introduced to the three prostate cancer cell lines after prolonged exposure to docetaxel drug. We hypothesized that these cell lines might develop resistance to the docetaxel drug after eight months of exposure and that this behavior would be associated with additional intracellular structural changes. In particular, a distinct change in the disorder strength in drug-resistant prostate cancer cells was expected.

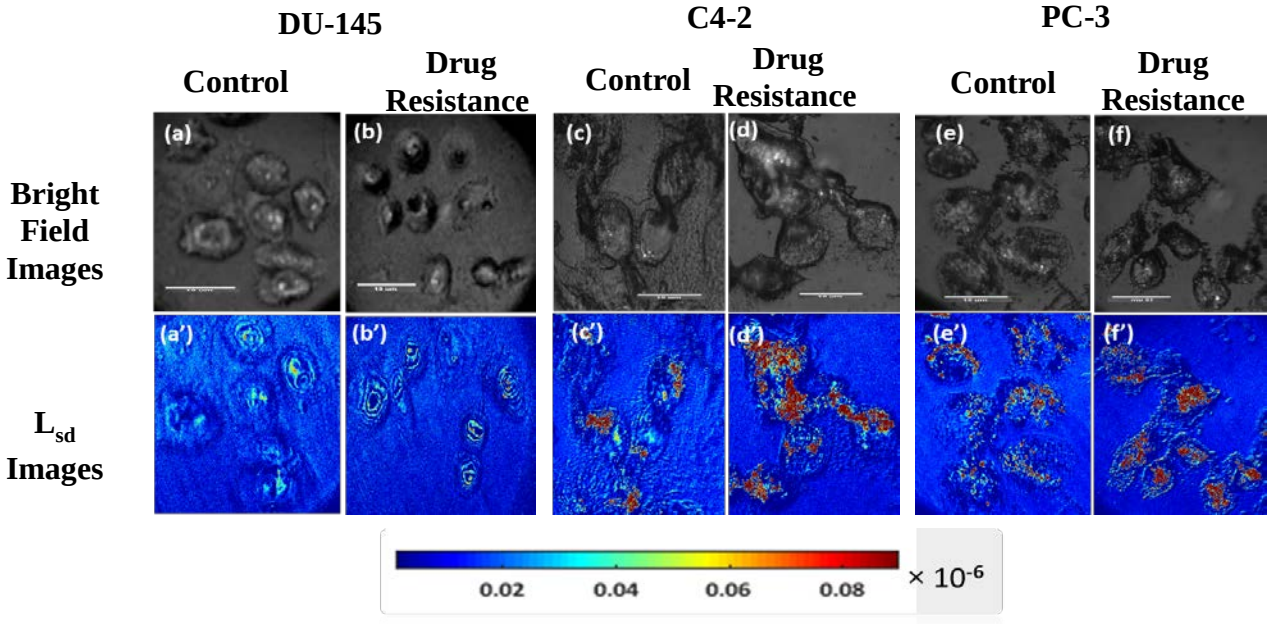

Figure 4. 3: (a-f) Bright-field images of three human prostate cell lines: Original cancer cells (control) and its corresponding (drug-resistant R) cells from the same cell type. (a'-f'). The colored images are PWS images; a 2D map of L_{sd} where images show the representative mean intracellular disorder strength between control and corresponding drug-resistant prostate cells.

To test our hypothesis, we measured the average structural disorder strength values for the docetaxel treated DU-145, C4-2, and PC-3 cells, and compared with their corresponding eight months age-matched non-drug treated cell (i.e., drug-sensitive), obtained as described above. The results are shown in Fig.4.3 and Fig 4.4.

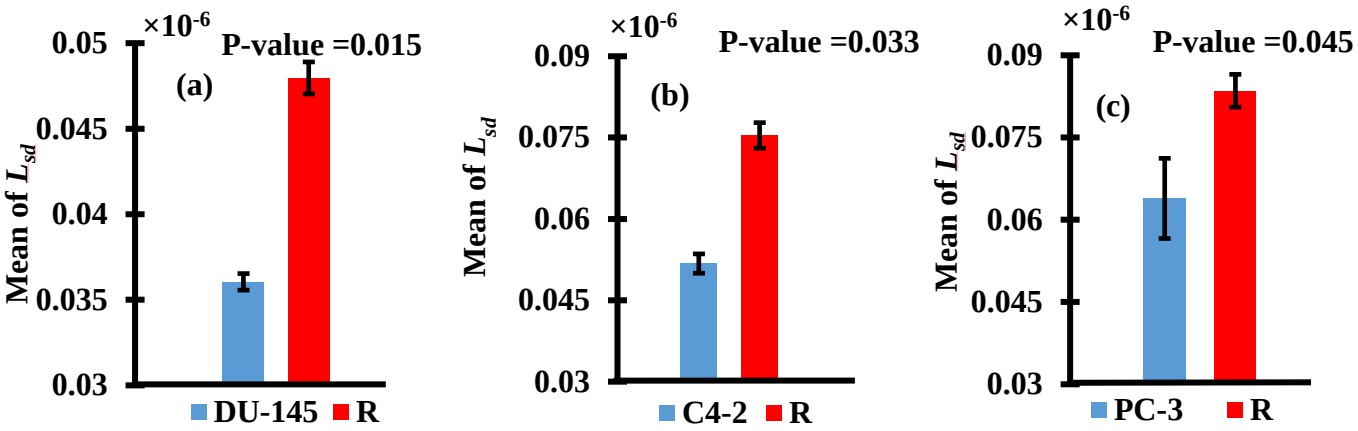

Figure 4.4: Bar plots for mean intracellular disorder strength value L_{sd} calculated for the three human prostate cancer cell lines: (a) DU-145, (b) C4-2, and (c) PC-3 (control) and the L_{sd} values of these cancer cells treated with docetaxel for about 8 months. Surviving cells are called drug-resistant cells, denoted as R. It can be seen that each drug-resistant cell type has higher L_{sd} than its corresponding control (aged cancer cells) type. The percentage increase of disorder strengths in the drug-resistance cells, relative to their corresponding non-drug treated DU-145, C4-2 and PC-3 cells are 34%, 45% and 30%, respectively.

As can be seen in figure 4.4, the disorder strength of the drug-resistant cells is higher than their corresponding age - matched normal cancer (control) cells. A p-value < 0.05 was obtained in each case, which suggests significantly elevated structural disorder in the drug-resistant cells induced with eight-month docetaxel dose, as compared with the untreated cells. This result also shows that a larger variation in the L_{sd} values were noted for the drug-resisted cells compared to their untreated counterparts. As pointed out before, it was anticipated that drug-resistant cells would show measurable structural changes associated with the aggressive behavior that prostate

cancer cells would have acquired after eight months of docetaxel chemotherapy *in vitro*, we indeed saw an increased disorder strength in the drug-resistant cells. Additionally, we were able to quantify such changes occurring in the cells in terms of the L_{sd} values, which provided a measure of the degree of aggressiveness in the cells.

These results not only show that the cancer cells underwent changes in their nano-architecture by virtue of prolonged exposure to the chemotherapy drug, but also show the potential use and quantitative capability of the disorder strength metric L_{sd}, as a useful biomarker by which to assess aggressiveness level acquired by the prostate cancer cells in chemotherapeutic treatment process.

4.5 Conclusion

In summary, we have applied partial wave spectroscopy (PWS) technique, to analyze structural disorder, in terms of 'disorder strength (L_{sd})' of the cells, in the selected stages of prostate cancer cell lines, namely C4-2, DU-145, and PC-3. These cancer cells were selected because they represent known levels or stages of tumorigenicity/aggressiveness (metastatic potential) of the prostate cancer cells, suggesting the clinical utility of measuring disorder strength of these cells. Subsequently, we also analyzed the effect of prolonged exposure to chemotherapy drug, docetaxel, on these cancer cells. In particular, we measured the changes in the disorder strength level in the cells which developed resistance towards the docetaxel drug upon an eight-month treatment (dose amount varying from 1 - 30 nM) compared to their age - matched untreated cancer cells (control). The first result showed that L_{sd} values for C4-2, DU-145, and PC-3 cell lines increases with the increasing order of metastatic potential (aggressiveness/tumorigenicity) which is DU-145 < C4-2 < PC-3. This result suggested that L_{sd} is directly correlated with the metastatic potential of these prostate cancer cell lines, and it can be potentially an efficient metric

to measure the aggressiveness of the prostate cancer cells. Subsequently, in the treatment with docetaxel drug, it was found that L_{sd} values (i.e., disorder strength) are significantly higher for the drug-resistant cells in comparison to their untreated counterparts, indicating higher aggressiveness in the drug resistant cells.

It should be noted that the disorder strength, L_{sd}, quantifies the intracellular structural changes, by measuring refractive index fluctuations inside the cells, which in turn arises as a result of mass density fluctuation inside the cells. In that context, the present results suggest that distinct structural changes have happened in the nano-architecture of control and drug-resistant cancer cells and that these changes presented as mass-density fluctuation increases in chemo-drug-surviving cells when the drug was introduced and applied for a long time. It should be worth pointing out here that cells behave differently in the case of drug resistance, including, for example, drug inactivation, alteration of drug targets, DNA damage repair, cell death inhibition, epithelial-mesenchymal transition and metastasis, cancer cell heterogeneity, etc.[63,71–75] By gene mutations, surviving cells increase their aggressive behavior and, correspondingly, their structural disorder owing to random growth, which, in turn, results in more drug resistance and higher L_{sd} values. The increase in the structural disorder in drug-resistant cancer cells can be measured by L_{sd} parameter, as demonstrated in the present chapter thus suggesting its utility as a potential biomarker with which to assess the efficacy of docetaxel.

These experimental results provided new insights into chemotherapy drug-resistant cells and the associated increase in their structural disorder, as explained in this work. The origin of these apparent pathologically related structural changes and their correlations with the specific molecular changes, as well as their relationship to drug resistance, are important matters to be explored in further studies.

5 Inverse Participation Ratio (IPR) Technique: Light Localization Properties of Biological Cells Via Confocal Imaging

The major part of this chapter has been taken from our below publications:

Optics Express 15428, Vol. 25, No. 13, 26 Jun 2017, and
Journal of Biophotonics. https://doi.org/10.1002/jbio.201700257, Jan. 2018

5.1 Introduction

In the previous two chapters (3 and 4), it was shown that the nanoscale structural disorder strength of the three-biological cancerous cell line models could be measured using mesoscopic light transport theory analysis of the one-dimensional backscattering spectra by these cells lines captured by the PWS system. To further investigate the structural disorder properties of the same cell lines, and support our previous results with PWS system, we introduce in this chapter a novel photonic technique, namely inverse participation ratio (*IPR*) technique. It is based on the analysis of the structural changes of the same biological cells by quantifying the effective structural disorder strength at the sub-micron scales with the help of the confocal imaging.

This dual approach, PWS, and IPR, would help us to understand the potential of the structural disorder analysis in the detection of cancer, and comprehensive understanding of structural changes in progressive carcinogenesis. This chapter discusses in detail about the formalism of the inverse participation ratio (*IPR*) technique. First, we will briefly introduce the working principles of the confocal microscopy, and subsequently, we describe the background, theoretical framework of *IPR* technique and the steps for determining the effective structural disorder using the averaged *IPR* values. In the following chapter, we apply the *IPR* technique for

cancer detection for breast, brain, and prostate cancer cell line models and compare the two techniques, *IPR* and PWS, in measuring the disorder strength.

5.2 Confocal Laser Scanning Microscopy (CLSM)

5.2.1 The Optical Principle of CLSM

Wide-field (non-confocal) fluorescence microscopy is a powerful technique that helps in studying and monitoring biological processes in fixed and living cells. The idea behind the fluorescence processes is very basic where electrons in a fluorescent molecule in a ground energy state (S_0) are excited by incident energy (incident photons) and make a transition to a higher electronic state (S_1or S_2 in diagram 5.1). This process is followed by the electrons dropping back to a lower energy state and emitting photons (fluorescence) with lower energy. Therefore, the working principle of the fluorescence microscopy is based on the optical excitation of the fluorescent specimen with a specific wavelength, which is absorbed by the fluorophores, causing them to emit light with longer wavelengths.

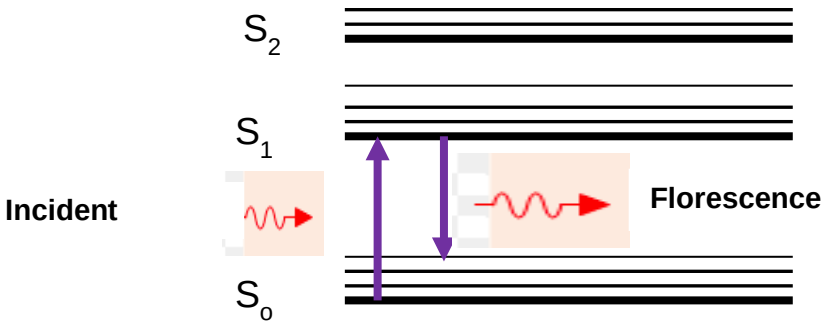

Figure 5.1: Jablonksi diagram of florescence pathway. In which electrons in a molecule make a transition between the eigenstates and release photons upon the interaction with light.

Further development of fluorescence microscopy led to the birth of the confocal scanning microscopy (CFM) by Marvin Minsky in the 1950s. Therefore, confocal scanning microscopy is an updated version of the wide-field fluorescence microscopy with superior imaging capability due to the contrast and resolution improvement. Figure 5.2 shows a schematic representation of the optical paths of confocal laser scanning microscopy.

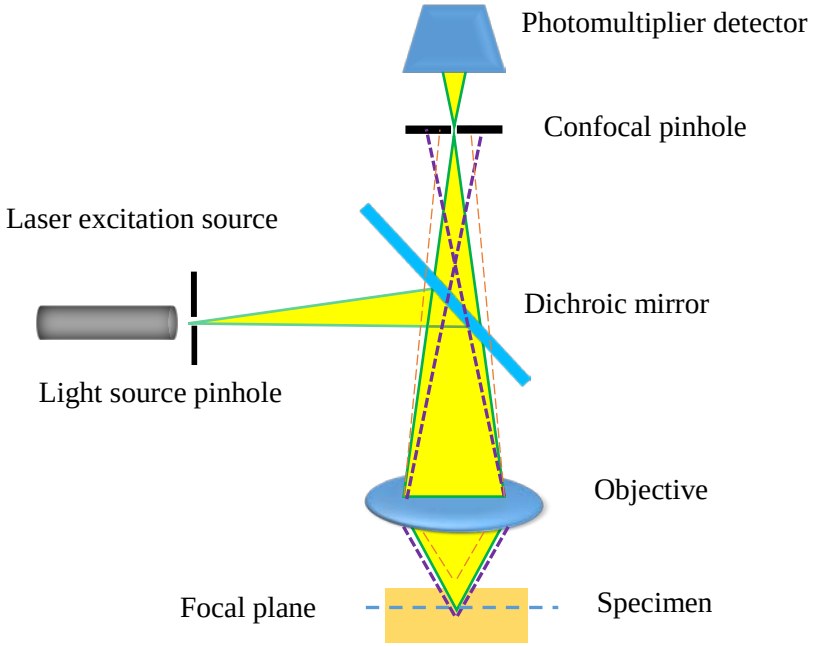

Figure 5.2: The optical paths of the excitation and fluorescent light. A pinhole is placed in a plane conjugate to the focal (objective) plane (in front of the detector). The pinhole rejects out of focus fluorescent light (red and purple light) and allows the light coming from the in-focus plane (green light) to reach the detector.

Two principal ideas are added to the confocal microscopy and made it possible to overcome conventional microscopy multiple scattering problems that cause low contrast images. First, the so-called point-by-point illumination of the specimen to control, while minimize the amount of fluorescence that out of focus and hence avoid light that scattered from different regions than the point of focus in the sample (focal plane). This mode of scanning can be achieved either by placing a pinhole in front of the excitation light or by introducing a narrow

beam of laser with the help of fiber optic. Second, a pinhole in front of the detector stops out of focus light, that comes from a plane above and below the objective focal plane, from reaching the detector.

5.2.2 Confocal Microscope Design

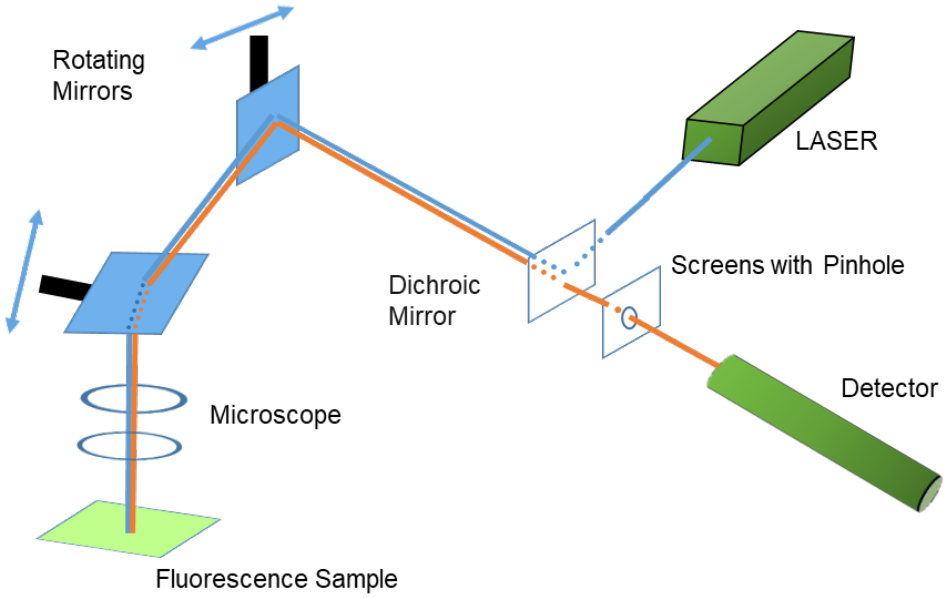

Figure 5.3: The one of the illumination methods in confocal microscopy based on the use of two rotating mirrors. The laser beam deflected by the mirrors toward the sample to scan the sample in a raster pattern. The light emitted from the fluorescence sample is deflected by the rotating mirrors in the revers path and collected by the detector.

In laser scanning confocal microscopy, the laser beam scans the sample with the help of two galvanometric mirrors (rotating mirrors) with the optical parts stationary. The pair of mirrors scans the laser light in a raster pattern in the x and y directions across the sample instead of moving the sample in front the beam. The advantage of the beam scanning mirrors is that the image reconstruction of the sample takes only a few milliseconds whereas the latter case it takes several minutes to reconstruct the sample image. Figure 5.3 shows how the mirrors used to

direct the excitation beam and the fluorescence light from the sample. The excitation light (blue line) is directed by a dichroic mirror (beam splitter) towards the galvanometric mirrors which deflect the angle of the laser to illuminate (scanning) the sample point by point. The laser excites the dye in the specimen and the emitted light (orange light) from the excited spot gets deflected by the mirrors to take a reverse optical path (de-scanning) with respect to the incident laser beam. The fluorescent light then passes through the dichroic mirror and arrives at the pinhole in front the detector and finally to the detector (photomultiplier tube).

5.2.3 Optical Sectioning

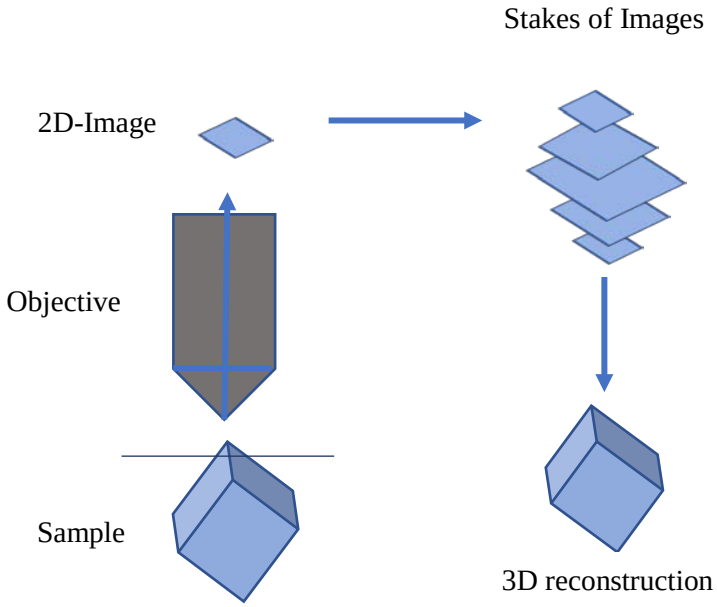

Figure 5.4: Shows a 3D reconstruction of an object from a series of 2D images. The sample steps with respect to the objective to acquire a series of 2D images at different focal plane from the top to the bottom of the object (different optical sections). The 2D image in the middle of the stacks cover the maximum area of the object. The stacks of images used by the computer to generate a 3D reconstruction of the object.

Among the advantages that laser scanning confocal microscopy provides the optical sectioning. To build a 3D image of a specimen, sequential 2D slices (optical section) are captured through a sample at different heights (focal plans) across the sample. Then, series of the optical sections

are stacked together into a 3D image called a z-stack that is processed with the computer to give a 3D structure that can be visualized from different angles. Therefore, the movement of the sample stage away from the objective or up toward the objective allows the capture of multiple optical sections each represented by a 2D plane image. As it shows in the Figure,5.4, recording the image information at different focal planes allows the 3D-reconstructing of the whole sample volume.

5.3 Light Diffraction and Spatial Resolution

The resolution of the optical microscopy is limited by the diffraction of light. In general, when light passes through obstacles (slits, gratings), it diffracts or bends from the edges of the obstacles and forms a diffraction pattern due to the interference of the light waves. The inherent resolution of confocal microscopy can be explained by the image formation process by a point source. On the microscopic scale, a specimen can be seen as a collection of slits with different widths, and when a point source (parallel beam) illuminates the specimen, the light diffracted and spread out and finally collected by an objective. The diffraction angles of light depend on the size of the slits (the size of the specimen details) and the narrower the slit (finer the size of a detail) the greater the angle of diffraction. Therefore, to collect the finer details of a specimen, we need an objective with a large angular numerical aperture to collect light from large diffracted angles. Moreover, the diffraction angle of light depends on the wavelength of light used, where shorter wavelengths diffracted with a small angle compared to long wavelengths.

The resolution of an optical imaging system can be defined as the ability of the system to distinguish between two closely spaced points on the image plane. When a point source illuminates a specimen, the image created for an object is not a fine bright dot, but a diffraction pattern. This pattern consists of the central bright spot, known as Airy disk, surrounded by a

series of diffraction rings. The maximum resolution that can be acquired by a microscopic system is set by the size of the Airy disk. According to Rayleigh criterion, the minimum distance between two Airy discs must be their radius in order for them to be resolved. The diffraction limited resolution theory relates the average imaging wavelength (λ), the numerical aperture ($NA = n\sin\theta$)) of the objective lens and Airy disk size (A) through Eq.1.[76]

$$A = 0.61\lambda/(NA) \quad \textbf{(1)}$$

Researchers have developed different techniques to exceed the diffraction limit resolution of the optical microscopy; however, one of these techniques is confocal microscopy. The resolution of the commercially available confocal microscopy is 30% higher than the conventional optical microscopy [77] and it given by [78]

$$A = 0.37\lambda/(NA) \quad \textbf{(2)}$$

5.4 Inverse Participation Ratio (IPR) Technique

Bloch's theory describes the eigenfunctions and eigenvalues for an electron in a solid system with a periodic potential (energy sites) $v(r)$, where $v(r) = v(r + r')$, r' is the period in the lattice. The solution of the Schrodinger equation of such system gives wave functions of the electron represented by plane waves with probability amplitudes extended over the entire system (lattice). However, in a system with a random potential, Bloch's theory fails. P.W. Anderson was the first to describe an electron moving in a random lattice and he predicted the localization of electrons eigenfunctions in a highly disorder system.[79]

The Anderson model is used to study the available energies states (wavefunctions) for an electron instead of solving Schrodinger equation, because of the difficulty due to the randomness in the system's potential energies. The model is based on the tight binding model, in which, the system is represented by a discrete lattice sites and the electron is subjected to the energy site (potential energy) associated with each lattice site. Moreover, for simplicity, the electron interaction (kinetic energy) is restricted to the nearest-neighbor sites. In other words, the electron has kinetic energy that allows it to hop from one site to another (nearest-neighbor sites only). It is worth noting that Anderson localization is a wave phenomenon in general that can occur for any type of classical and quantum wave, light, acoustic and electron wave, when propagating in disorder medium (disorder potential). One method to distinguish localized eigenfunctions of a system and hence characterize the system disorder properties is to calculate the inverse participation ratio (*IPR*), which averages the fourth power of the eigenfunctions of a system.

Earlier, a technique was proposed that quantifies the effective degree of structural disorder in heterogeneous biological samples using a single parameter via inverse participation ratio (*IPR*) analysis of the light wave eigenfunctions of these systems.[80] This approach utilizes the fact that in a weakly disordered system, the degree of structural disorder (L_{sd}), which relates to the mass density (or, refractive index) fluctuation inside the sample, is linearly proportional to the *IPR* value for a system.[81,82] In this study,[83] the transmission electron microscopy (TEM) imaging technique was used to generate the 'optical lattices' (analogy of potential energy or simply potential sites) from the cells; subsequently, light localization properties were analyzed for the control and cancerous cells. The study showed highly promising results in quantifying and differentiating nano-scale level structural disorders in biological samples.

Although this technique is highly promising, it requires the sample preparation and imaging efforts of electron microscopy. With that view in mind, we demonstrate here performing similar studies with optical microscopy as an alternative to the TEM imaging.

In particular, we performed the light localization analysis of biological cells using confocal fluorescence microscopy, which is one of the most widely used optical imaging techniques in life science and biomedical research. The additional advantage of using confocal fluorescence microscopy is that the structural disorder analysis can be performed for fluorescently labeled selective molecules or organelles inside the cells. For example, in our investigation work in the next chapter, we selectively perform the structural disorder analysis of nuclear DNA using DAPI staining.

5.4.1 Calculation Method of the Structural Disorder: IPR Technique

The IPR technique involves the use of the fluorescence intensity fluctuation data from confocal micrographs to construct a disordered 'optical lattice' systems. Numerically determining of the eigenfunctions and eigenvalues of the optical lattice system using the Anderson tight-binding model (TBM) Hamiltonian in closed boundary conditions follow this. Subsequently, a statistical analysis of the eigenfunctions leads to the calculation of an average *IPR* value for the disordered lattice system. The average *IPR* value of a system, i.e. $\langle IPR \rangle$ is proportional to physical parameters, RI fluctuations or rms value, dn and its correlation length lc, of a system.

5.4.2 Pixel Intensity in Confocal Microscopy Imaging in 2D

In confocal imaging, the amount of fluorescence intensity emitted from a 'point' (excitation center on the focal plane) inside the sample is emitted out by the fluorescing molecules inside a finite volume, 'voxel', around that excitation center. The excitation volume depends on the laser beam intensity profile being used for the excitation. For a typical Gaussian-shaped laser beam,

the intensity profile around the excitation center $r_c\,(x_c, y_c, z_c)$ is given as, $I(r,r_c) \propto exp[-2\{(x-x_c)^2 + (y-y_c)^2\}/w_{xy} - (z-z_c)^2/w_z]$, where w_{xy} is the lateral width and w_z is the axial width, which together determines the volume covered around the excitation center. Under normal imaging conditions, i.e., uniform incident intensity across the sample plane, no fluorescence saturation, and photo-bleaching, the amount of fluorescence intensity emitted out from the voxel volume can be considered as proportional to the mass density of the fluorescing molecules inside that volume, that is $I(r)_{out} \propto dV_{voxel}(\rho)$ where ρ is the mass density. [82,84,85]

Therefore, under normal imaging conditions, the intensity detected at the image plane, i.e., the pixel values, is a measure of the mass density of the dye molecules inside the small volume in the sample plane, which in turn is stoichiometrically proportional to the mass density of the target molecules inside that volume. Therefore, the detected confocal image intensity (I_{CFM}) can be written as,

$$I_{CFM}(r) \propto dV_{voxel}(\rho) \qquad \textbf{(3)}$$

5.5 Relation between Mass Density and Refractive Index of a Biological Sample: Optical Lattice Construction and Its Physical Significance

The pixel intensity values in a confocal fluorescence image are used to construct a refractive index matrix termed an ‘optical lattice’. It is known that the variation in fluorescence intensity recorded in the confocal image plane depicts the variation in the mass density of targeted molecules inside the cell. Additionally, it is also well known that local refractive index inside a

biological sample is proportional to its local mass density. [86,87] Therefore, considering the mass density at any point *r* inside the cell of form

$$\rho_{cell}(r) = \langle \rho \rangle_{cell} + \beta d\rho_{cell}(r) \quad \textbf{(4)}$$

Where $\langle \rho \rangle_{cell}$ the average mass density of the cell, $d\rho_{cell}(r)$ represents the fluctuation in the mass density at the position *r*, and β is a proportionality constant. The refractive index (*RI*) can also be written as, $n(r) = n_0 + dn(r) \propto (\langle \rho \rangle_{cell} + \beta d\rho_{cell}(r))$. Where n_0 is the average refractive index of the cell and $dn(r)$ represents the spatial refractive index fluctuations. In general, the average refractive index of biological cells is ~1.38 and the position dependent fluctuation ranges up to ~ 0.02. In the case of fluorescence imaging, since the fluorescent intensity is proportional to the mass density of the target molecules, the contrast of the pixel intensity values in the confocal micrograph can be attributed to the spatial variation in the mass density of the target molecules. Consequently, in turn, the contrast of the pixel intensity values can be correlated to the spatial refractive index fluctuations inside the sample. We defined the term $\varepsilon(x, y) = \frac{dn(x, y)}{n_0}$ as onsite 'optical potential' corresponding to pixel position (x, y) on the 2D image plane.

To express mathematically,

$$\varepsilon(x, y) = \frac{dn(x, y)}{n_0} \propto \frac{d\ I_{CFM}(x, y)}{< I_{CFM}(x, y) >} \quad \textbf{(5)}$$

Thus, the onsite 'optical potential' values, $\varepsilon(x, y)$ are obtained from the corresponding pixel intensity values in the confocal image. As illustrated in Fig.5.5, from a confocal image, created by point-to-point scanning on a horizontal plane inside the sample (Figs.5.5 (a) and 5.5(b)), the

pixel intensity values at each point (x, y), $I_{CFM}(x, y)$ is noted down. Then, $dI_{CFM}(x, y)$, $< I_{CFM}(x, y) >$ is calculated for each of the pixels in the image. Subsequently, using Eq. 5, the $\varepsilon(x, y)$ values are calculated for all the pixel points of the confocal image.

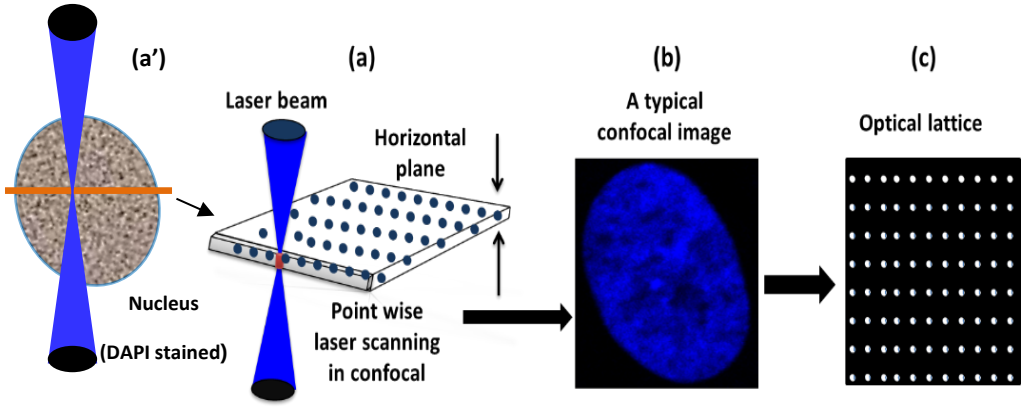

Figure 5.5: Construction of a disordered optical lattice from confocal imaging (schematic pictures): (a') Imaging of a sample with a laser beam (a) Voxel-wise scanning on xy- plane (z=constant) to construct a confocal 2D plane image of a DAPI stained cell nucleus. (b) A typical confocal image- 2D micrograph. (c) A sample disordered optical lattice: each dot in the optical lattice is determined from the pixel confocal fluorescence image as shown in (b).

This results in a matrix, of the size of the confocal image, with the $\varepsilon(x, y)$ values known for each of its points as represented in Fig.5.5(c). As described in the next chapter in detail, we used DAPI fluorescence staining to target DNA molecules inside the nucleus of the cells. Therefore, the fluorescence intensity contrast observed in the confocal images represents the refractive index fluctuation pattern of the DNA molecules inside the nucleus of the cells. Consequently, an optical lattice obtained in such a way depicts a disordered optical system representing intranuclear spatial DNA distribution.

Since, in this process, we obtain a matrix, of the dimension of the confocal image, for which the 'optical potential' values, i.e., $\varepsilon(x, y)$ values, are known for each of its points, this

matrix is simply termed as 'optical lattice'. It should be noted that the $\varepsilon(x, y)$ values represent the strength of refractive index fluctuations of the target molecules at those spatial positions (x, y) on a 2D plane inside the cell. Thus, essentially, this optical lattice is a representative of spatial refractive index fluctuation pattern of the targeted molecules inside the sample.

5.6 Tight-Binding Model and IPR Calculations

In the next step, an Anderson tight-binding model (TBM) Hamiltonian is constructed for the optical lattice systems generated from the confocal micrographs. To quantify the structural disorder properties from the CFM images, we need to calculate the IPR of the system. The calculation of IPR of the system required the determination of the eigenfunctions and eigenvalues of the system. To do so, we carry out numerical calculations of the Anderson disorder tight-binding model (TBM) Hamiltonian[88] which is constructed from the optical lattice system generated from the confocal micrographs, such a Hamiltonian can be written as follows:

$$H = \sum_i \varepsilon_i \mid i >< j \mid + t \sum_{<ij>} \mid i >< j \mid + \mid j >< i \mid , \qquad \textbf{(6)}$$

Here, ε_i (= dn_i/n_0) represents the optical potential of the i^{th} site and that $\mid i >$ represents the state of a photon at any arbitrary lattice site i and t is the inter-lattice site hopping energy. For any disorder system, the diagonal matrix elements of the Hamiltonian are the site energies ε_i and the off-diagonal elements are values of the hopping parameter t, which is taken to be constant and limited to nearest neighbors (i and j) and otherwise are equal to zero.

5.7 Ensemble Averaged IPR Value and the Degree of Structural Disorder Calculation in Terms of IPR

Strictly speaking, *IPR* measures the localization of an eigenfunction $\Psi(r)$ of a system in D-dimensions and defined as. [89]

$$IPR = \int dr \left|\Psi(r)\right|^{2D} \tag{7}$$

From the Hamiltonian in E.q 5, the E_i (eigenfunctions) were determined and we analyzed the localization properties of a system by measuring the average value of *IPR* , <*IPR*>, over the *N* eigenfunctions, calculated for 2D lattice L×L calculated by. [81]

$$< IPR(L) >_{Pixel} = \frac{1}{N} \sum_{i=1}^{N} \int_0^L \int_0^L E_i^4(x, y) dxdy \tag{8}$$

Where E_i is the i^{th} Eigen function of the lattice Hamiltonian determined for a small area $L \times L$ inside the sample, and N represents the total number of eigenfunctions in the sample area $L \times L$. For a discrete lattice system, N is determined by the total number of lattice points in the sample area [i.e., $N = N_p^2$, where $N_p = L/a$ and dx = *dy* = *a* (lattice constant)]. < > represents ensemble averaging, i.e., averaging over several different samples of size $L \times L$. For 2D system, the *IPR* values are measured in the unit of inverse area.

To calculate the *IPR* value of a sample at a length scale *L*, the process first involves dividing the whole sample (micrograph) into small square areas $L \times L$. For example, a *100×100-pixel* micrograph can be divided into *25×25 (=625)* square areas for *L* corresponding to *4* pixels. For every square area, with the known optical potential at each lattice site, i.e., pixel points, inside it, a Hamiltonian matrix is constructed using Eq. 5. Subsequently, eigenfunctions are

determined from this Hamiltonian matrix. After all the eigenfunctions for the small closed lattice system (of length scale L) are known, the *IPR* value for this small area within the sample is calculated using Eq. 8. This *IPR* value constitutes one-pixel value in the 2D *IPR* plot. Thus, a distribution of *IPR* values for the whole sample, corresponding to the particular length scale L is obtained. Finally, an ensemble averaged *IPR* value, $\langle IPR(L) \rangle$, is obtained for the whole sample by taking mean of all the *IPR* values determined at the length scale L.

Further averaging of the *IPR* values is done for a number of cells of a particular cell type, and are compared with the average *IPR* values of other cell types. Similar analysis and comparison are done for different length scales as well. Two systems with different degree of structural disorders result in different $\langle IPR(L) \rangle$ values.[80] The $\langle IPR(L) \rangle$ value corresponding to a sample area $L \times L$ is a measure of the strength of light localization inside the sample in that area. The strength of light localization, or the *IPR* value, in a closed area measures the effective structural disorder of the sample, which in turn is a function of the magnitude and spatial distribution of the refractive index fluctuations inside the area.

5.8 Significance of IPR Value

Typically, disorder inside a refractive index system is characterized by two parameters, namely the refractive index fluctuations dn and its spatial correlation length l_c. These parameters come with different functional forms, or a combination of functional forms, depending on the complexity of the heterogeneous sample. For example, for a Gaussian color noise disorder, defined by $\langle dn(x)dn(x') \rangle = \langle dn^2 \rangle exp(-|x-x'|/l_c)$, can be characterized by the $\langle dn^2 \rangle$ (the strength of fluctuation) and its spatial correlation decaay length l_c. Similarly disorder of other functional form or a combination of them are characterized by effective dn and l_c (if they are known).

Being based on eigenfunctions of the system, the IPR approach further reduces the complexity by measuring the degree of disorder (i.e., disorder strength) in one parameter, namely the <IPR> value (note that the eigenfunctions of the system contains all the disorder information in them). For a simpler case of 2D Gaussian color noise disorder system, it has been shown that $\langle IPR \rangle \sim dn \times l_c$.[90] Thus, the two parameters, dn (= $\langle dn^2 \rangle^{1/2}$: standard deviation) and l_c, are combined into a single one, i.e., $\langle IPR \rangle$ value, which is also termed as 'disorder strength', because it provides a measure of the RI fluctuations (magnitude as well as correlation length) inside the system. Consequently, for 2D systems, the ensemble average of all the *IPR* values can be expressed as shown in Eq. 8

$$\langle IPR \rangle = \langle IPR \rangle_{Sample} \equiv Disorder\ \ Strength.$$

5.9 Summary of the Technique

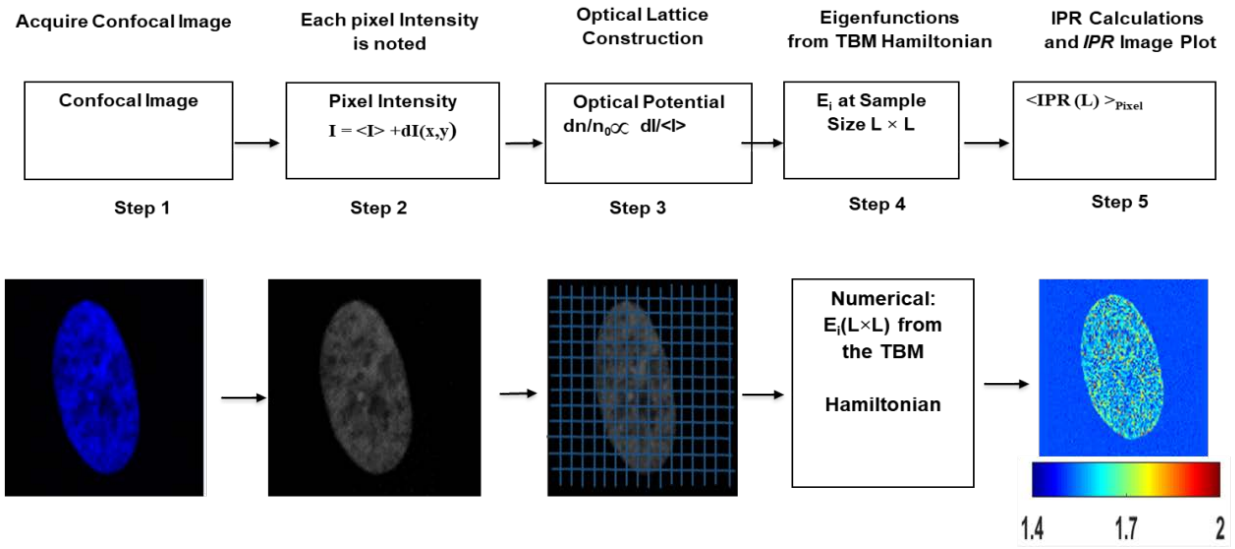

Figure 5.6: Schematic flowchart for IPR calculation from confocal images.

We methodically describe the steps involved in calculating the IPR values using confocal fluorescence micrographs. Fig 5.6 shows a schematic flow chart of IPR calculations. The process

mainly involves five major steps, starting from acquiring the confocal images to calculating the average *IPR* value, $\langle IPR \rangle$, as follows:

- **Step-1:** The desired confocal images/micrographs are acquired from the cells.
- **Step-2:** Using the pixel intensity values of each micrograph, a pixel intensity matrix is obtained: $I(x,y) = \langle I \rangle + dI(x,y)$.
- **Step-3:** From the pixel matrix, an optical refractive index lattice/matrix is obtained by considering one-to-one correspondence between micrographic pixel intensities and the refractive index defined as $dn_i/n_0 \propto dI_i/\langle I \rangle$, where dn_i is the refractive index fluctuation at i^{th} lattice points, n_0 is the average refractive index of the cell, and dI_i is the i^{th} pixel in the confocal micrograph (i.e., $dI(x,y)$). Then, for every point in the optical lattice, an "*optical potential*" is defined as $\varepsilon_i = dn_i / n_0$. In essence, this procedure replaces the confocal pixel intensity matrix with a refractive index/optical potential matrix, or, more simply, an "optical lattice" system of refractive index distribution.
- **Step-4**: In this 2-dimensional optical lattice, we choose a sample size $L \times L$, i.e., $N_p \times N_p$ optical lattice points, where $N_p = L/a$, with a as the lattice unit. On this lattice size, a tight binding Hamiltonian is constructed with $\varepsilon_i\ (= dn_i/n)$ as the onsite potential using Eq. 5.
- **Step-5:** We calculate the eigenfunctions, $E_i s$, of the Hamiltonian, where E_i is the i^{th} eigenfunction of the Hamiltonian. From the $E_i s$, we calculate the average *IPR*, $\langle IPR(L) \rangle_{Pixel}$, using the Eq. 8, which constitutes the one-pixel value of the IPR image. Thus, in this way we obtain an IPR distribution inside sample corresponding to the length scale L, i.e. in the sample area $L \times L$.
- ***IPR image***: The $\langle IPR(L) \rangle_{Pixel}$ image is constructed from the confocal image by systematically determining the average *IPR* value for the area covered by $L \times L$ pixels in

the confocal micrograph or the optical lattice size which is equal to $N_p \times N_p$. That is, for a confocal micrograph of pixel dimension $L_{max} \times L_{max}$, we get $\langle IPR(L) \rangle_{Pixel}$ image of dimension $L_{max}/L \times L_{max}/L$.

- $\langle \boldsymbol{IPR(L)} \rangle = \langle \langle \boldsymbol{IPR(L)} \rangle_{\boldsymbol{Pixel}} \rangle_{ensemble}$: Once the distribution of $\langle IPR(L) \rangle_{Pixel}$ values on a micrograph are known, they are averaged to get a mean *IPR* value of a cell, followed by averaging over several micrographs of a cell and, finally, for several cells of the same category. The $\langle IPR(L) \rangle$ values are obtained for different length scales L.

6 Quantification of Photonic Localization Properties of Targeted Molecular Specific Nuclear Mass Density Variations: Application in Cancer Detection

The major part of this chapter has been taken from our below publications:

Optics Express 15428, Vol. 25, No. 13, 26 Jun 201, and
Journal of Biophotonics. https://doi.org/10.1002/jbio.201700257, Jan. 2018

6.1 Introduction

In the previous Chapter, we have described and developed the formalism for characterization of structural disorder by inverse participation technique via confocal microscopy. In this chapter, we will apply the inverse participation technique for differentiating normal and cancer cells, as well as characterization of the stage of the cancer. Analyzing structural disorder of weakly disordered optical media has many applications, in particular determining the physical properties of the samples such as refractive index variation. Some typical examples of such media include polymers, thin dielectric films, biological media cells/tissues, etc. The characterization of these disordered media becomes more complicated if the system has spatial heterogeneity involving many kinds of spatial correlation decay length scales within the sample, for example as in biological cells. [28,91] Recently, there has been a significant interest in quantifying structural disorder of cells, by analyzing their light transport and localization properties [27,92] These investigations have shown that the analyses of light localization properties of cells can be a useful tool to examine the progress of cancer as well as to characterize the intracellular tumorigenicity levels. From physics point of view, cells are dielectric/refractive index media with typical length scale ~2-10 μm, which corresponds to the mesoscopic length scale regime. Secondly, owing to the complex spatial arrangements of the basic building blocks of the cells, such as DNA, proteins, lipids, etc., inside the cells, the cells' refractive index media have

inherent heterogeneity. Thus, with very weak light scattering properties, cells are a perfect example of weakly disordered heterogeneous optical media. Therefore, in principle, the light transport and localization analyses of the cells can be a useful method to extract out information about the physical properties of the cells. In fact, such approach has been shown to have practical applications, for example in the detection of early carcinogenesis. [80] Consequently, these developments have opened new avenues for applications of "mesoscopic physics" based optical transport analysis [81,93] in understanding disease processes in the biological cells.

It should be noted that disorder analysis of optical disordered media via light localization has been widely studied in last few decades [94,95] For a closed boundary optical disordered media, the light is localized due to the multiple interference effects within the disordered samples. The phenomenon of light localization in the disordered media is quantified in terms of the IPR values [89,96]. In general, the localization effect is more strongly observed in 1D and 2D systems compared to 3D systems.[97] According to the scaling theory of localization, all optical eigenstates are localized in 1D-disordered systems, while 2D systems are marginally localized, and 3D systems have localized/delocalized states. [98] As a result, the disorder analysis is preferably performed for 1D or 2D systems. Additionally, the 2D images provide a better planar visualization of the light localization strength, in term of the structural disorder. Therefore, in the present work, we have conducted the structural disorder analysis with 2D confocal images. The choice of confocal fluorescence microscopy takes advantage of the mechanism of confocal imaging technique in constructing 2D images of the sample. The pixel intensity of a 2D confocal image obtained upon a systematic voxel-by-voxel scanning inside the sample on a horizontal thin layer of xy-plane, for a fixed z-axis. This scanning consequently represents the refractive index variation pattern of the target molecules inside the sample in the slice of the 2D plane. The

'optical lattice' matrix (i.e., the refractive index matrix) were generated using the pixel intensity values from the confocal images, and these optical lattices were used to compute the degree of structural disorder in the sample. For this, first an optical disorder potential array is generated, and then using the Anderson tight-binding model (TBM) Hamiltonian in the 2D potential matrix, the eigenfunctions were obtained by solving the Maxwell's light wave equation in a closed boundary condition. Finally, we quantify the structural disorder in the sample by calculating the average *IPR* values of all the eigenfunctions of the optical lattice system. Subsequently, an average *IPR* value, $<IPR>$, averaged over all the cells of particular type are calculated. Two types of biological cell samples with different mass density (or the refractive index) fluctuations distribution of the targeted molecules would result in optical lattice systems with different structural disorders. In the present work, we compare the average *IPR* values of cancerous cells and normal cells. Specifically, in this proof of the concept study, we analyzed normal and cancerous breast, brain, and prostate cell line models.

Since carcinogenesis is associated with spatial alteration/rearrangement in DNA/chromatin structure inside the nucleus, we focused on examining the degrees of structural disorder of the DNA molecules in the nuclei of these cells. In order to perform confocal imaging of the nuclei of these cells, they were dyed with DAPI, and from the confocal imaging of DAPI stained nuclei, we were able to differentiate the normal and cancer cell nuclei by quantifying sub-micron scale level ultra-structural alterations in the nuclei of these cells, using the IPR technique.

6.2 Methodology and Theoretical Background

In this section, we will briefly describe the quantification method of light localization properties of cellular media, evaluating the structural disorder L_{sd}, inside cells' nuclei, using confocal

imaging. The description systematically elaborates the methodology, starting from the construction of the optical lattice (using pixel intensities in confocal micrograph) to the calculation of the *IPR* values.

6.2.1 Construction of Optical Refractive Index Lattice for Targeted Molecular Mass Density Using Confocal Imaging

In confocal fluorescence microscopy, any particular molecule can be selectively emphasized (targeted) for imaging using specific fluorescent dyes. For example, DNA molecules inside the nucleus are targeted by staining them with DAPI fluorescent dyes, which stoichiometrically binds with the accessible DNA molecules. It has been shown that the RI, $n(r)$, inside a cell is linearly proportional to local mass density, $\rho_{cell}(r)$, of macromolecules, e.g., DNA, RNA, proteins, etc., $n(r) = n_0 + dn(r) = \langle\rho\rangle_{cell} + kd\rho_{cell}(r)$. Where n_0 is the average RI, $dn(r)$ and $d\rho_{cell}(r)$ represents RI and mass density fluctuations at position r, respectively; k is the proportionality constant. Importantly, in quantitative image analysis, the pixel intensity of confocal fluorescence micrograph is considered as directly proportional to the mass density of the targeted molecules at the voxel point. [76,85] Therefore, if fluctuation in the RI is represented by $dn(r)/n_0$, then $dn(r)/n_0 \propto dI(r)_{CFM}/\langle I\rangle_{CFM}$, where $\langle I\rangle_{CFM}$ and $dI(r)_{CFM}$ represent the average confocal intensity and the intensity fluctuation at position r in the confocal image. [99]

In the present work, we used DAPI fluorescent dyes to stain the DNA molecules of different breast, brain, and prostate cells, then imaged them with confocal fluorescence microscopy. As described above, using the pixel intensity values in the confocal fluorescence micrograph, a 2D refractive index map, corresponding to the DNA distribution in the sample is constructed.

6.2.2 Tight-Binding Model to Determine the Eigenfunctions of the Optical/Refractive Index Lattice/Matrix and IPR Calculations

We have described this step in the earlier chapter. However, for the completeness of this Chapter, we will briefly mention the formalism. For the optical lattice, constructed using the confocal image, the disordered tight binding model (TBM) Hamiltonian is determined. The Maxwell light wave equation is solved for the disordered optical lattice system under closed boundary conditions. Considering that ε_i (= dn_i/n_0) represents the onsite optical potential at the i^{th} site and that $|i>$ represents the state of a photon at any arbitrary lattice site, the Hamiltonian for the entire lattice system can be obtained using the TBM as shown in Eq.1

$$H = \sum_i \varepsilon_i \, | i >< j | + t \sum_{<ij>} | i >< j | + | j >< i | , \qquad \textbf{(1)}$$

Where t is the inter-lattice site hopping strength, which is restricted to only the nearest neighbors. Subsequently, the eigenvalues and eigenfunctions of the system are determined from the Hamiltonian. From the above Hamiltonian, the average value of *IPR*, $<IPR>$, is calculated as shown in Eq.2 [100]

$$< IPR(L) >_{Pixel} = \frac{1}{N} \sum_{i=1}^{N} \int_0^L \int_0^L E_i^4(x, y) dx dy \qquad \textbf{(2)}$$

Where E_i is the i^{th} eigenfunction of the lattice determined for a small area $L \times L$ inside the sample, and N represents the total number of eigenfunctions in the sample area $L \times L$. For a discrete lattice system, N is determined by the total number of lattice points in the sample area [i.e., $N = N_p^2$, where $N_p = L/a$ and $dx = dy = a$ (lattice constant)]. It should be noted that, the above described IPR analysis of the eigenfunctions of a lattice system has been widely studied

both for electronic and optical media, and is considered to be one of the most efficient method to analyze structural disorder of the corresponding lattice system.

Since biological systems are heterogeneous media, therefore, the degree of structural disorder in two different biological systems is compared through their $\langle IPR(L) \rangle$ (ensemble averaged) values by considering an effective Gaussian color noise refractive index fluctuating system with exponentially decaying spatial correlation statistics. It has been shown that $\langle IPR(L) \rangle$ value is proportional to the strength of the structural disorder L_{sd} of the sample in an effective Gaussian model. [27] Therefore, once the $\langle IPR(L) \rangle$ value for each closed sample area is known, the L_{sd} inside that closed area of $L \times L$ is characterized via a Gaussian color noise with exponentially decaying spatial correlation of the refractive index fluctuations. This type of Gaussian color noise is typically represented as $\langle dn(r)dn(r') \rangle = \langle dn^2 \rangle exp(-|r-r'|/l_c)$, where dn is the fluctuation in refractive index distribution and l_c is the spatial correlation decay length of the fluctuation. The choice of the Gaussian color noise model is based on the fact that theoretical framework for localization analysis is well established for Gaussian disorder model, for both white and color noise models. [81,93] For a Gaussian color noise refractive index fluctuation with short correlations decay length, it has been shown with extensive numerical simulations in 2D disordered system, that [27]

$$\left\langle IPR(L) \right\rangle \propto L_{sd} = \left\langle dn^2 \right\rangle^{1/2} \times l_c \qquad \textbf{(3)}$$

Therefore, a change in <IPR(L)> values, and thus the L_{sd} values, indicates a change in either the fluctuation strength of the refractive index or a rearrangement in its spatial distribution or the product of both the quantities, for a fixed sample length L, i.e., sample size L×L. For the simplicity of expressing the structural disorder in terms of IPR values, we are considering the

proportionality constant as 1; thus, expressing L_{sd} and the IPR as the same numerical number, i.e., L_{sd}(<IPR(L)>) =<IPR(L)>. A typical schematic of the steps involved in this study of comparing structural disorder in two samples using confocal fluorescence microscopy has been shown in Fig.6.1.

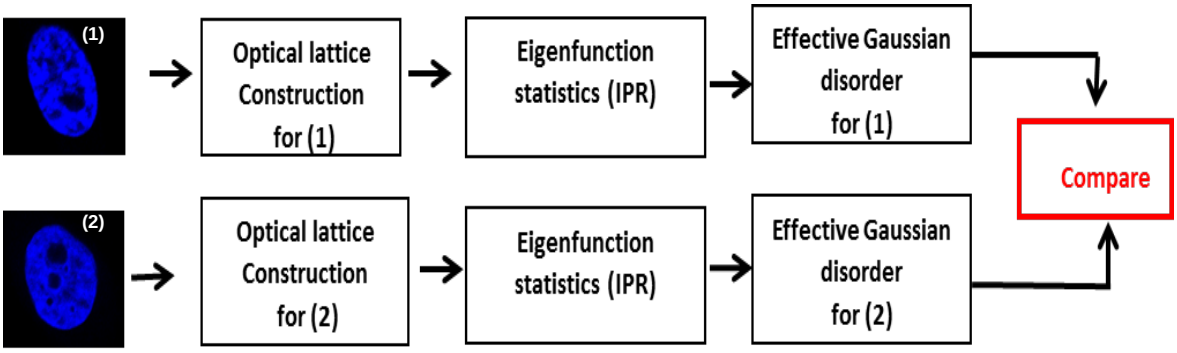

Figure 6.1: Schematic flowchart for comparing the structural disorder using confocal micrographs. (i) The confocal images of the nucleus of two samples were obtained. (ii) Optical lattices are constructed, and eigenvalues are obtained by solving the Anderson tight binding model optical Hamiltonian, (iii) The structural disorder of the samples are then obtained by calculating the inverse participation ratio (*IPR*) of the systems from the eigenfunctions in a Gaussian color noise model and compared.

6.3 Results and Discussions

Based on the above mentioned IPR technique, we analyzed several normal and cancerous breast, brain, and prostate cells by quantifying the structural disorder in their DAPI stained nuclear DNA, in terms of <*IPR*> values (≡ disorder strength).

6.3.1 Sample Preparation and Imaging

Primary cells and cell lines were acquired and cultured under the conditions recommended by the vendor. For fluorescence staining, the cells were plated onto sterile glass coverslips. Sub-confluent cultured cells plated on sterile glass coverslips were briefly rinsed in PBS and fixed for *5* minutes at room temperature with *2 – 4 %* paraformaldehyde in PBS. Cells were then washed 3

times five minutes in PBS and mounted on a glass slide using Prolong Diamond antifade mountant containing DAPI. The DAPI present in the mountant is a DNA binding dye that enables to visualize nuclei by fluorescence microscopy. For imaging, Nikon A1 confocal microscope was used with *405* nm laser, DAPI filter set, and *60*x oil immersion objective. Images were collected at pixel dimension *1024×1024*, with x-y resolution ~ $0.2 \times 0.2\ \mu m^2$, and the z-axis resolution of *0.13* μm.

From every z-stack of a cell nucleus, *2-3* confocal micrographs above and below the middle plane of the nucleus of a cell were taken for the analysis, constituting around *5-6* micrographs from the z-stack of each cell nucleus imaged. The choice of selecting images from around the middle of the stack is to cover maximum nuclear area and therefore capture maximum change. Subsequently, several cells from each cell type were imaged for the analysis.

6.3.2 Disorder Strength Analysis of Control and Cancerous Breast Cells

Structural disorder analyses of the DAPI stained nuclear DNA of breast cell lines, namely MCF-10A cells (normal/control) and MCF-7 (cancer) cells (American Type Culture Collection, Rockville, MD, USA), were performed. The MCF-10A cells which are regarded as non-tumorigenic [101,102] were used as control; while the tumorigenic MCF-7 cells which are associated with the metastatic adenocarcinoma stage were used as the cancer cells. The $\langle IPR \rangle$ values were calculated at different length scales L (i.e., in small areas $L \times L$ inside the sample) for all the cells and subsequently averaged for the 10-12 number of cells to obtain $\langle IPR \rangle$ at each length scale for both the cell lines. The experiments were repeated *3* times. The results are shown in Fig.6.2**.**

Figures 6.2(a) and 6.2(b) are the representative 2D confocal images of DAPI-stained nuclei from MCF-10A and MCF-7cells, respectively, exhibiting the staining intensity distribution, which essentially represents the DNA mass density distribution inside the nucleus.

The corresponding IPR images obtained at sample length (length scale) $L = 0.4\ \mu m$, i.e., sample size $A = 0.4 \times 0.4\ \mu m^2$, are shown in Figure 6.2(a') and 6.2(b'), respectively. The areas colored in red in the IPR images indicate regions with higher disorder strength, i.e., higher structural disorder. Figure 6.2(c) represents a bar graph comparison between the $<IPR>$ values of MCF-10A and MCF-7 cell lines measured at the length scale $1.6\ \mu m$, i.e., sample size $1.6 \times 1.6\ \mu m^2$.

The $<IPR>$ values for the MCF-10A and MCF-7 cells, at $L = 1.6\ \mu m$, were measured to be *2.55* and *2.76*, respectively. The spread of the $<IPR>$ values, measured in terms of the standard deviation of the measurement, turned out to be 0.04 and 0.07 for the MCF-10A and MCF-7 cells, respectively. A two tailed Student's *t*- test was performed by considering all the ensemble IPR values calculated for each cell types.

A p-value < 0.05 was obtained, which suggest that the mean disorder strength of the cancerous MCF-7 cells is significantly higher than the control MCF-10A cells. Subsequently, we also calculated $<IPR(L)>$ values at different length scales (sample size $L \times L\ \mu m^2$) for both the cell lines. The results, which are shown in Figure 6.2(d), indicate that the average disorder strength, $<IPR(L)>$, for the MCF-7 cells is higher than that of MCF-10A cells at all the measured length scales ranging from $L = 0.4$ to $1.6\ \mu m$. This reveals that the disorder strength of nuclear DNA of tumorigenic MCF-7 cells is greater than that of the control MCF-10A cells. Furthermore, this study suggests that degree of tumorigenicity in breast cancer cells can potentially be quantified by measuring the disorder strength of their nuclear DNA. Here it would be interesting to point out that the higher disorder strength of nuclear DNA of cancerous MCF-7 cells may be attributed to the spatial rearrangement of the DNA molecules inside the nucleus as result of compaction of the chromatin structure [103,104]

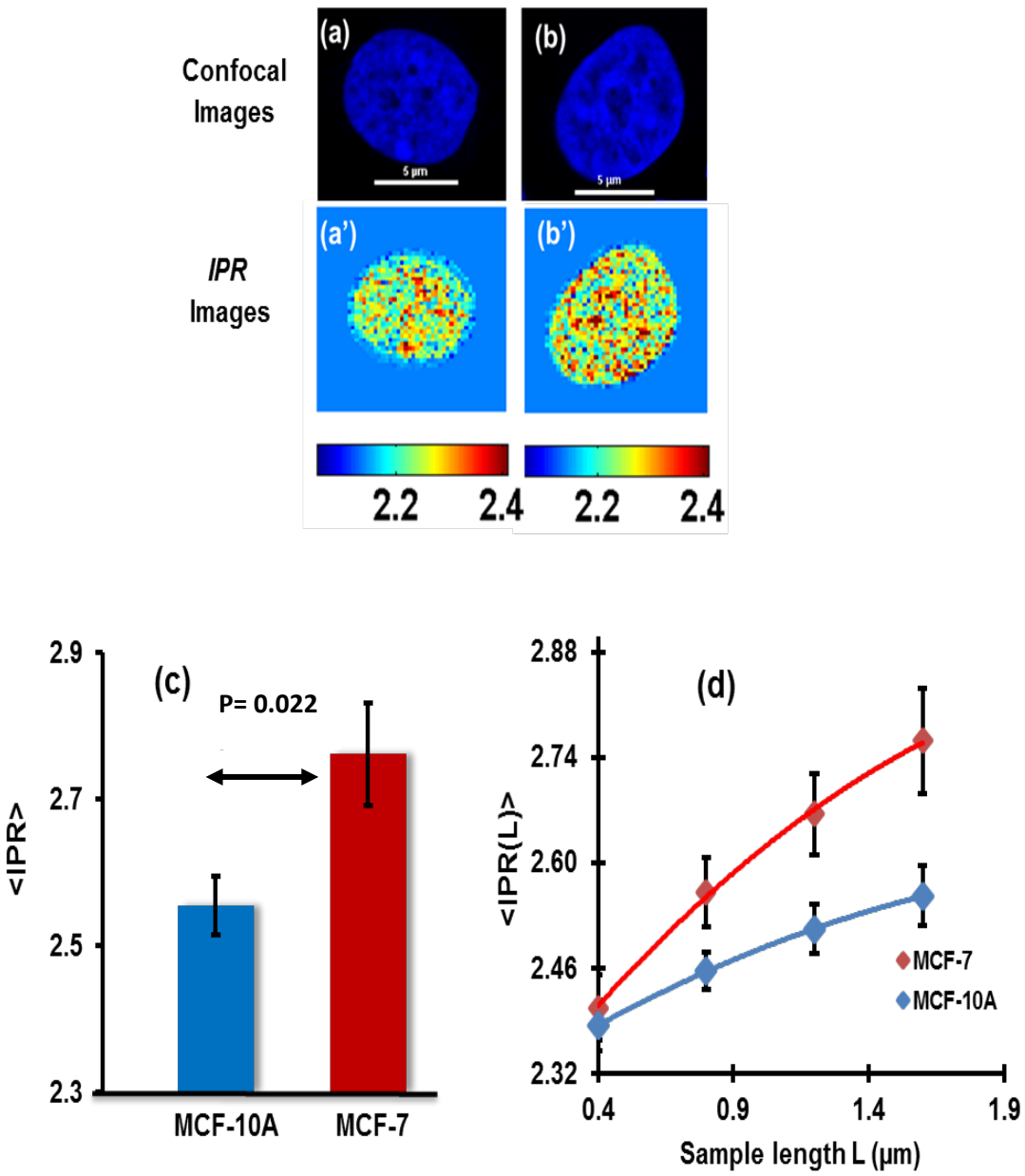

Figure 6.2: Structural disorder analysis of breast cell lines MCF-10A (control) and MCF-7 (cancerous). Sample size *n=34*. (a), (b): Representative confocal images of DAPI-stained nuclei from MCF-10A and MCF-7 cells representing intranuclear DNA distribution (scale bar in the image corresponds to *5 μm*) and (a'), (b') their corresponding IPR images at sample length *L= 0.4 μm (where, <IPR> = disorder strength*, measured in unit of area inverse*)*; (c): Bar graph comparing the structural disorder level at the sample length *L=1.6 μm*; (d): Structural disorder strength *<IPR(L)> vs*. sample length *L*. A *p*-value < *0.05* was obtained in the two tailed Student's *t*-test.

Such rearrangements of the nuclear DNA distribution leads to an increased mass density fluctuation of the DNA molecules distribution resulting in higher disorder strength. [51]

6.3.3 Disorder Strength Analysis of Normal and Cancerous Brain Cells

We studied the commercially available normal and cancerous human astrocytic cell lines. In particular, the 1) normal astrocyte (Lonza Group Ltd, Basel, Switzerland), 2) astrocyte progenitor (Applied Biological Material, Richmond, Canada) cells, and 3) U87 astrocytoma cells (American Type Culture Collection, Rockville, MD, USA).

The confocal micrographs of optical sections of nuclei were analyzed for structural disorder in the nuclear DNA using the methodology described in Section 2, and the results were evaluated statistically. The degree of structural disorder $L_{sd,}$ in terms of IPR values, were calculated for different length scales ranging from L=0.4 to 1.6 μm. Subsequently, all the IPR values were averaged for ~3-5 confocal micrographs for each single cell nucleus, and 12-15 cells from each of the cell line categories were analyzed. The experiment was repeated for 3 different sets of cells.

Typical results comparing L_{sd} in all the three types of cells are shown in Fig.6.3. The figures 6.3(a), 6.3(b), and 6.3(c) show representative confocal images of the 1) normal astrocyte, 2) astrocyte progenitor, and 3) U87 astrocytoma cell's nucleus, respectively. The images presented in Figs. 6.3(a'), 6.3(b'), and 6.3(c') are their corresponding IPR images obtained at sample length L= 0.4 μm. These *IPR* images show the distribution of the *IPR* values (i.e., L_{sd}) calculated in the sample area of $0.4\times0.4\ \mu m^2$ inside the nucleus of the two cells.

As it can be seen in the figures 6. 3(a), 6.3(b), and 6.3(c) that the confocal images for the nucleus of the three cells, i.e., 1) normal astrocyte, 2) astrocyte progenitor, and 3) U87 astrocytoma, the *IPR* image shows more prominent hot spots (red spots) regions in the cancerous astrocyte progenitor and U87 astrocytoma cell nucleus in comparison to the normal astrocyte cell nucleus. It should also be noted that variation in the *IPR* values for the cancerous astrocyte

progenitor and U87 astrocytoma cells are much higher, that is 1.4 –2, than the normal astrocyte cells. This suggests a significantly higher DNA mass density variation, in terms of magnitude and spatial arrangement, in the cancerous astrocyte cells' nuclei compared to the normal astrocyte cells, in turn indicating the higher degree of structural disorder in the nuclear DNA in the cancerous case.

A comparison of structural disorder, L_{sd} , in terms of average <IPR> values, between the normal and the cancerous astrocyte cells types, is shown in Fig.6. 3(d). The bar graph shows the (<IPR>) at length scale 1.6 μm, i.e., 1.6×1.6 μm2 areas inside the sample. The p-value obtained from the Student's *t*-test (sample size > 45) turned out to be < 0.05 for all the pairs, demonstrating that the structural disorder in the nuclear DNA of the cancerous astrocyte progenitor and U87 astrocytoma cells is significantly higher than that of the normal astrocyte cells, and so is the difference between astrocyte progenitor and U87 astrocytoma cells.

Furthermore, we also examined (<IPR(L)>) for all the cells types at different sample lengths L ranging from 0.4–1.6 μm. The results are shown in Fig.6. 3(e). The results show that average structural disorder L_{sd} is higher for cancer cells compared to their non-cancerous counterpart, for all the length scales studied. Further, it is interesting to note in Fig.6. 3(e) that(<IPR(L)>) for the normal astrocyte cells starts showing the saturating trend at higher sample lengths, which is in accordance with Eq. 2. It would be worth pointing out here that the (<IPR(L)>) graphs for the cancerous cases would also ultimately saturate at significantly higher sample length; a trend towards saturation can still be seen in the present plots.

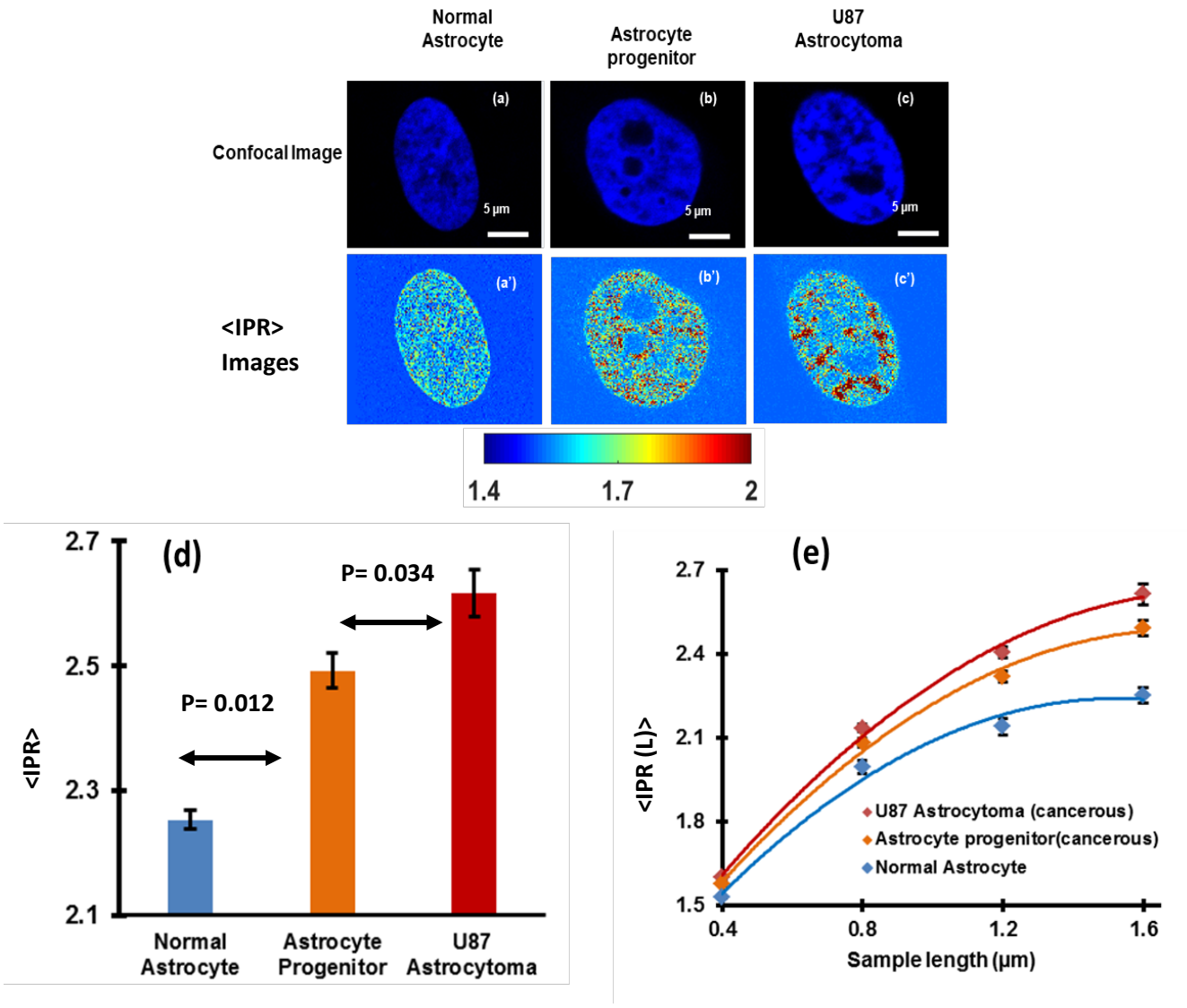

Figure 6.3: (a), (b), and (c): Representative confocal images of a normal astrocyte, an astrocyte progenitor, and a U87 astrocytoma cell nuclei, respectively and (a') - (c'): their corresponding disorder strength *(IPR)* images at sample length *L =0.4 µm;*(d): Bar plots for mean *IPR* values (n=12-15 cells, 3-5 micrographs per cell, 3 sets) for the normal astrocyte, astrocyte progenitor, and U87 astrocytoma cells nuclei at sample length L= 1.6 µm.; Student's t-test obtained p-value < 0.05 for each pair; (e) Structural disorder at different sample length scales (L) (sample size L×L), for each type of normal astrocyte, astrocyte progenitor, and U87 astrocytoma cells The scale bar in the confocal image corresponds to 5 µm.

The higher L_{sd} values for tumorigenic astrocyte progenitor and U87 astrocytoma cells suggest more structural alterations in its nuclear DNA and chromatin when compared to normal astrocyte cells. The higher structural disorder in nuclear DNA of the cancerous cells may be

attributed to the unfolding of the heterochromatin inside the nuclei, which occurs during carcinogenesis.[105]

6.3.4 Disorder Strength Analysis of Normal and Cancerous Prostate Cells

After the breast and brain cancer cells experiments, we used the IPR technique to analyze disorder strengths of the DAPI stained nuclear DNA of normal and cancerous human prostate cells. The prostate cell nuclei were confocal imaged all together on a slide in a single shot to reduce extra effort of imaging one cell at a time.

In this study, we used the well-characterized following cell lines; i) normal prostate PWR cells, ii) tumorigenic and low metastatic LNCaP (AR-dependent), iii) tumorigenic and moderate metastatic DU145 (AR-independent), and iv) tumorigenic and highly bone metastatic C4-2 (AR-independent) cell lines. Based on their cellular and molecular characteristics, these cell lines are well-established *in vitro* models of early- and advance-stage prostate cancer, and their tumorigenicity levels and metastatic potentials well known [106–111]

Figures 6.4 (a), (b), (c), and (d) show the confocal fluorescence micrographs of DAPI stained prostate cell nuclei on glass slides exhibiting nuclear DNA distribution of PWR (normal prostate cell) and the cancerous LNCaP, DU145, and C4-2 cell lines, respectively. The images shown in Figures 6.4(a'), (b'), (c'), and (d') are their corresponding IPR images obtained at sample length $L = 1.40\ \mu m$. As explained above, the red-region represent higher structural disorder in that region. Based on disorder strength distribution, as seen in the IPR images, the three metastatic cell lines appear clearly distinct from the normal PWR prostate cells, suggesting higher structural disorder level in these cancer cells.

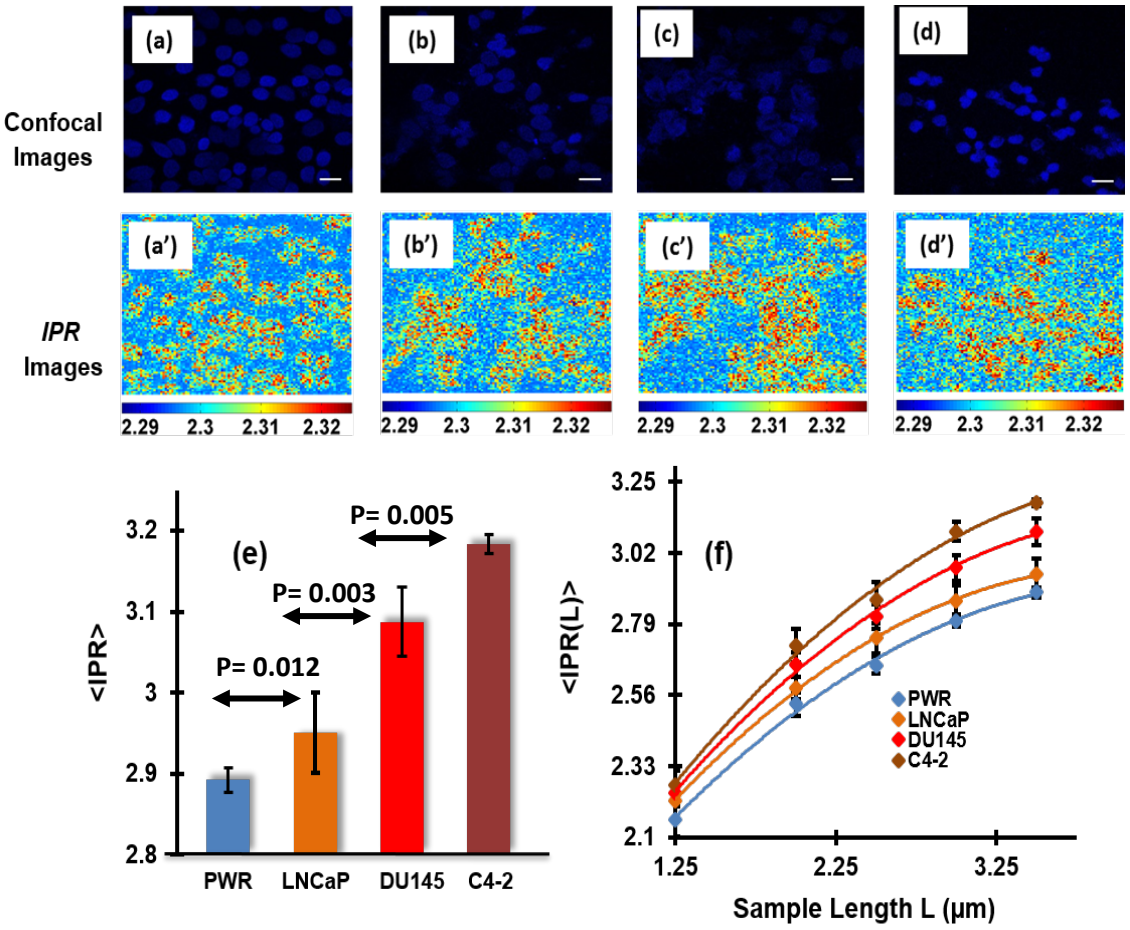

Figure 6.4: Structural disorder analysis of prostate cells. Sample size *n=31-35* (a) - (d): Confocal images of several DAPI-stained nuclei from PWR, LNCaP, DU145, and C4-2 prostate cell lines taken in a single shot (scale bar in the image corresponds to *20 μm*) and (a') - (d') their corresponding disorder strength *<IPR>* images at sample length *L= 1.40 μm*; (e): Bar graph comparison at *3.5 μm* sample length scale; *p*-value measured in 2-tailed Student's *t*-test for each pair of the measurement *< 0.05* (f): *<IPR(L)> vs*. sample length scale *L* (sample size *L* × *L*) observed for all cells studied.

In further analyses, *8-12* cell nuclei of each cell category were randomly picked from the confocal micrographs, and the IPR analysis was performed for each nucleus separately. The experiments were repeated three times. Typical nucleus size was around *7-10 μm*. The bar graph in Fig.6.4(e) shows disorder strengths comparison for all the prostate cell lines examined at the

length scale *3.5 μm*. At this length scale, the <*IPR*> values for all the four types of prostate cell lines, namely the PWR, LNCaP, DU145 and C4-2, were measured to be 2.89, 2.95, 3.08 and 3.18, respectively. Additionally, the spread of the <*IPR*> values in each cell type, measured in terms of the standard deviation of the measurement, was noted to be 0.015, 0.049, 0.043 and 0.011, for the PWR, LNCaP, DU145, and C4-2 cell lines, respectively.

These results show that the disorder strength for all the metastatic prostate cancer cell lines are higher compared to the normal prostate PWR cells. The disorder strength calculated for the AR-independent C4-2 cell line (Fig.6.4 (d')) was higher than that calculated for LNCaP cells (Fig.6.4(b')). Since C4-2 is derived from the LNCaP cell line, it is expected to have higher tumorigenicity and metastatic potential compared to LNCaP, which agrees well with our results. Further, in this work, the disorder strengths calculated for the PWR, LNCaP, DU145, and C4-2 cell lines are in increasing order, which is in accordance with the hierarchy of their tumorigenicity levels and metastatic potential. From the two tailed Student's *t*-test, conducted on the ensemble IPR values, a *p*-value < 0.05 was obtained for each pair of the statistical data. The structural disorder strengths were also analyzed at different length scales (*1.25 – 3.5 μm*) for each cell category. The plots are shown in Figure 6.4(f). Again, the <*IPR*> values for all the metastatic prostate cancer cell lines turned out to be higher than the normal PWR cells at all length scales examined.

As pointed out earlier, the increase in <*IPR*> values, and hence the disorder strength with increase in tumorigenicity levels in the prostate cancer cells can be attributed to the changing configuration of DNA inside the nucleus. The progression of carcinogenesis is followed by compaction of the chromatin structure inside the nucleus. The compaction of the chromatin structure results in higher mass density fluctuation which causes higher disorder strength. To put

it simply, lower disorder strengths in cells (e.g., for normal or lesser metastatic cells), suggest that nuclear DNA mass density in them is relatively more uniformly distributed compared to the cells with higher disorder strengths, such as the higher metastatic cells.

6.4 Correlation between Structural Disorder, Tumorigenicity, and Hierarchy

The outcomes of the present study for prostate cancer cells are promising for the quantification of structural alterations inside the cells. The IPR technique in conjunction with confocal fluorescence microscopy could be highly useful in diagnosing different levels of cancer. However, since this would require development of a robust calibration curve with different cancer types, we present herein a framework for a potential calibration curve for analyzing the tumorigenicity level in carcinogenesis. A calibration curve for real application purposes should be developed with data from extensive clinical studies, along the similar direction.

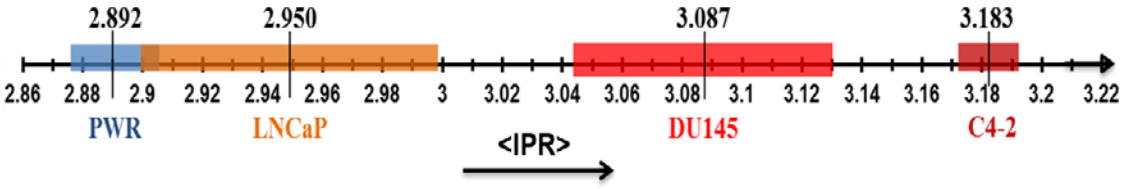

Figure 6.5: A proposed representative calibration curve for cell tumorigenicity: nuclear DNA structural disorder <*IPR*> determined at the sample length of *3.5 μm vs.* tumorigenicity level inside the prostate cells.

Figure 6.5 shows a framework for a calibration curve for the prostate cancer case studied above. The structural disorder strength, as examined for sample size $3.5 \times 3.5\ \mu m^2$ and measured for all four types of prostate cells, has been drawn with respect to their increasing order of tumorigenicity, in a single-line <*IPR*> spectrum. Therefore, each colored block in Fig.6.5 represents the spread of the <*IPR*> values measured for the normal and cancer prostate cell lines

in this study. Each block is marked in the middle with the mean <*IPR*> values 2.8925, 2.9506, 3.0876, and 3.1835, corresponding to the PWR, LNCaP, DU145, and C4-2 cell lines, respectively. This representative calibration line plot attempts a quantitative evaluation of tumorigenicity and metastatic potential in any unknown prostate cancer cell type through a graded evaluation, as suggested above. Such a calibration chart demonstrates the potential capability to predict cancer stages.

6.5 Comparison between the IPR and the PWS Approach in the Structural Disorder Measurements

Both, the IPR and the PWS techniques measure the structural disorder based on mesoscopic physics principles. IPR measures the nanoscale structural alteration, whereas the IPR technique measure the submicron scale structural alterations. The PWS takes its strength from the use of the raw spectrum data from backscattering imaging of the sample, without its further manipulation, such as Fourier transform, in conducting the structural disorder analysis. The IPR technique takes its strength from the fluorescence imaging data in confocal microscopy imaging. Both the techniques use single parameter, namely ‘disorder strength ‘but of different form, instead of multiple parameters, to quantify structural alterations and characterize the heterogeneity of the cells. However, there are some differences between the two techniques which make each of techniques unique as well as special in its own respect. For example, PWS measure the structural disorder along the depth of the sample. In other words, PWS detects the refractive index fluctuations in one dimension (1D). Even though at this point, PWS is not depth sensitive technique, because we are using a very thin transparent sample (cells), it can be easily modified to measure the structural disorder at different depths inside a thick sample such as tissues. Whereas the IPR measures the structural disorder in a 2D plane of the sample where it

detects the refractive index fluctuations in that plane. The PWS measures structural disorder of whole sample (biological cells in our case), while the IPR technique measures the structural disorder of a selected organelle in the cells. Also, PWS measurement is directly proportional to the variance of the refractive index fluctuation, however, IPR measurement is proportional to the standard deviation (sqrt(variance)) of the refractive index fluctuations. By keeping in mind, the similarities and differences between the two techniques, in this work we have tried to gain insight into the trends that each technique predicts for disorder strength in present cancer detection study, and have compared the results obtained from these two techniques.

Therefore, in figure 6.6, we plot the average L_{sd} vs. the average *IPR* for the normal and cancerous cell types based on our studies of the disorder strength in the two groups (a) brain, (b) prostates cancer cell lines in this chapter an d chapters 3 and 4. Clearly, both L_{sd} and IPR are higher for the cancerous cells compared to the normal cells in all the three groups. Similarly, in the three groups of cell lines L_{sd} and *IPR* move in the same direction that we notice when the *IPR* increases, L_{sd} increases and vice versa. This suggests a strong positive linear correlation between the two parameters. Since we have a limited sample numbers in each cell lines (brain breast, prostate), calculating the exact correlation coefficient or mathematical relationship between the two methods may not be appropriate at this point. Exact correlation coefficient values can be obtained with large sample numbers, such as in clinical studies.

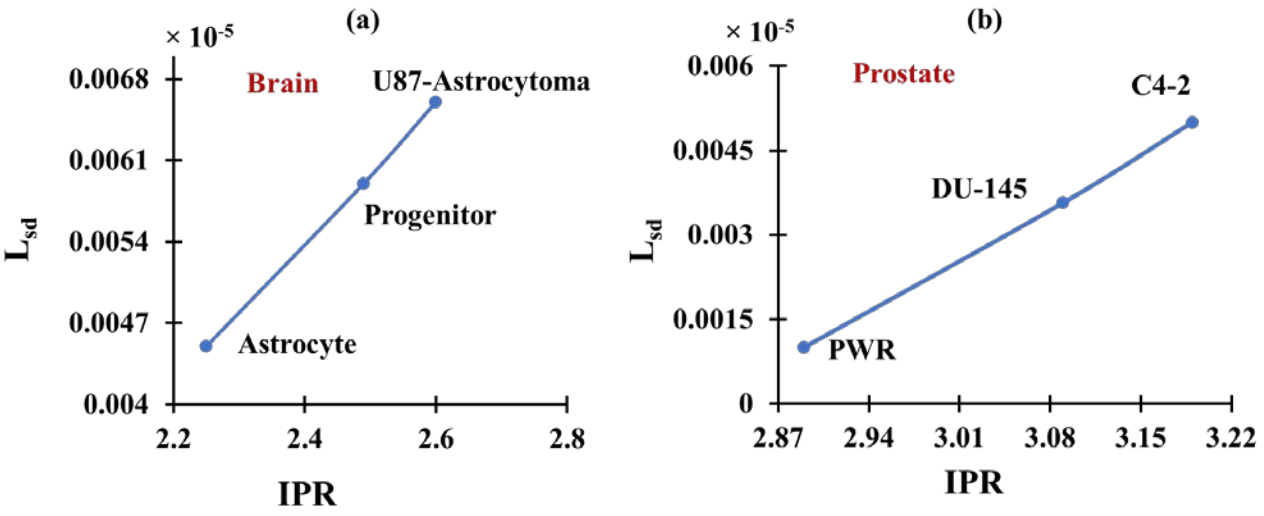

Figure 6.6: Comparison between the IPR and PWS in the structural disorder measurements. The average L_{sd} vs. the average *IPR* for the normal and cancerous cell types in the two groups: (a) brain, (b) prostate.

6.6 Conclusion

In conclusion, we have developed a novel method to quantify refractive index fluctuations in weakly disordered heterogeneous optical system using confocal fluorescence microscopy imaging. Cells were studied to evaluate the potential utility of the technique for bio-medical applications, in particular, cancer detection. Our results show that confocal fluorescence micrographs can be used to extract refractive index fluctuations, or conversely the mass density fluctuations information inside a weakly disordered heterogeneous optical medium represented by cells. Further, we showed that such analysis can be performed at the submicron level using one single parameter– the degree of structural disorder L_{sd} in terms of the inverse participation ratio (IPR), values. We performed all the study with commercially available normal and cancerous breast, brain, and, prostate and demonstrated that the proposed method provides a numerical mean to distinguish these cell types based on its mass density variation of the nuclear DNA. In particular, the nuclei of the cells were chosen to compare structural disorder in the

DNA, as in the case carcinogenesis DNA inside the cell nuclei is known to undergo alterations. The promising result obtained in this work suggests that our method can also have potential applications in analyzing other cellular abnormalities or disease conditions, such as sickle cell anemia, metabolic or mechanical stress, and response of cells to therapeutic agents, just to name a few. The method has the capability to detect any structural changes in a nucleus, regardless of its origin. Therefore, the method should potentially work for dye-treated live cells as well. The way the technique has been formulated, it should work for any type of dye-targeting any organelle, as long as the absorption of the dye at a point in the organelle has a functional relationship with the mass density of the dye present at that point. This method would be also useful without dye if the confocal imaging of the cell can detect sufficient mass density variations. Finally, our method may also be useful for materials science of soft optical disordered media, such as polymers and thin films, in characterizing the structural disorder of the sample using the similar approach.

7 Conclusion and Future Directions

This dissertation provides insight into the usefulness of the mesoscopic light transport and light localization analysis in quantifying structural disorder in biological cells in which the structural alterations, caused by cancer diseases, is measured in terms of refractive index (RI) fluctuation (*dn*), and its correlation length, l_c. As the cancer progresses, a change in the spatial distribution of the intracellular mass density starts occurring due to the alterations in the cell's architecture in the length scale ranging from nano- to sub-micrometer, consequently, leading to higher structural disorders in the cell. We hypothesized that the structural disorder is correlated with the cancer progression and its measurement can be used as a biomarker/numerical index to characterize cancer. We tested this hypothesis experimentally, by employing the two mesoscopic techniques, namely light transport analysis based partial wave spectroscopy (PWS) and light localization analysis based inverse participation ratio (IPR) technique to investigate the structural changes in human cancer cell line models. The main results reported in this dissertation are the following:

1. **PWS Study of the Structural Alterations in the Breast and Brain Cancer Cell Lines**. Our first study (Chapter 3) on the breast (MCF-10A and MCF-7) and brain (Astrocyte, Astrocyte progenitor, and U-87 astrocytoma) cell lines models, we distinguished the cancerous and control cells by quantifying the structural disorder using the PWS method. Our statistical analysis of the disorder strength showed higher mean intracellular disorder strength in the cancerous cases. Moreover, the spread of disorder strength values for cancerous cells was also observed to be higher than the normal/control cells. Our results demonstrate that the increase in intracellular structural alterations is indeed associated with the progressive carcinogenesis, suggesting increasing heterogeneity in the cells. Even

though, we did not identify specific structures/building blocks that are responsible for the increase in structural disorder, however, an overall global increase in disorder strength is observed for the cancerous cells relative to control cells.

2. **Study of the Chemotherapy Resistance Based on the Structural Alterations in Three Types of Prostate Cancer Cells Lines.** Our second study (Chapter 4) quantifies the degree of disorder in three types of metastasized prostate cells, namely DU-145, C4-2, and PC-3 after drug-induced resistance has been developed over a period of around 8 months in the prostate cells. In this study, the structural disorder analysis was conducted using the PWS method. We compared the results of the degree of structural disorder measured for the age-matched non-drug treated, i.e., drug-sensitive, prostate cells with their counterpart drug-resistant cells. It turned out that the drug-resistive cells in each category had a higher structural disorder with percentage increase in disorder strengths in the drug-resistive cells, relative to their corresponding non-drug treated cells, was more than 30%, suggesting higher level of heterogeneity in the drug resistive cells.

3. **Study of Structural alterations in Selective Organelles in the Cells Using the IPR Technique** Our third study (Chapters 5 and 6) introduced and explored the IPR technique based on the confocal imaging of cells. Using confocal imaging, molecular specific optical lattices were constructed for a particular layer of a cell. The degree of structural changes of theses optical lattices were evaluated by calculating their light localization strength through the statistical analysis of the eigenfunctions of these lattices. The measurement parameter is the average *inverse participation ratio* (IPR) value of the eigenfunctions of

these lattice systems, where the average IPR value of a disordered optical lattice is termed as ‘disorder strength’ of the lattice. In this work, we measured submicron scale disorder strength of DAPI stained nuclear DNA in the breast (MCF-10A and MCF-7), brain (Astrocyte, Astrocyte progenitor, and U-87 astrocytoma) and prostate (PWR, LNCaP, DU-145, and C4-2) cell lines of different tumorigenicity (metastatic potential) levels. The results showed that the disorder strength, measured for the nuclear DNA molecular spatial structural disorder of these cells, increases in accordance with increase in the tumorigenicity levels of these cells. The results showed that the light localization analysis using confocal fluorescence imaging has potential to efficiently distinguish different cancerous and normal breast, brain and prostate cells by analyzing the structural disorder strength of nuclear DNA spatial mass density inside these cells.

In summary, the studies performed in this dissertation work lead us to the key finding that the quantification of spatial structural disorder of the biological cells based on mesoscopic light transport and light localization approaches are indeed promising methods where the disorder strength, measured as described in the respective PWS and IPR sections, can act as a potential biomarker or numerical index to characterize any progressive carcinogenesis. In the future work, the main aim would be to make improvements in these measurement techniques so that it can be used in clinical settings with large scale clinical trials. First, fully automated, this new partial wave microscopic spectroscopy setup has to be developed, and in the next step where the experiment can be performed with better image quality and reduced noise performance and shorter analysis time. Moreover, automated IPR analysis would rather save a great deal of time. The study of the disorder strength discussed in this dissertation performed on thin cells and the results from thin tissues may be different which needs to be investigated for generalization of

this method for studying of tissue. Further, the quantitative IPR technique will be more useful to pathologist who uses stained thin cells/tissue sections for cancer screening and grade classification by distinguishing them visually. In addition, the preliminary results presented here are promising that helped us to lay down the applications of the mesoscopic physics based techniques, however, for real clinical implementation, further extensive studies with larger samples size and clinical trials are necessary to reach to the larger goal in cancer diagnostics in medical care.

References

1. Rubin R, Strayer DS, Rubin E. *Rubin's Pathology: Clinicopathologic Foundations of Medicine*. Lippincott Williams & Wilkins; 2008.

2. Adhyam M, Gupta AK. A review on the clinical utility of PSA in cancer prostate. *Indian journal of surgical oncology*. 2012;3(2):120–129.

3. Meigs JB, Barry MJ, Oesterling JE, Jacobsen SJ. Interpreting results of prostate-specific antigen testing for early detection of prostate cancer. *Journal of general internal medicine*. 1996;11(9):505–512.

4. Boustany NN, Tsai YC, Pfister B, Joiner WM, Thakor NV, Oyler GA. Light scattering by apoptotic cells. In: *Frontiers in Optics*. Optical Society of America; 2003:WZ1.

5. Hackenbrock CR. Ultrastructural bases for metabolically linked mechanical activity in mitochondria: I. Reversible ultrastructural changes with change in metabolic steady state in isolated liver mitochondria. *The Journal of cell biology*. 1966;30(2):269–297.

6. Wyatt PJ. Differential light scattering: a physical method for identifying living bacterial cells. *Applied optics*. 1968;7(10):1879–1896.

7. Wyatt PJ. Light scattering and the absolute characterization of macromolecules. *Analytica chimica acta*. 1993;272(1):1–40.

8. Wax A, Backman V. *Biomedical Applications of Light Scattering*. McGraw Hill Professional; 2009.

9. Marx E, Mulholland GW. Size and refractive index determination of single polystyrene spheres. *J Res Nat Bur Stand*. 1983;88(5):321–338.

10. Colthup N. *Introduction to Infrared and Raman Spectroscopy*. Elsevier; 2012.

11. Mourant JR, Bigio IJ, Boyer JD, et al. Elastic scattering spectroscopy as a diagnostic tool for differentiating pathologies in the gastrointestinal tract: preliminary testing. *Journal of Biomedical Optics*. 1996;1(2):192–200.

12. Choi WJ, Jeon DI, Ahn S-G, Yoon J-H, Kim S, Lee BH. Full-field optical coherence microscopy for identifying live cancer cells by quantitative measurement of refractive index distribution. *Optics express*. 2010;18(22):23285–23295.

13. Backman V. Erratum: Detection of preinvasive cancer cells (Nature (2000) 406 (35-36)). *Nature*. 2000;408(6811):428.

14. Bista RK, Uttam S, Wang P, et al. Quantification of nanoscale nuclear refractive index changes during the cell cycle. *Journal of biomedical optics*. 2011;16(7):070503.

15. Phillips KG, Velasco CR, Li J, et al. Optical quantification of cellular mass, volume, and density of circulating tumor cells identified in an ovarian cancer patient. *Frontiers in oncology*. 2012;2:72.

16. Wang Z, Popescu G, Tangella KV, Balla A. Tissue refractive index as marker of disease. *Journal of biomedical optics*. 2011;16(11):116017.

17. Zhernovaya OS, Bashkatov AN, Genina EA, et al. Investigation of glucose-hemoglobin interaction by optical coherence tomography. In: *Saratov Fall Meeting 2006: Optical Technologies in Biophysics and Medicine VIII*. Vol 6535. International Society for Optics and Photonics; 2007:65351C.

18. Meng Z, Yao XS, Yao H, et al. Measurement of the refractive index of human teeth by optical coherence tomography. *Journal of biomedical optics*. 2009;14(3):034010.

19. Wang TD, Van Dam J. Optical biopsy: a new frontier in endoscopic detection and diagnosis. *Clinical gastroenterology and hepatology*. 2004;2(9):744–753.

20. Beuthan J, Minet O, Helfmann J, Herrig M, Müller G. The spatial variation of the refractive index in biological cells. *Physics in Medicine & Biology*. 1996;41(3):369.

21. Boustany NN, Boppart SA, Backman V. Microscopic imaging and spectroscopy with scattered light. *Annual review of biomedical engineering*. 2010;12:285–314.

22. Liu PY, Chin LK, Ser W, et al. Cell refractive index for cell biology and disease diagnosis: past, present and future. *Lab on a Chip*. 2016;16(4):634–644.

23. Tuchin V. Tissue optics: light scattering methods and instruments for medical diagnosis.

24. Kinoshita S. *Bionanophotonics: An Introductory Textbook*. CRC Press; 2013.

25. Boustany NN, Thakor NV. Light scatter spectroscopy and imaging of cellular and subcellular events. *Biomedical Photonics Handbook*. 2002:16–1.

26. Zaccanti G, Taddeucci A, Barilli M, Bruscaglioni P, Martelli F. Optical properties of biological tissues. In: *Optical Tomography, Photon Migration, and Spectroscopy of Tissue and Model Media: Theory, Human Studies, and Instrumentation*. Vol 2389. International Society for Optics and Photonics; 1995:513–522.

27. Pradhan P, Damania D, Joshi HM, et al. Quantification of nanoscale density fluctuations using electron microscopy: Light-localization properties of biological cells. *Applied physics letters*. 2010;97(24):243704.

28. Schmitt JM, Kumar G. Turbulent nature of refractive-index variations in biological tissue. *Optics letters*. 1996;21(16):1310–1312.

29. Waters JC. *Accuracy and Precision in Quantitative Fluorescence Microscopy*. Rockefeller University Press; 2009.

30. Lee PA, Ramakrishnan TV. Disordered electronic systems. *Reviews of Modern Physics*. 1985;57(2):287.

31. Pradhan P, Damania D, Joshi HM, et al. Quantification of nanoscale density fluctuations by electron microscopy: probing cellular alterations in early carcinogenesis. *Physical biology*. 2011;8(2):026012.

32. Rammal R, Douçot B. Invariant imbedding approach to localization. I. General framework and basic equations. *Journal de Physique*. 1987;48(4):509–526.

33. Subramanian H, Pradhan P, Liu Y, et al. Partial-wave microscopic spectroscopy detects subwavelength refractive index fluctuations: an application to cancer diagnosis. *Optics letters*. 2009;34(4):518–520.

34. Figliola RS, Beasley D. *Theory and Design for Mechanical Measurements*. John Wiley & Sons; 2015.

35. High Power Mercury-Xenon Light Sources. https://www.newport.com/f/research-arc-lamp-sources-450-1000-w. Accessed March 9, 2018.

36. 44-140156DTS_010053A_01_VariSpec_DTS.pdf. https://www.perkinelmer.com/CMSResources/Images/44-140156DTS_010053A_01_VariSpec_DTS.pdf. Accessed March 9, 2018.

37. Barber PW, Hill SC. *Light Scattering by Particles: Computational Methods*. Vol 2. World scientific; 1990.

38. Murphy DB. *Fundamentals of Light Microscopy and Electronic Imaging*. John Wiley & Sons; 2002.

39. Siegel RL, Miller KD, Jemal A. Cancer statistics, 2018. *CA: a cancer journal for clinicians*. 2018;68(1):7–30.

40. Biopsy Procedure | American Brain Tumor Association. http://www.abta.org/brain-tumor-information/diagnosis/biopsy-procedure.html. Accessed March 10, 2018.

41. Rakha EA, Reis-Filho JS, Baehner F, et al. Breast cancer prognostic classification in the molecular era: the role of histological grade. *Breast Cancer Research*. 2010;12(4):207.

42. He L, Long LR, Antani S, Thoma GR. Histology image analysis for carcinoma detection and grading. *Computer methods and programs in biomedicine*. 2012;107(3):538–556.

43. Ross KFA, Billing EVE. The water and solid content of living bacterial spores and vegetative cells as indicated by refractive index measurements. *Microbiology*. 1957;16(2):418–425.

44. Choi W, Fang-Yen C, Badizadegan K, et al. Tomographic phase microscopy. *Nature methods*. 2007;4(9):717.

45. Rammal R, Douçot B. Invariant imbedding approach to localization. I. General framework and basic equations. *Journal de Physique*. 1987;48(4):509–526.

46. Tuchin VV. Control of tissue and blood optical properties. *NATO SCIENCE SERIES SUB SERIES I LIFE AND BEHAVIOURAL SCIENCES*. 2005;369:79.

47. Subramanian H, Pradhan P, Liu Y, et al. Optical methodology for detecting histologically unapparent nanoscale consequences of genetic alterations in biological cells. *Proceedings of the National Academy of Sciences*. 2008;105(51):20118–20123.

48. Wang P, Bista R, Bhargava R, Brand RE, Liu Y. Spatial-domain low-coherence quantitative phase microscopy for cancer diagnosis. *Optics letters*. 2010;35(17):2840–2842.

49. Damania D, Subramanian H, Tiwari AK, et al. Role of cytoskeleton in controlling the disorder strength of cellular nanoscale architecture. *Biophysical journal*. 2010;99(3):989–996.

50. Roy HK, Turzhitsky V, Kim Y, et al. Association between rectal optical signatures and colonic neoplasia: potential applications for screening. *Cancer research*. 2009;69(10):4476–4483.

51. Kim JS, Pradhan P, Backman V, Szleifer I. The influence of chromosome density variations on the increase in nuclear disorder strength in carcinogenesis. *Physical biology*. 2011;8(1):015004.

52. Siegel RL, Miller KD, Jemal A. Cancer statistics, 2017. *CA: A Cancer Journal for Clinicians*. 2017;67(1):7-30. doi:10.3322/caac.21387

53. Prostate Cancer: What Are The Risk Factors? *PCF*. August 2016. https://www.pcf.org/c/prostate-cancer-risk-factors/. Accessed March 10, 2018.

54. De Bono JS, Oudard S, Ozguroglu M, et al. Prednisone plus cabazitaxel or mitoxantrone for metastatic castration-resistant prostate cancer progressing after docetaxel treatment: a randomised open-label trial. *The Lancet*. 2010;376(9747):1147–1154.

55. Tannock IF, Osoba D, Stockler MR, et al. Chemotherapy with mitoxantrone plus prednisone or prednisone alone for symptomatic hormone-resistant prostate cancer: a Canadian randomized trial with palliative end points. *Journal of Clinical Oncology*. 1996;14(6):1756–1764.

56. Yagoda A, Petrylak D. Cytotoxic chemotherapy for advanced hormone-resistant prostate cancer. *Cancer*. 1993;71(S3):1098–1109.

57. Prostate Cancer: Treatment Options. Cancer.Net. https://www.cancer.net/cancer-types/prostate-cancer/treatment-options. Published June 25, 2012. Accessed March 10, 2018.

58. Hwang C. Overcoming docetaxel resistance in prostate cancer: a perspective review. *Therapeutic advances in medical oncology*. 2012;4(6):329–340.

59. Ganju A, Yallapu MM, Khan S, Behrman SW, Chauhan SC, Jaggi M. Nanoways to overcome docetaxel resistance in prostate cancer. *Drug Resistance Updates*. 2014;17(1-2):13–23.

60. Zhang W, Meng Y, Liu N, Wen X-F, Yang T. Insights into chemoresistance of prostate cancer. *International journal of biological sciences*. 2015;11(10):1160.

61. O'Neill AJ, Prencipe M, Dowling C, et al. Characterisation and manipulation of docetaxel resistant prostate cancer cell lines. *Molecular cancer*. 2011;10(1):126.

62. Nagesh PK, Johnson NR, Boya VK, et al. PSMA targeted docetaxel-loaded superparamagnetic iron oxide nanoparticles for prostate cancer. *Colloids and Surfaces B: Biointerfaces*. 2016;144:8–20.

63. Shah AN, Summy JM, Zhang J, Park SI, Parikh NU, Gallick GE. Development and characterization of gemcitabine-resistant pancreatic tumor cells. *Annals of surgical oncology*. 2007;14(12):3629–3637.

64. Yang AD, Fan F, Camp ER, et al. Chronic oxaliplatin resistance induces epithelial-to-mesenchymal transition in colorectal cancer cell lines. *Clinical cancer research*. 2006;12(14):4147–4153.

65. Corcoran C, Rani S, O'Brien K, et al. Docetaxel-resistance in prostate cancer: evaluating associated phenotypic changes and potential for resistance transfer via exosomes. *PloS one*. 2012;7(12):e50999.

66. Khan S, Maher D, Ebeling M, Kumar D, Jaggi M, Chauhan SC. *MicroRNA-145 Targets MUC13 and Suppresses Invasion and Metastasis of Pancreatic Cancer Cells.* AACR; 2013.

67. Zaman MS, Chauhan N, Yallapu MM, et al. Curcumin nanoformulation for cervical cancer treatment. *Scientific reports*. 2016;6:20051.

68. Liu AY, Brubaker KD, Goo YA, et al. Lineage relationship between LNCaP and LNCaP-derived prostate cancer cell lines. *The Prostate*. 2004;60(2):98–108.

69. Stone KR, Mickey DD, Wunderli H, Mickey GH, Paulson DF. Isolation of a human prostate carcinoma cell line (DU 145). *International journal of cancer*. 1978;21(3):274–281.

70. Pulukuri SM, Gondi CS, Lakka SS, et al. RNA interference-directed knockdown of urokinase plasminogen activator and urokinase plasminogen activator receptor inhibits prostate cancer cell invasion, survival, and tumorigenicity in vivo. *Journal of Biological Chemistry*. 2005;280(43):36529–36540.

71. Plastaras JP, Guengerich FP, Nebert DW, Marnett LJ. Xenobiotic-metabolizing cytochromes P450 convert prostaglandin endoperoxide to hydroxyheptadecatrienoic acid and the mutagen, malondialdehyde. *Journal of Biological Chemistry*. 2000;275(16):11784–11790.

72. Michael M, Doherty MM. Tumoral drug metabolism: overview and its implications for cancer therapy. *Journal of Clinical Oncology*. 2005;23(1):205–229.

73. Zahreddine H, Borden K. Mechanisms and insights into drug resistance in cancer. *Frontiers in pharmacology*. 2013;4:28.

74. Housman G, Byler S, Heerboth S, et al. Drug resistance in cancer: an overview. *Cancers*. 2014;6(3):1769–1792.

75. Yang AD, Fan F, Camp ER, et al. Chronic oxaliplatin resistance induces epithelial-to-mesenchymal transition in colorectal cancer cell lines. *Clinical cancer research*. 2006;12(14):4147–4153.

76. Inoué S. Foundations of confocal scanned imaging in light microscopy. In: *Handbook of Biological Confocal Microscopy*. Springer; 2006:1–19.

77. Young M. *Optics and Lasers: Including Fibers and Optical Waveguides*. Vol 5. Springer Science & Business Media; 2000.

78. Confocal Microscopy - Resolution and Contrast in Confocal Microscopy. https://www.olympus-lifescience.com/en/microscope-resource/primer/techniques/confocal/resolutionintro/. Accessed March 13, 2018.

79. Anderson PW. Absence of diffusion in certain random lattices. *Physical review*. 1958;109(5):1492.

80. Pradhan P, Damania D, Joshi HM, et al. Quantification of nanoscale density fluctuations by electron microscopy: probing cellular alterations in early carcinogenesis. *Physical biology*. 2011;8(2):026012.

81. Pradhan P, Sridhar S. Correlations due to localization in quantum eigenfunctions of disordered microwave cavities. *Physical review letters*. 2000;85(11):2360.

82. Pawley JB. Points, pixels, and gray levels: digitizing image data. In: *Handbook of Biological Confocal Microscopy*. Springer; 2006:59–79.

83. Pradhan P, Damania D, Joshi HM, et al. Quantification of nanoscale density fluctuations using electron microscopy: Light-localization properties of biological cells. *Applied physics letters*. 2010;97(24):243704.

84. Darzynkiewicz Z. Critical aspects in analysis of cellular DNA content. *Current protocols in cytometry*. 2010:7–2.

85. Muller M. *Introduction to Confocal Fluorescence Microscopy*. Vol 69. SPIE press; 2006.

86. Beuthan J, Minet O, Helfmann J, Herrig M, Müller G. The spatial variation of the refractive index in biological cells. *Physics in Medicine & Biology*. 1996;41(3):369.

87. Barer R, Ross KFA, Tkaczyk S. Refractometry of living cells. *Nature*. 1953;171(4356):720.

88. Lidorikis E, Sigalas MM, Economou EN, Soukoulis CM. Tight-binding parametrization for photonic band gap materials. *Physical review letters*. 1998;81(7):1405.

89. Fyodorov YV, Mirlin AD. Mesoscopic fluctuations of eigenfunctions and level-velocity distribution in disordered metals. *Physical Review B*. 1995;51(19):13403.

90. Pradhan P, Damania D, Joshi HM, et al. Quantification of nanoscale density fluctuations using electron microscopy: Light-localization properties of biological cells. *Applied physics letters*. 2010;97(24):243704.

91. Sheppard CJ. Fractal model of light scattering in biological tissue and cells. *Optics letters*. 2007;32(2):142–144.

92. Kim JS, Pradhan P, Backman V, Szleifer I. The influence of chromosome density variations on the increase in nuclear disorder strength in carcinogenesis. *Physical biology*. 2011;8(1):015004.

93. Pradhan P, Sridhar S. From chaos to disorder: Statistics of the eigenfunctions of microwave cavities. *Pramana*. 2002;58(2):333–341.

94. John S. Localization of light. *Phys Today*. 1991;44(5):32–40.

95. Kramer B, MacKinnon A. Localization: theory and experiment. *Reports on Progress in Physics*. 1993;56(12):1469.

96. Domınguez-Adame F, Malyshev VA. A simple approach to Anderson localization in one-dimensional disordered lattices. *American Journal of Physics*. 2004;72(2):226–230.

97. Lüschen HP, Scherg S, Kohlert T, et al. Exploring the Single-Particle Mobility Edge in a One-Dimensional Quasiperiodic Optical Lattice. *arXiv preprint arXiv:170903478*. 2017.

98. Abrahams E, Anderson PW, Licciardello DC, Ramakrishnan TV. Scaling theory of localization: Absence of quantum diffusion in two dimensions. *Physical Review Letters*. 1979;42(10):673.

99. Sahay P, Almabadi HM, Ghimire HM, Skalli O, Pradhan P. Light localization properties of weakly disordered optical media using confocal microscopy: application to cancer detection. *Optics express*. 2017;25(13):15428–15440.

100. Pradhan P, Sridhar S. From chaos to disorder: Statistics of the eigenfunctions of microwave cavities. *Pramana*. 2002;58(2):333–341.

101. Soule HD, Maloney TM, Wolman SR, et al. Isolation and characterization of a spontaneously immortalized human breast epithelial cell line, MCF-10. *Cancer research*. 1990;50(18):6075–6086.

102. Lane MA, Romagnoli L, Cruise B, Cohn GM. Spontaneous conversion to estrogen receptor expression by the human breast epithelial cell line, MCF-10A. *Oncology reports*. 1999;6(3):507–518.

103. Richter K, Nessling M, Lichter P. Experimental evidence for the influence of molecular crowding on nuclear architecture. *Journal of Cell Science*. 2007;120(9):1673–1680.

104. Kim JS, Pradhan P, Backman V, Szleifer I. The influence of chromosome density variations on the increase in nuclear disorder strength in carcinogenesis. *Physical biology*. 2011;8(1):015004.

105. Kim JS, Pradhan P, Backman V, Szleifer I. The influence of chromosome density variations on the increase in nuclear disorder strength in carcinogenesis. *Physical biology*. 2011;8(1):015004.

106. Bastide C, Bagnis C, Mannoni P, Hassoun J, Bladou F. A Nod Scid mouse model to study human prostate cancer. *Prostate cancer and prostatic diseases*. 2002;5(4):311.

107. Thalmann GN, Anezinis PE, Chang S-M, et al. Androgen-independent cancer progression and bone metastasis in the LNCaP model of human prostate cancer. *Cancer research*. 1994;54(10):2577–2581.

108. Kawada M, Inoue H, Usami I, et al. Establishment of a highly tumorigenic LNCaP cell line having inflammatory cytokine resistance. *Cancer letters*. 2006;242(1):46–52.

109. Cunningham D, You Z. In vitro and in vivo model systems used in prostate cancer research. *Journal of biological methods*. 2015;2(1).

110. Stone KR, Mickey DD, Wunderli H, Mickey GH, Paulson DF. Isolation of a human prostate carcinoma cell line (DU 145). *International journal of cancer*. 1978;21(3):274–281.

111. Liu AY, Brubaker KD, Goo YA, et al. Lineage relationship between LNCaP and LNCaP-derived prostate cancer cell lines. *The Prostate*. 2004;60(2):98–108.